7-2021

High Heat Flux Dissipation Using Innovative Dual Tapered Manifold in Pool Boiling, and Thermosiphon Loop for CPU Cooling in Data Centers

Aranya Chauhan
axc7796@rit.edu

Recommended Citation

Chauhan, Aranya, "High Heat Flux Dissipation Using Innovative Dual Tapered Manifold in Pool Boiling, and Thermosiphon Loop for CPU Cooling in Data Centers" (2021). Thesis. Rochester Institute of Technology. Accessed from

R.I.T

High Heat Flux Dissipation Using Innovative Dual Tapered Manifold in Pool Boiling, and Thermosiphon Loop for CPU Cooling in Data Centers

by

Aranya Chauhan

A dissertation submitted in partial fulfilment of the requirements for the degree of Doctor of Philosophy in Engineering

Engineering PhD Program

Kate Gleason College of Engineering

Rochester Institute of Technology
Rochester, New York
July, 2021

High Heat Flux Dissipation Using Innovative Dual Tapered Manifold in Pool Boiling, and Thermosiphon Loop for CPU Cooling in Data Center

by

Aranya Chauhan

Committee Approval:

We, the undersigned committee members, certify that we have advised and/or supervised the candidate on the work described in this dissertation. We further certify that we have reviewed the dissertation manuscript and approve it in partial fulfillment of the requirements of the degree of Doctor of Philosophy in Engineering.

Dr. Satish G. Kandlikar (Advisor)
Date
James E.Gleason Professor, Mechanical Engineering

Dr. Kathleen Lamkin-Kennard
Date
Associate Professor, Mechanical Engineering

Dr. Michael Schertzer
Date
Associate Professor, Mechanical Engineering

Dr. Santosh Kurinec
Date
Professor, Electrical and Microelectronic Engineering

Certified by:

Dr. Edward Hensel
Date
Director, PhD in Engineering Program

Abstract

Kate Gleason College of Engineering
Rochester Institute of Technology

Degree: Doctor of Philosophy **Program:** Engineering PhD

Author: Aranya Chauhan **Advisor:** Satish G. Kandlikar

Dissertation Title: High Heat Flux Dissipation Using Innovative Dual Tapered Manifold in Pool Boiling, and Thermosiphon Loop for CPU Cooling in Data Center

The current trend of electronics miniaturization presents thermal challenges which limit the performance of processors. The high heat fluxes in CPUs are affecting the reliability and processing ability of the servers. Due to these thermal limitations, large amount of energy is required to cool the servers in data centers. The advanced two-phase boiling heat transfer systems are significantly more efficient than currently used single phase coolers. In the current work, a novel approach is adopted by using a dual tapered microgap over the heated boiling surface for enhanced heat transfer. The theoretical work has identified the role of two-phase pressure recovery effect induced by the expanding bubbles in the tapered microgap configuration that leads to a self-sustained flow over the heater surface. This effectively transforms the pool boiling into a pumpless flow boiling system. Additionally, the tapered microgap introduces a bubble squeezing effect that pushes the liquid along the expanding taper direction. High fluid velocities are generated through this mechanism thus creating the pumpless flow boiling process in a conventional pool boiling system. Using water as the working fluid, a critical heat flux (CHF) of 288 W/cm^2 was achieved at a wall superheat of 24.1°C. The baseline configuration without any tapered manifold resulted in a CHF of 124 W/cm^2 at a wall superheat of 23.8°C. This represents the largest enhancement ever reported for water on a plain surface without incorporating any surface modifications during pool boiling. For dielectric liquid as the working fluid, the dual tapered micogap obtained ~2X enhancement in the heat transfer coefficient (HTC) compared to the configuration with the baseline configuration. This dual tapered microgap design is also implemented in a thermosiphon loop for CPU cooling where no pumping power is required for fluid circulation in a closed loop. The loop contains an evaporator with a dual tapered microgap and was able to dissipate heat from an actual CPU (i7-930 processor, TDP 130

W) more efficiently as compared to air, or water-based coolers during thermal stress tests. This dual taper evaporator configuration will be able to mitigate the hotspots generated on the CPU surface and improve the efficiency and mechanical integrity of the processor. Such boiling heat transfer systems can significantly reduce the cooling water temperature requirement thereby reducing the operational cost of data centers.

Acknowledgement

I would like to sincerely express my gratitude to my advisor Dr. Satish G Kandlikar for his continuous guidance and support throughout this work. I would like to thank him for giving me this opportunity to develop the understanding of the subject and express my ideas at various platforms. His enthusiasm and sincerity inspired me at every step and helped me in achieving my goals.

I would like to thank my committee members – Dr. Kathleen Lamkin-Kennard, Dr. Michael Schertzer, and Dr. Santosh Kurinec for providing helpful suggestions during the course of study. I am grateful to all TAMFL lab members – Dr. Arvind Jaikumar, Dr. Alyssa Owens, Dr. Pruthvik Raghupathi, Dr. Travis Emery, Dr. Isaac Perez-Raya, Dr. Jose-Luis Gonzalez-Hernandez, Aniket Rishi, Akshat Negi, and Maharshi Shukla for their continuous support and assistance without which this work would not have been possible. I would sincerely like to thank Craig Arnold for the fabrication of parts for test assembly, and Emilio Del Plato and William Finch for their help in setting up the server for testing.

I would like to thank my parents for their blessings and always believing in me. I am grateful to them for providing the constant support at every stage of my life, there are no words to express the sacrifices they have made.

Dedication

To

Sadhana Singh and Pradeep Singh

Table of Contents

List of Figures

List of Tables

Nomenclature

q''	heat flux, W/cm^2
dT/dx	temperature gradient, °C/m
k_{Cu}	thermal conductivity of copper, W/(m°C)
T_s	surface temperature, °C
ΔT_{sat}	wall superheat, °C
T_1	top thermocouple temperature, °C
T_2	middle thermocouple temperature, °C
T_3	bottom thermocouple temperature, °C
T_4	chip thermocouple temperature, °C
T_{sat}	saturation temperature of liquid, °C
Δx	distance between successive thermocouples, m
x_1	distance between surface and T_4 thermocouple, m
T_{CPU}	average temperature of the four cores of CPU, °C
$\Theta_{J\text{-}CW}$	temperature difference between CPU and chiller water, °C
B_y	bias error
P_y	precision error
U_y	total uncertainty
dP/dz	pressure drop per unit length, Pa/m
dz	length along flow direction, m
L_{tp}	two phase flow length, m
f_{tp}	two phase friction factor (-)
G	mass flux, kg/(m^{2}s)
$\dot{m}$	mass flow rate, kg/s
D_h	hydraulic diameter, m
x	exit quality (-)
h_{fg}	latent heat of vaporization, J/kg

A_c	cross section area, m^2
Co	convection number (-)
Bo	boiling number (-)
$C_1 - C_4$	constants (-)
h_f	liquid phase heat transfer coefficient, W/(m^2°C)
F_f	liquid dependent parameter (-)
Re_f	liquid Reynolds number (-)
Pr_f	liquid Prandtl number (-)
k_f	liquid thermal conductivity, W/(m°C)
F_σ	force due to surface tension, N/m
F_p	force due to pressure difference, N/m
F_{em}	evaporation momentum force, N/m
F_{net}	net force at bubble interface, N/m

Greek Symbols

v_f	specific volume of the liquid, m^3/kg
v_g	specific volume of the vapor, m^3/kg
v_{fg}	difference in the specific volumes of the liquid and vapor phases, m^3/kg
Θ	angle of inclination from the horizontal plane, °
μ_{tp}	two phase viscosity, Pas
μ_g	dynamic viscosity of vapor, Pas
μ_f	dynamic viscosity of liquid, Pas
ρ_f	liquid density, kg/m^3
ρ_g	vapor density, kg/m^3
ΔP_{geo}	pressure drop due to geometry - entrance and exit losses, Pa

Subscript

Cu	copper
s	surface
sat	saturation
tp	two phase
h	hydraulic
c	cross section
f	liquid
g	vapor
geo	geometry

Abbreviation

HTC	heat transfer coefficient, W/(m^2°C)
CHF	critical heat flux, W/m^2 or W/cm^2

Chapter 1

1.0 Introduction

1.1 Electronics Thermal Management

The trend of miniaturization in electronic chips [1] as shown in Fig.1 represents the reduction in gate length and increase in number of transistors in the processor since 1970s, and this leads to several thermal design challenges in the device. The processors are getting smaller and faster every year, and the performance demand is increasing. In 1965, Intel co-founder Gordon Moore predicted that the number of transistors per square inch on integrated chip will double every year, and this has been happening since then [2]. But such trends are difficult to follow in the future because the performance and size of the electronic devices are significantly constrained by their thermal threshold. Developing effective cooling techniques to dissipate a large heat fluxes from small devices is proving to be a great challenge for the design engineers. Presently used cooling techniques are not efficient enough and this greatly affects the data processing ability of the processors. This results in highly inefficient large scale cooling operations such as server cooling in data centers.

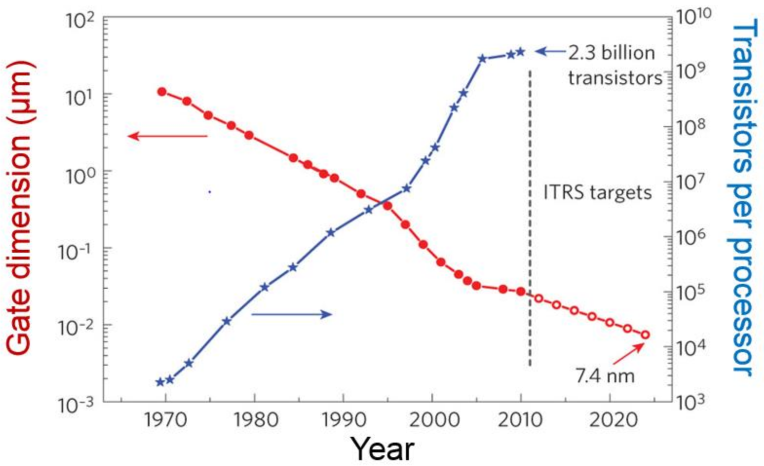

Figure 1: The trend of miniaturization in electronics [1]

A data center is a building used to house computer systems for the storage, distribution, and processing of large quantity of data. Data centers manage the internet connectivity across the globe acting as the backbone of information transfer around the globe. It contains large number central processing units (CPUs) installed in the servers generating high heat fluxes under stressful working conditions. A data center may have multiple server rooms, each room contains several server racks arranged in an array.

Due to enormous energy consumption during server cooling, a significant cost is spent on data center management annually. Based on the findings of Cool IT Systems, in an air-based cooled data center, 60% of the total power consumption is used for networking, server, storage etc., and the remaining 40% power is used for cooling operations as shown in Fig.2. Based on the report by Natural Resources Defense Council in partnership with Anthesis, in 2013 nearly 3 million computer rooms in data centers used electricity equivalent to the annual output of 34 large coal-fired power plants. The US based data centers have the potential to reduce the electricity consumption by 40 percent[3], this estimates to an energy saving of 39 billion kilowatt-hours equivalent to $3.8 billion. Currently used CPU cooling techniques based on air, and water as the cooling medium are discussed in the following section.

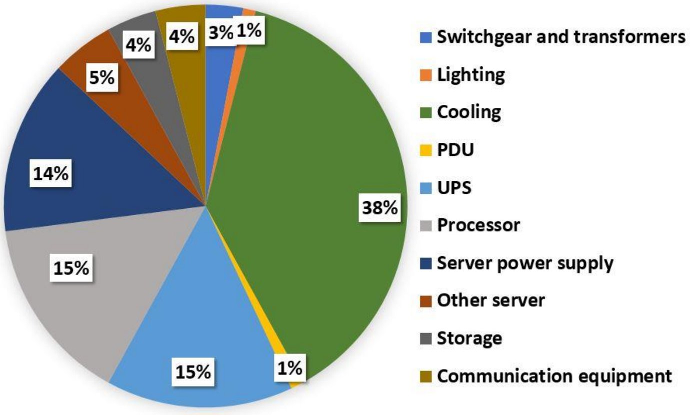

Figure 2: Distribution of total power consumption in a data center according to Cool IT Systems.

1.2 Data Center Cooling Techniques

The two major types of currently used data center cooling processes are air, and water-based techniques. These two strategies are discussed in this section.

1.1.1 Air Cooling

In an air-based cooling system, a computer room air conditioner (CRAC) or computer room air handler (CRAH) unit is installed in the server room. The cold air is supplied from the CRAC unit to the inlet of racks. The cold air flow is driven through each server by a fan arrangement installed in the server, and hot air from the outlet of the racks is supplied back to the CRAC unit. The CRAC unit is connected to an external water chiller outside the data center. The water chiller extracts the heat from CRAC and dumps it in the open atmosphere. The two types configurations based on air flow from the CRAC to the racks' inlet are, (a) non raised floor design, and (b) raised floor layout [4]. In a non raised floor design, the cold air is supplied into the server room through diffusers. In a raised floor design as shown in Fig.3, the cold air is supplied through the raised floor which is constructed under the server room. The cold air is eventually supplied in the room via perforated floor design using tiles.

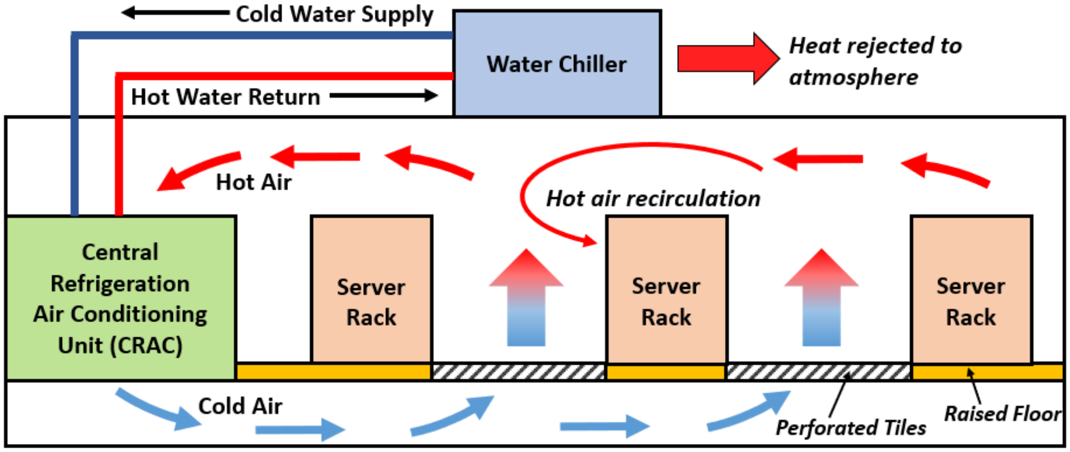

Figure 3: The air cooling mechanism in a raised floor layout for data center cooling.

The major thermal challenge in the air-based cooling system is hot air recirculation. The hot air from the outlet of the racks is recirculated in the room and is supplied into the server inlet resulting in high server temperatures. The servers towards the top of the rack receive hot air due to recirculation compared to the servers placed near the floor. The processing load on the rack is limited by the air temperature at the hot end, and this results in efficient rack processing.

The air flow segregation approach can be adopted to minimize the hot air recirculation. This can be accomplished by developing hot-cold aisle containments [5]. In such configuration, the designated aisles are constructed, and the cold air from the perforated tiles is supplied in the cold aisle. The cold air flows through the front end of the servers along the rack height and the hot air from the rear end of the servers is expelled in the hot aisle. The segregation aisles can be constructed using Plexiglas, and this design offers a low-cost approach. The plexiglass walls are nonstructural in nature and therefore can be modified easily based on the design requirements.

The air cooling has reached its maximum heat dissipation limit. Air offers low heat transfer coefficient, and this results in high convection based thermal resistances. The specific heat capacity of air is also low, therefore, to mitigate these effects high temperature differences between cooling air and the servers are needed for required heat dissipation. This results in the demand of unnecessary low air temperature supply. In a conventional server, the required temperature of the air at the inlet of the server is 27 °C but the air supplied in the server room is at 15°C or lesser. Hence effective cooling solutions are required for efficient CPU cooling in servers.

1.1.2 Water Cooling

The water-based cooling configuration is generally used to dissipate heat from high density servers. In present air-based cooling systems, the heat from CRAC units is dissipated by a water-cooled external chiller. Therefore, cooling processing equipment using water as the coolant is an extension of the currently used water-cooling loops closer to the server. The two levels of water-based cooling systems are, (a) rack level cooling, and (b) server level cooling.

The two configurations of rack level cooling are, (i) liquid-cooled door, and (ii) closed-liquid rack. In liquid-cooled door, the liquid is supplied to the door of the rack, and the door is constructed as an air-liquid heat exchanger. The hot air expelled from the rack passes through the door heat exchanger and cold air from the heat exchanger is resupplied to the rack inlet. Two other types of rack level cooling methods similar to liquid-cooled door configuration are overhead liquid coolers, and in-row liquid coolers. In closed-liquid rack system, the rack is completely sealed, and a liquid-cooled heat exchanger is installed below the rack. The room air enters the sealed rack from the bottom into the heat exchanger, and cold air from the heat exchanger flows along the rack height towards the multiple server inlets. These configurations eliminate the need of developing hot-cold aisles.

In server level cooling, the working cooling liquid is supplied to the CPU in the server, and heat dissipation takes place through a cold plate attached on the top on CPU. The heat dissipation efficiency of server level cooling is much higher than the rack level cooling system. Reduced thermal resistance is obtained in server level cooling due to smaller heat transfer path between the cooling liquid and CPU [6,7]. The server level cooling does not eliminate the need of air as cooling medium since several other components in the server require cooling. The transition from rack level to server level cooling adds more design complexity and cost, and it is suggested to adopt server level cooling for high power density CPU applications.

Immersion cooling: Another configuration of liquid cooling is immersion cooling. In this configuration, the server is completely immersed in a dielectric cooling liquid. The heat from the electronic components is dissipated into the dielectric liquid by natural convection. This server-dielectric system is enclosed, and an external water loop is used to transfer heat from the dielectric liquid outside the enclosure. A schematic of immersion cooling setup is shown in Fig. 4.

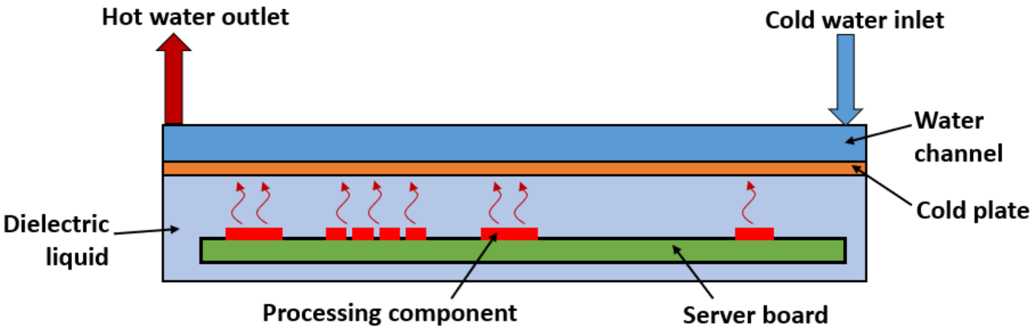

Figure 4: The schematic of water-cooling loop in a dielectric direct immersion cooling setup.

1.3 Two Phase Heat Transfer

The efficient high heat flux dissipation and hot-spot mitigation demands from the CPUs in a data center are beyond the capability of previously discussed single-phase cooling mechanisms. The two-phase heat transfer (boiling heat transfer) is the futuristic approach for reliable thermal management of the processing equipment. The two main categories of boiling heat transfer systems are, (a) pool boiling, and (b) flow boiling.

1.3.1 Pool Boiling

In a pool boiling system, a stagnant pool of liquid is converted into vapor phase at the saturation temperature of liquid due continuous heat supply from a heated surface where the heating surface's temperature is greater than the saturation temperature of the liquid. The degree of wall superheat (ΔT_{sat}) is defined as the temperature difference between the heating surface and the saturation temperature of liquid. Heat flux is defined as the amount of heat dissipated from the heated surface per unit area and it is measured in W/cm^2 or W/m^2. For electronics cooling application, heat flux is generally represented in W/cm^2 since the electronic equipment have small dimensions.

The various regimes in boiling heat transfer are studied using a boiling curve as shown in Fig. 5. In boiling curve, the controlling parameter is heat flux which is shown on the Y-axis. And the dependent parameter is wall superheat which is represented on the X-axis. This approach was adopted when Nukiyama introduced the first pool boiling curve [8], since then this representation of heat flux and wall superheat has been followed by the researchers. The different regimes in the boiling curve are, (a) natural convection, (b) partial nucleate boiling, (c) fully developed nucleate boiling, (d) transition boiling, and (e) film boiling. The exact nature of the boiling curve is dependent on the working liquid and the morphology of the heating surface.

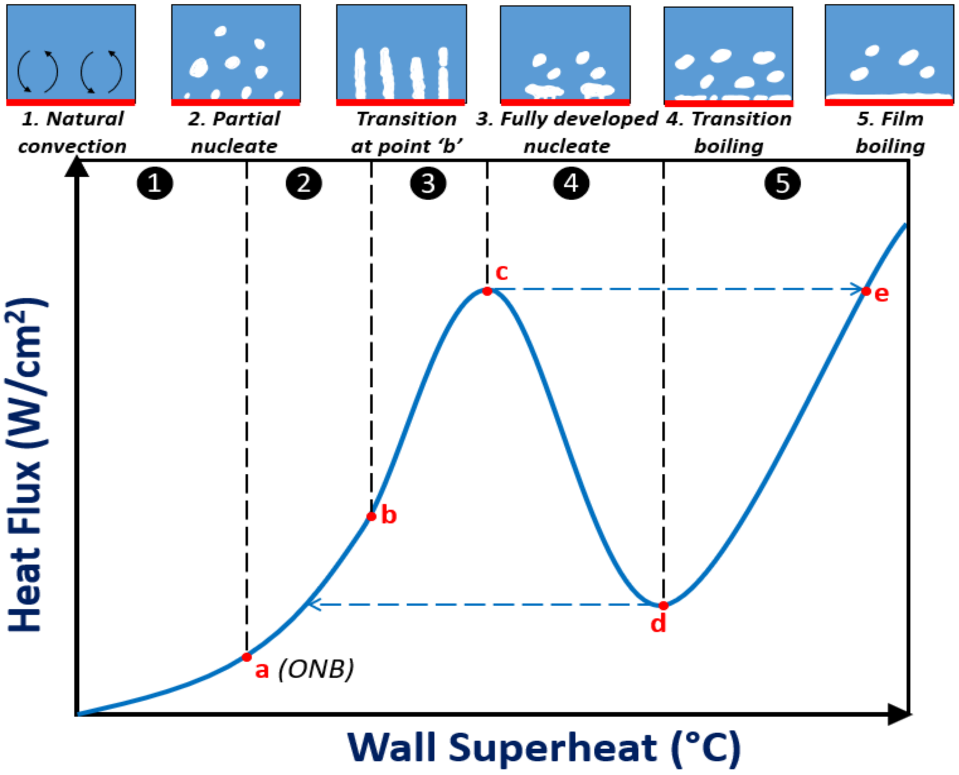

Figure 5: Pool boiling curve showing different boiling regimes.

Natural convection (Region 1): The natural convection region is defined from the origin of the curve to point ‘a’. At low heat fluxes, the wall superheat is small and liquid near the heated surface is at higher temperature compared to the bulk liquid. This temperature gradient in the liquid volume creates a density difference along the height. The hot liquid near the heated surface is less dense hence rises upwards, and cold denser liquid from the bulk replaces the hot liquid near the heated surface. This develops a natural convection flow, and this mode of heat transfer sustains till point ‘a’.

Partial nucleate boiling (Region 2): At point ‘a’ the bubble starts nucleating from the heated surface and this point of first bubble occurrence is called onset of nucleate boiling (ONB). The partially developed nucleate boiling region is defined from point ‘a’ to point ‘b’. In this region, the bubbles nucleate from various active nucleation sites, and the bubble nucleation frequency increases with continuous increase in the heat flux.

Fully developed nucleate boiling (Region 3): The transition from partial to fully developed nucleate boiling is shown by point ‘b’. At point ‘b’, the bubbles begin coalescing in the vertical direction to form continuous vapor jets. The fully developed nucleate boiling region is defined from point ‘b’ to point ‘c’. In this region, the bubbles begin coalescing horizontally along the heated surface to form mushroom like vapor structures with several stems attached on the heated surface. As the heat flux increases, at point ‘c’ critical heat flux (CHF) condition is achieved. At CHF a sudden jump in the surface temperature is observed as shown by the dashed line from point ‘c’ to point ‘e’.

Film boiling (Region 5): At CHF, the bubble nucleation frequency is highest, and bubbles coalesce on the heated surface to form a stable insulating vapor film. This increases the surface temperature, and the dominant mode of heat transfer is radiation. By reducing the heat flux, the boiling curve is traced from point ‘e’ to ‘d’. At point ‘d’, minimum heat flux is achieved, and this point is called Leidenfrost point. Further reducing the heat flux results in sudden drop in the wall superheat value and the nucleate boiling is attained.

Transition boiling (Region 4): The transition boiling region is from point ‘d’ to point ‘c’. This boiling region can be obtained by controlling the wall superheat. The previously discussed regions were achieved by controlling the heat flux. In transition boiling, the bubbles occupy significant area on the heated surface.

A significant heat transfer enhancement is obtained in the nucleate boiling region; hence this region (point ‘a’ to point ‘c’) defines the desired operating range for a two-phase system. The steep nature of the boiling curve in the partial nucleate boiling and fully developed nucleate boiling regions suggest high heat fluxes can be dissipated with small increase in the wall superheat. Therefore, high heat transfer coefficient (HTC) can be obtained in this region. HTC is the ratio of heat flux and the wall superheat, and it defines the heat dissipation efficiency of the system.

1.3.2 Flow Boiling

In flow boiling, the desired liquid flow rate on the heated surface is achieved by using an external pump. The bubbles are forced to move along the boiling domain due to high liquid inertia, unlike pool boiling where bubble motion was significantly driven by the buoyancy. The different boiling regimes in a flow boiling channel are characterized based on the relative liquid-vapor volumes in the channel. These boiling regimes in a flow boiling system are shown in Fig.6.

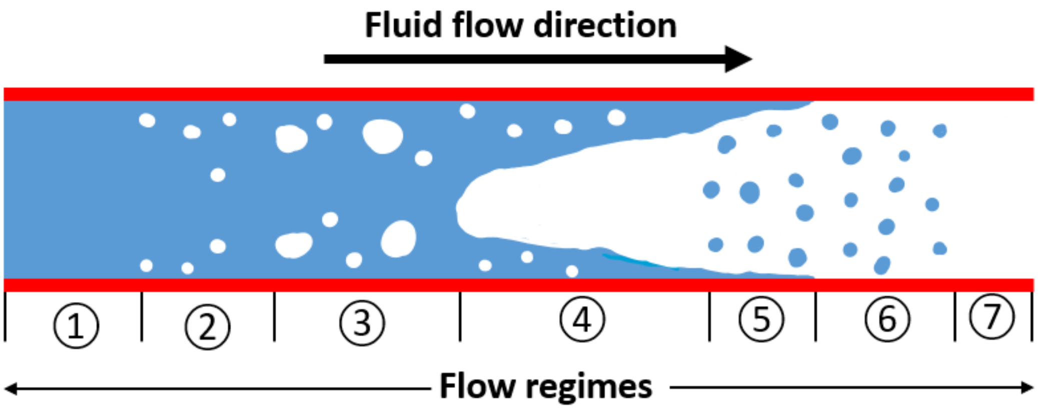

Figure 6 : Schematic showing different regimes during flow boiling in a closed channel.

The various regimes as shown in Fig.6 are described below.

Forced Convection with liquid flow (Region 1): The liquid is forced into the channel by an external pump and forced convection occurs along the heated walls as liquid travels through region 1.

Bubbly Flow (Region 2): The liquid is continuously heated along the surface and this initiates bubble nucleation at the saturation condition. The bubbles move along the heated surface due to forced fluid flow and begin to move towards the core due to buoyancy.

Slug Flow (Region 3): As the liquid is further heated along the surface, the fluid core also heats up and the temperature of the liquid in the core increases resulting in bubble expansion due to evaporation and coalescence to form large bubbles.

Annular Flow (Region 4): Due to continuous bubble expansion and coalescence in the core, a large vapor space is created confining liquid in the smaller spaces along the heated surface.

Transition Flow (Region 5): The liquid region is restricted to minimal spaces close to the heater and eventually disappears due to continuous evaporation and expansion of vapor space in the core. Small drops of liquid are also observed in the core of the channel.

Mist Flow (Region 6): In this region, the liquid flows in the vapor dominated space in the form of mist.

Forced Convection with Vapor Flow (Region 7): Towards the end of the channel, the mist completely evaporates, and the channel space is entirely occupied by the vapor phase.

1.3.3 Thermosiphon Loop

Thermosiphon loop is a gravity driven self-sustaining closed system, containing a boiling section in the evaporator and a heat exchanger in the condenser. A schematic of thermosiphon loop in shown in Fig.7. The working liquid is charged in the condenser, and the liquid is supplied into the heating section of the evaporator due to the gravitational head between the evaporator and the condenser. The working liquid flows on the heated surface and bubbles nucleate on the surface at saturation temperature. Like pool boiling and flow boiling systems, small temperature difference can be maintained between the working liquid and heating surface due to phase change process. Based on the heat flux dissipated, bubbles coalesce to form large vapor and leave the evaporator rising vertically towards the condenser. The heat exchanger in the condenser extracts heat from the vapor and converts vapor back into liquid phase. The condenser acts as a reservoir and supplies liquid back into the evaporator.

Thermosiphon loop is a flow boiling system where fluid flow is driven due to gravity. Since no external pump is required for fluid pumping, this significantly reduces the power requirement and the operational cost especially in large scale applications such as CPU cooling in data centers. In another configuration of thermosiphon loop, the evaporator is flooded with the working liquid and pool boiling heat transfer occurs at the heating surface, such systems are not the focus of this study.

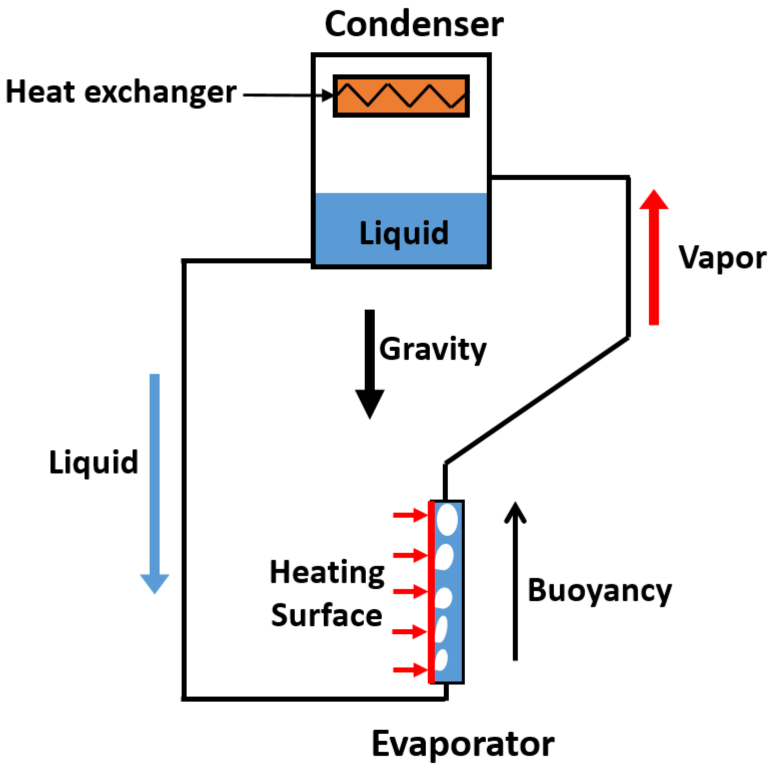

Figure 7: The schematic of thermosiphon loop with evaporator and condenser.

Chapter 2

2.0 Literature Review

The literature review on different boiling systems, (a) pool boiling, (b) flow boiling, and (c) thermosiphon loop are discussed in this chapter. In pool boiling, the different surface enhancement techniques and separate liquid-vapor pathways mechanism are discussed. In flow boiling, the different channel designs and tapered gap geometry were reviewed for heat dissipation enhancement. And finally, the potential of thermosiphon loop was also reviewed for electronics cooling application.

2.1 Pool Boiling

2.1.1 Surface Enhancements

Surface enhancement techniques have been studied by researchers to dissipate large heat fluxes efficiently by delaying the CHF and improving the HTC. The region near the heated surface affects the enhancement mechanisms such as contact line augmentation. The enhancements based on contact line augmentation include wicked surfaces [9], roughness augmentation [10–12], and microlayer partioning [13]. Raghupathi et al.[14] presented the effect of microgrooves on the departure diameter and bubble dynamics. The bubble gets pinned in 100 µm deep groves hence CHF was reduced but enhanced CHF was obtained using the 200 µm wide and 10-20 µm deep groves. Zou and Maroo [13] significantly improved the CHF by increasing the bubble frequency using nano-micro ridges for the partition of microlayer into slabs. Rahman et al.[9] reported that increase in liquid wickability of the boiling surface leads to linear increment in the CHF. Chu et al. [10] increased the effective contact line dimension using micropillar roughness augmented surfaces, and this increased the CHF.

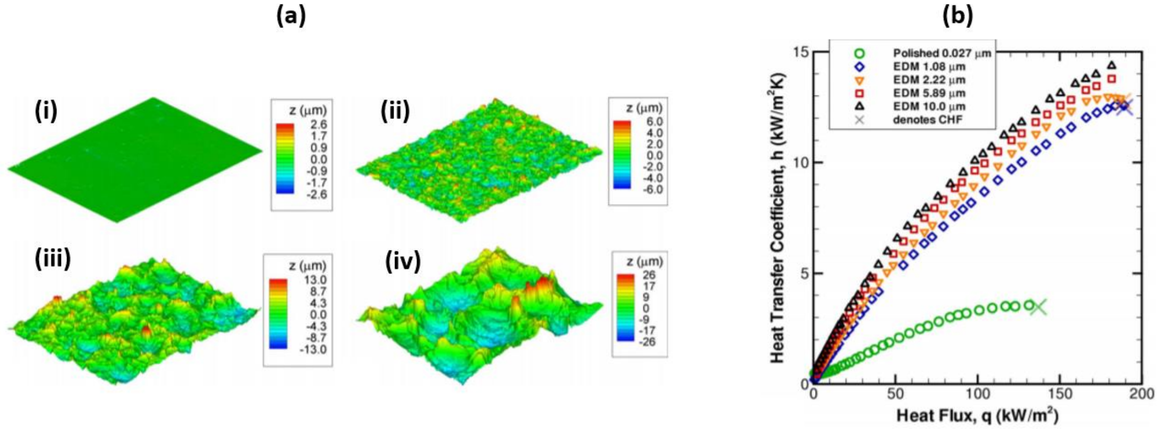

Figure 8: (a) Surface topography showing various roughness[10]; (i) 0.027 µm, (ii) 1.08 µm, (iii) 2.22 µm, and (iv) 5.89 µm, (b) Varying HTC with respect to heat flux for different roughness surfaces with FC-77[15]

Jones et al. [15] studied the effect of surface roughness on HTC for FC-77 and water as the working fluids. For FC-77 fluid, a continuous improvement in HTC was observed for surface roughness higher than 1.08 µm as shown in Fig.8. For water, the HTC increased significantly for roughness greater than 10 µm. Betz et al.[16] obtained improved CHF and HTC values using biphilic surfaces compared to the surface with uniform wettability. In biphilic configuration, the lateral bubble coalescence is prevented by the hydrophilic regions, and hydrophobic regions increase the number of active nucleation sites. Nam et al.[12] studied Si based hydrophilic and copper based superhydrophilic surfaces. It was observed that the performance enhancement can be achieved using superhydrophilic surfaces since the bubble departure diameter was reduced by a factor of 2.5 and the bubble growth duration was reduced 4 times. Figure 9 shows the various surface enhancements developed for the efficient heat flux dissipation. These enhancements are, wicking microstructures[17,18], bi-conductive configuration[19], tall porous structures[20,21], nano-micro ridges[14,22,23], and pores and tunnels[24].

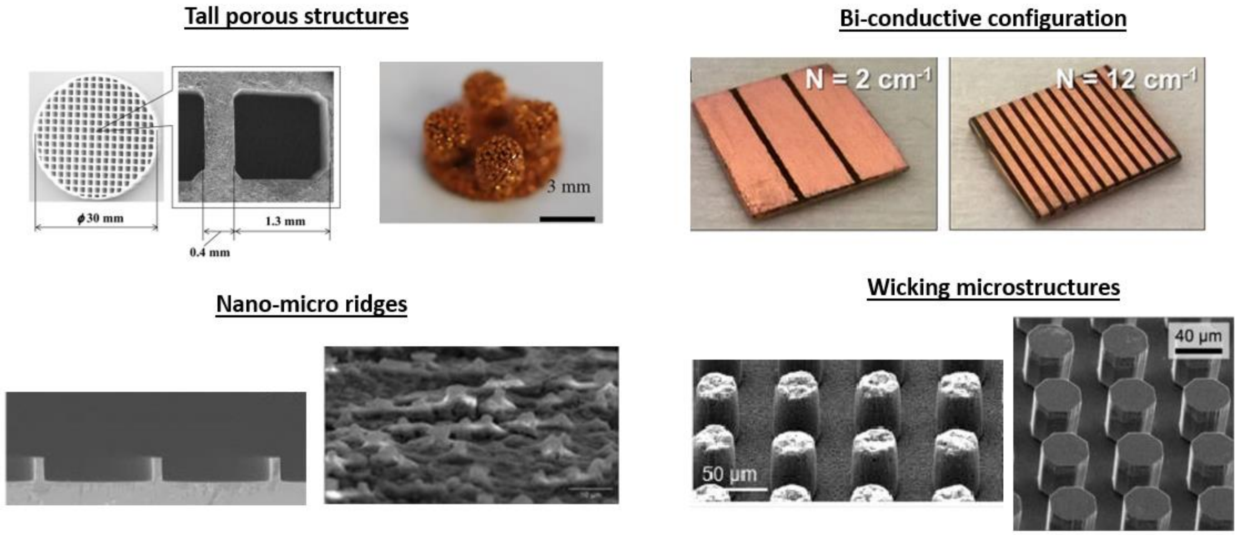

Figure 9: Various surface enhancements; tall porous structures [20,21], bi conductive configuration [19], nano micro ridges [14,22,23], and wicking microstructures [17,18].

2.2.2 Separate Liquid-Vapor Pathways

The efficient removal of vapor bubbles from the boiling surface, and continuous surface rewetting by developing effective liquid resupply are critical phenomena for CHF and HTC enhancement. Liter and Kaviany [25] used porous projections to develop vapor pathways at critical wavelengths and a separate liquid return supply mechanism. Kandlikar [26] developed contoured surfaces with fins as shown in Fig.10 and introduced the concept of evaporation momentum force driving the bubble motion away from the fin along the designed contour. This established separate liquid vapor pathways flow mechanism.

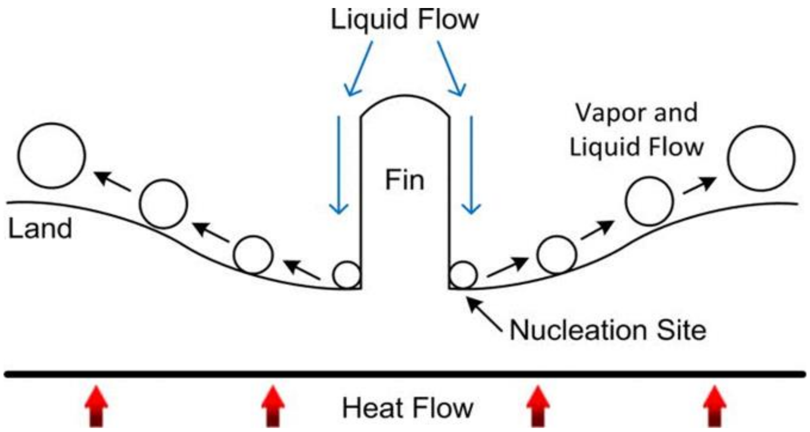

Figure 10: Schematic of the countered fin and the trajectory of a bubble nucleating the base of the fin [26].

Jaikumar and Kandlikar [27] achieved 2.4X and 6.5X enhancements in CHF and HTC values respectively using selectively sintered microchannels where fin tops were covered with a microporous coating. The liquid supply and vapor flow mechanism in selectively sintered microchannels is shown in Fig.11(a). Separate liquid vapor pathways were also established using nucleating regions with feeder channels (NRFC) configuration [28–30]. A novel copper chip was developed where nucleating regions (NRs) were designed to avoid the lateral bubble coalescence, and liquid jets were created in the adjacent NRs. The liquid is supplied to the NRs through feeder channels (FCs), and this establishes a stable liquid vapor pathways. The fluid flow mechanism in NRFCs is shown in Fig.11(b). A CHF of 420 W/cm^2 at wall superheat of 1.7^{o}C was obtained using NRFC chip, resulting in a significant HTC enhancement of 2.9 MW/m^{2o}C [31].

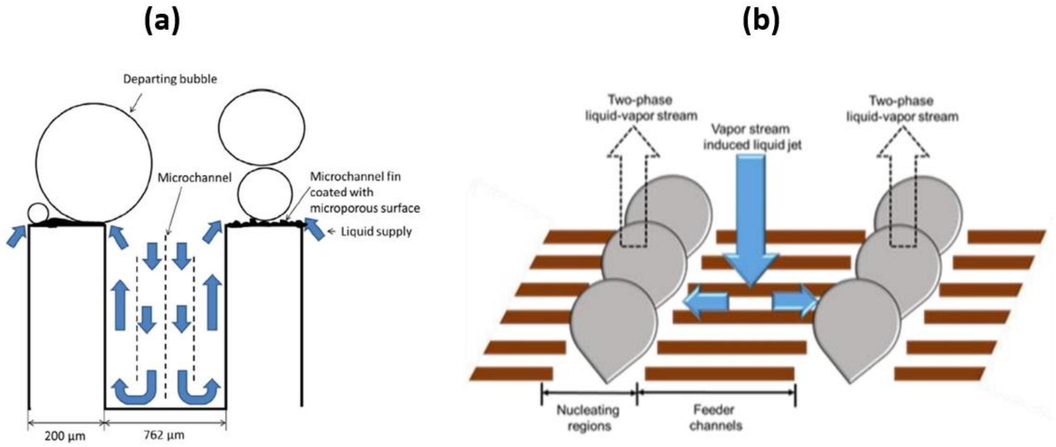

Figure 11: Schematics of separate liquid vapor pathways in (a) selectively sintered microchannels [27], and (b) NRFC configuration [28-31].

2.2 Flow Boiling

In flow boiling liquid flows over the heated surface where the flow rate is driven by an external pump unlike pool boiling where fluid flow was driven by buoyancy. Colgan et al.[32] studied single phase heat transfer using pumped flow and were able to dissipate 300 W/cm^2 but high chip temperature and pressure drops were obtained. Also, high pumping power was required to achieve desired fluid flow rate. Considering these limitations, flow boiling provides a promising solution for high heat dissipation with smaller wall superheat. The flow boiling heat transfer can be improved using microchannels due to higher surface to volume ratio [33]. The two types of microchannels configuration used in flow boiling based on the space available above the fins are, (a) open microchannels, and (b) closed microchannels, as shown in Fig.12. In open microchannels, additional space is available between the fin top and cover plate, this creates a continuous fluid domain between the channels. In closed microchannels, the cover plate is directly placed on the fin tops and disconnected fluid flow domains are developed for each microchannel. During boiling, the vapor expansion along the channels resists incoming flow of the liquid, and this effect is significant in closed microchannels leading to high flow instabilities. Whereas in open microchannels, the additional space above the fin tops allow smoother bubble expansion and this develops a stable fluid flow along the channels compared to closed microchannels configuration. Higher flow stability in the open microchannels improves the heat transfer efficiency and reduces the total pressure drop. The flow stability in microchannels chip can also be improved by reducing the channel length, and the number of channels [34,35].

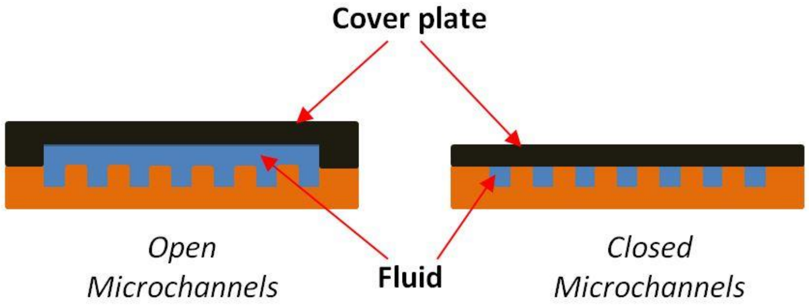

Figure 12: Different microchannels configuration - open and closed type.

Balasubramanian et al.[36] studied flow boiling using an expanding type of open microchannels as shown in Fig.13(a). A heat flux of 120 W/cm^2 was obtained with a surface temperature 122^{o}C with expanding microchannels. For straight microchannels at 120 W/cm^2, the surface temperature of 128^{o}C was achieved. Using expanding microchannels configuration, the pressure drop reduced from 0.037 bar to 0.015 bar as shown in Fig.13(b), therefore a higher flow stability was developed with lower pumping power. The expanding microchannels provide smoother bubble expansion along the channel length due to additional cross-sectional space.

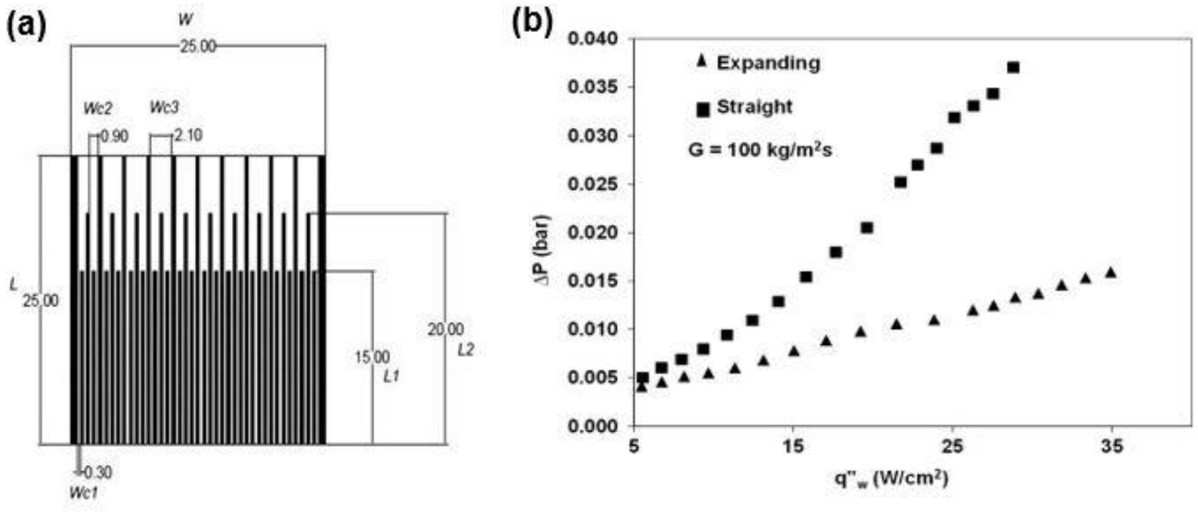

Figure 13: Flow boiling study conducted by Balasubramanian, (a) expanding microchannels configuration, (b) pressure drop comparison for expanding and straight microchannels [36].

Mukherjee and Kandlikar [37] proposed a stepped wall microchannels design in a numerical study to provide increasing cross section along the flow length and reduce the instability causing reversible flow as shown in Fig.14(a). To improve the ease of manufacturing, a smooth diverging channel design was also proposed as shown in Fig. 14(b) [38].

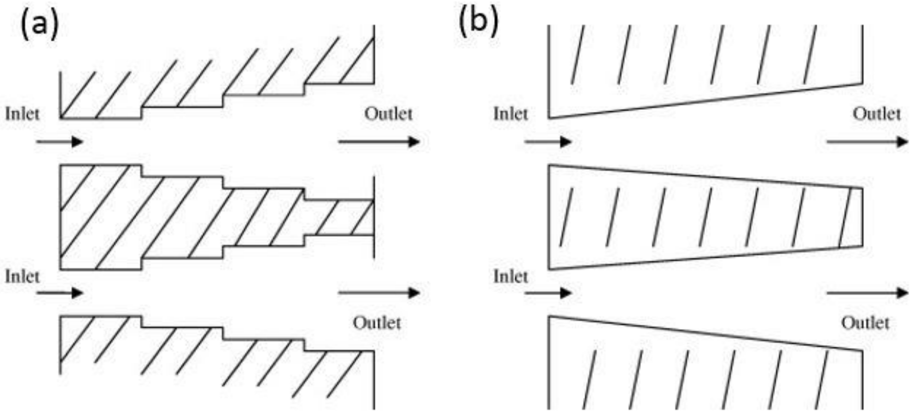

Figure 14: Expanding microchannels, (a) stepped wall microchannels [37], (b) smooth wall microchannels [38].

Lu and Pan [39] conducted an experimental study with diverging cross sections and 10 microchannels. The depth of each channel was 76 µm with a mean hydraulic diameter of 120 µm, and diverging angle of 0.5°. It was observed that diverging microchannels were able to achieve higher flow stability compared to uniform cross section channels.

Prajapati et al.[40] studied single phase heat transfer in diverging microchannels and evaluated the thermal performance of diverging, segmented, and uniform channels configuration as shown in Fig.15. The number of channels in each configuration was 12 with hydraulic diameter 522 µm. The highest HTC observed was ~ 14 kW/m^{2}K for segmented microchannels configuration at the mass flux of 130 kg/m^{2}s. The heat transfer parameters were recorded at various mass fluxes, 130 kg/m^{2}s, 194.7 kg/m^{2}s, 260 kg/m^{2}s and 324.5 kg/m^{2}s.

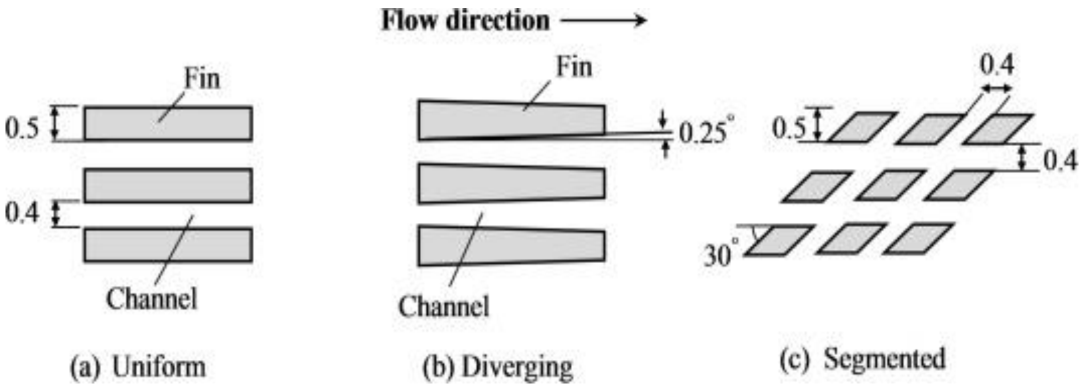

Figure 15: Different microchannels, (a) uniform, (b) diverging, (c) segmented studied by Prajapati et al. [40].

Kalani and Kandlikar [34,41] conducted flow boiling study with tapered manifold in an open microchannels configuration as shown in Fig.16 and obtained lower pressure drop and wall superheat compared to uniform manifold design. Three different tapered configurations 2%, 4%, and 6% were studied and HTC of 278 W/cm^2 was obtained with a pressure drop of 3.3 kPa for 6% taper. The performance of different tapered manifold configurations and uniform manifold are shown in Table 1.

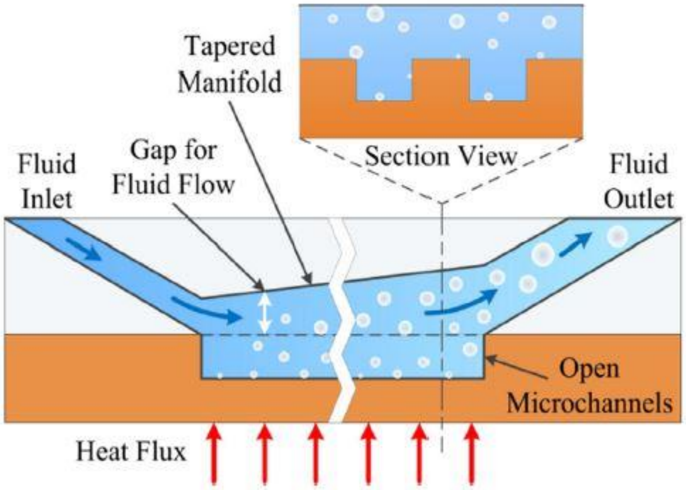

Figure 16: Tapered manifold on microchannels chip studied by Kalani and Kandlikar [34,41].

Table 1: Flow boiling performance of uniform and tapered manifolds [34,41].

Manifold	Heat Flux (W/cm^2)	Wall Superheat (^oC)	Pressure Drop (kPa)
Uniform	283.2	13	62.1
Taper A (2%)	265	14	7.5
Taper B (4%)	239.1	8.6	6
Taper C (6%)	281.2	10.1	3.3

The tapered manifold design was used on a microchannels chip with fin width, fin height, and channel width 200 µm, since the microchannels design achieves lower pressure drop along the flow length compared to plain chip design [42]. The heat transfer performance increases and pressure drop reduces using a tapered manifold compared to a uniform manifold design, but no heat flux or HTC enhancement is obtained by increasing the taper height on a plain copper chip. At low heat fluxes, the tapered manifold shows similar heat transfer performance compared to uniform manifold [34,41], but at high heat fluxes, the superior performance is obtained with tapered manifold [41,43].

Bubble expansion in tapered manifold: In a uniform manifold, the vapor bubble expands on the microchannels surface leading to dry out, this results in high pressure drop, low HTC, and early CHF [44,45]. In the tapered manifold, the increasing cross section allows bubble expansion in the vertical additional space along the flow direction, this delays the dry out to large extents. The vapor in tapered manifold flows above the microchannels due to buoyancy and allows effective continuous surface rewetting compared to uniform manifold. The bubble departure in the overhead space in the tapered manifold provides nucleating sites under the fully grown departed bubbles as shown in Fig.17, thus enhancing the heat transfer from microchannels surface to the working liquid [45].

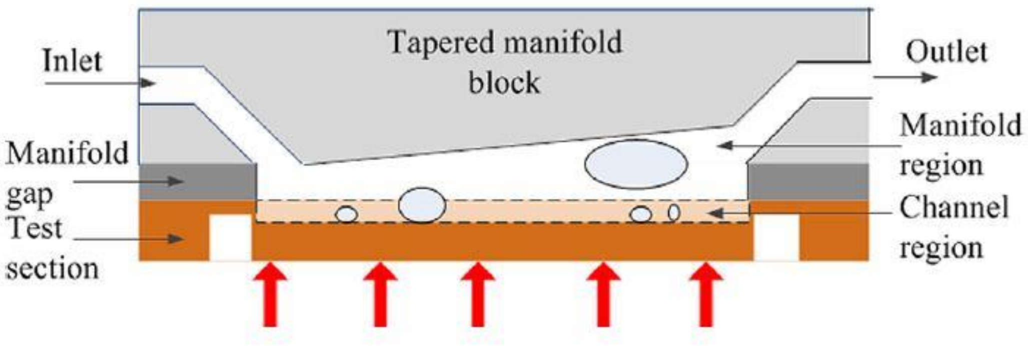

Figure 17: The bubble departure in tapered manifold and nucleation under a fully grown departed bubble [45].

Effect of flow rate in tapered manifold configuration: Kalani and Kandlikar [44,45] explained that the vapor bubbles can be removed effectively by increasing the Reynolds number (Re). At higher Re, the bubbles are carried away from the boiling domain due to high liquid inertia. For Re 1642, a CHF of 1.1 kW/cm^2 was obtained at a wall superheat of 43°C using a 6% taper manifold with microchannels. The tapered manifold design becomes essential at high Re since pressure drop also increases with increase in mass flow rate, and tapered design provides a pressure recovery effect. But at very high Re, the liquid inertia forces bubbles onto the heater surface leading to poor heat transfer performance as shown in Fig.18, and this phenomenon is called vapor blanketing.

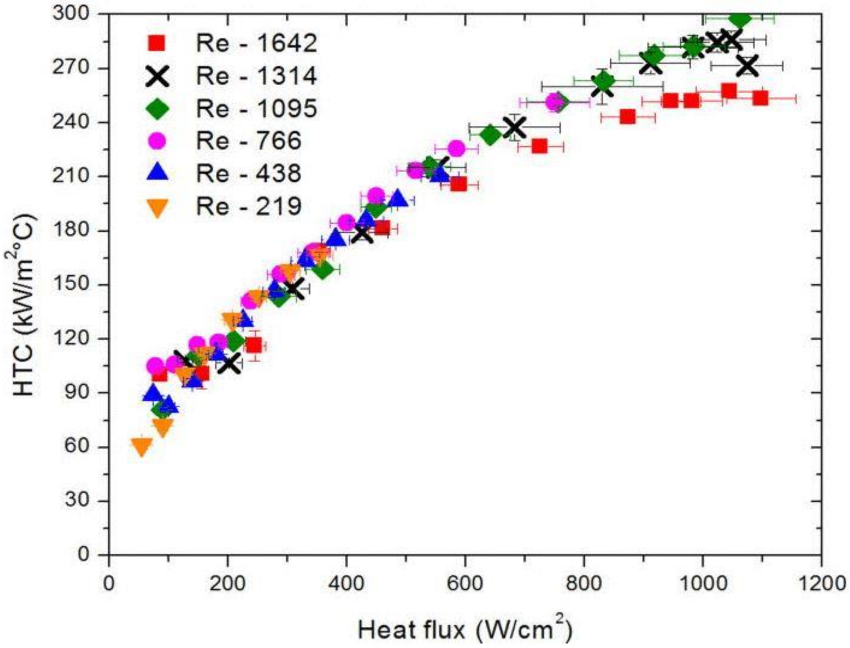

Figure 18: HTC variation with heat flux for different flow rates [44].

2.3 Thermosiphon Loop

The thermosiphon loop is a passive two-phase gravity driven system i.e., no external pump is required for fluid circulation. Thermosiphon loops are generally used to transfer heat over large distances compared to conventional heat pipes [46]. Franco and Filippeschi [47] experimentally studied a thermosiphon loop using plain hollow copper cylinder as the heating substrate in the evaporator and achieved heat flux of 370 kW/m^2 with water as the working fluid. Pal et al.[48] applied thermosiphon loop for processor cooling in a commercial desktop computer. The loop dissipated 50 W/cm^2 with water and the bottom temperature of the evaporator was maintained at 60°C. The system was also evaluated with refrigerant PF5060 as the working fluid, and the bottom temperature of the evaporator was maintained at 98°C. Lamaison et al.[49] numerically studied the thermal performance of thermosiphon loop for parallel cooling of two Intel Xeon E560 processors and dissipating 8 W/cm^2. The layout of the setup and performance results are shown in Fig.19. The performance results show the variation in mean chip temperatures during unbalanced heat load conditions for the two processors. In the experimental study on a test stand, the

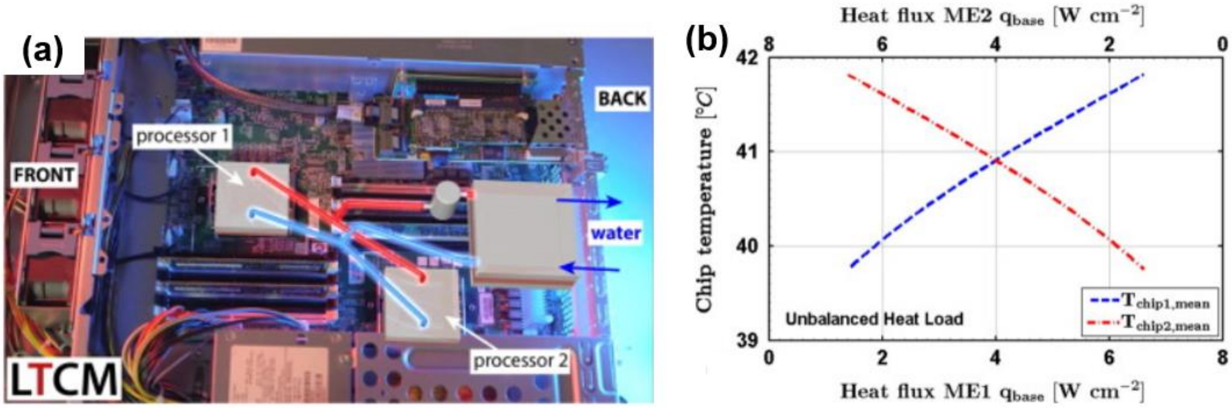

Figure 19: (a) Parallel cooling of Intel Xeon E560 processors, (b) Variation in mean chip temperatures for unbalanced heat load conditions [49].

thermosiphon loop dissipated 33 W/cm^2 using refrigerant R134a as the working fluid and the chip temperature was maintained at 56°C.

Samba et al. [50] developed an evaporator where a microchannel block was used to separate the liquid and vapor chambers in the evaporator. This evaporator was used in a thermosiphon loop with n-pentane as the working fluid to dissipate heat from a prototype of telecommunications outdoor cabinet. The loop was able to dissipate 600 W, and the operating temperature of the cabinet was maintained below 55°C. Whereas, using an air-cooling technique at 55°C operating temperature only 250 W was dissipated. Noie [51] evaluated an integrated loop where the evaporator and the condenser were contained in a single unit as shown in Fig.20. The experimental study was conducted to evaluate the combined effect of filling ratio and aspect ratio on heat transfer performance of the loop.

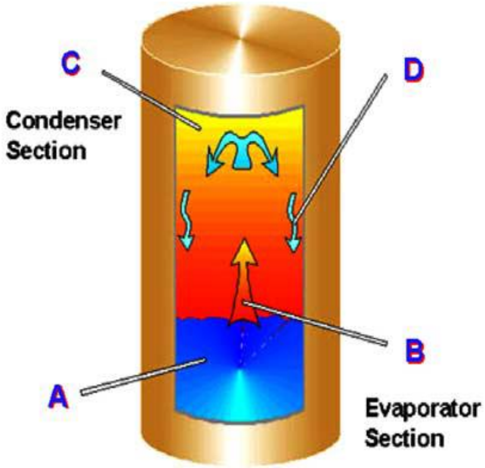

Figure 20: The integrated thermosiphon loop unit studied by Noie et al. [51].

Saenan and Baelmans [52] analytically evaluated the heat transfer performance of three different refrigerants as the working fluids, R134a, R236fa, and R245fa by varying the accumulator volume. Webb et al. [53,54] studied two different working fluids – water, refrigerant R134a, and achieved HTC values greater than 60 kW/m$^{2\circ}$C. Tuma [55] used metallic porous coatings on the heated surface in the evaporator for microprocessor cooling application and obtained HTC of 100 kW/m$^{2\circ}$C. The image of microporous coating and experimental setup are shown in Fig.21.

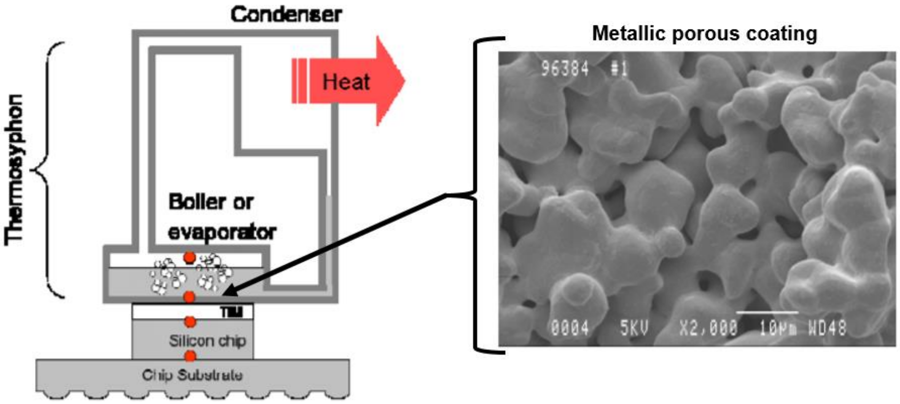

Figure 21: Schematic of the thermosiphon loop used for microprocessor cooling using metallic porous coatings at the interface [55].

Moura [56] used circular cavities in the thermosiphon loop and reduced the temperature of the processor by 26°C. The circular cavities enhances the nucleate boiling thus reducing the pressure drop. The reduced pressure drop enhances the HTC in the gravity driven systems [57,58]. The orientation of the heated surface in the evaporator affects the thermal performance of the thermosiphon loop. The heat transfer performance is reduced for a horizontal surface compared to a vertical configuration [59]. In this research study, the performance of thermosiphon loop is evaluated for horizontally oriented CPU cooling in the data center servers.

Chapter 3

3.0 Research Approach

3.1 Research Need

The currently used air-based cooling techniques are not efficient to dissipate high heat fluxes from CPUs in the data center. Due to large thermal resistances involved in air cooling, extremely low temperature air supply is required to dissipate heat from the servers. To meet the cooling demands, single phase water cooling is adopted for high power density CPUs, but this technique requires continuous pumping power for the fluid flow and hot spots are generated on the CPU surface. Also, the leakage of water can cause severe damage to the processing equipment.

In this work boiling heat transfer is proposed as the efficient solution for high heat flux dissipation using a ‘dual-tapered manifold’ design. Kalani and Kandlikar[34,41] studied flow boiling enhancement using a single taper manifold on a small surface (1 cm^2) where an external pump was used for fluid circulation. The pressure drop (ΔP) affects the pumping power required for the stable volumetric flow rate ($\dot{V}$) in a system as shown by Eq. (1).

$$Power = \Delta P . \dot{V} \tag{1}$$

The aim of this work was to obtain a pumpless self-driven stable fluid flow on a larger heater surface (11 cm^2) for CPU cooling in data centers. Therefore, a dual-taper design was developed to reduce the pressure drop by decreasing the flow length, since external pumping power is not available for driving the flow.

Hypothesis: It is hypothesized that taper manifold provides pressure recovery effect which can be effective to create two-phase flow in tapered microgaps for significantly enhanced pool boiling, and thermosiphon loop heat transfer performances.

3.2 Methodology

The two major boiling heat transfer configurations studied in this work are (a) pool boiling, and (b) thermosiphon loop. A 'dual-tapered manifold block' was used on the heated surface for both configurations to drive the two-phase flow along the expanding tapered region as shown in Fig. 22. The two major design parameters focused in this study are – (a) dual taper angle (α), and (b) inlet gap height (h_i).

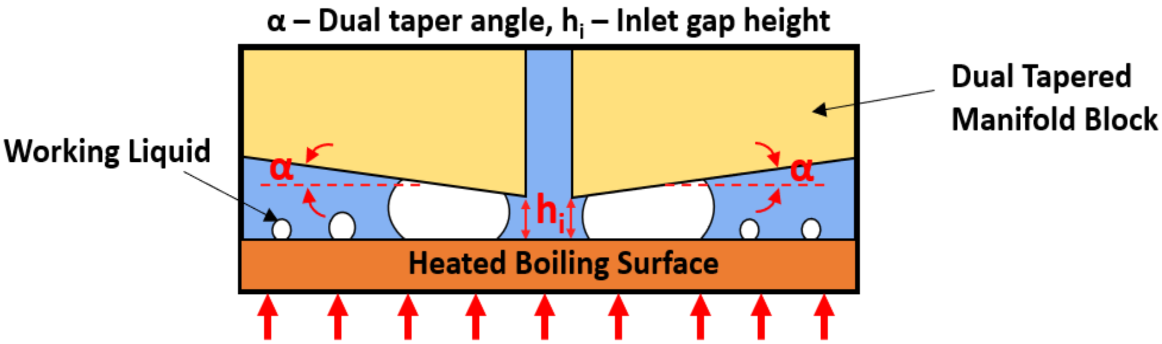

Figure 22: Schematic of dual tapered manifold block on a heated boiling surface.

This design was used to improve the thermal performance of a plain copper surface during pool boiling, and in the evaporator of the thermosiphon loop for CPU cooling. The stable two-phase flow and bubble expansion mechanisms in a tapered microgap during boiling are shown in Fig.23. In the first image, bubble nucleates near the inlet of the tapered microgap and meets the surface of the tapered manifold block. This creates two bubble interfaces - advancing interface and receding interface. The desired flow direction is

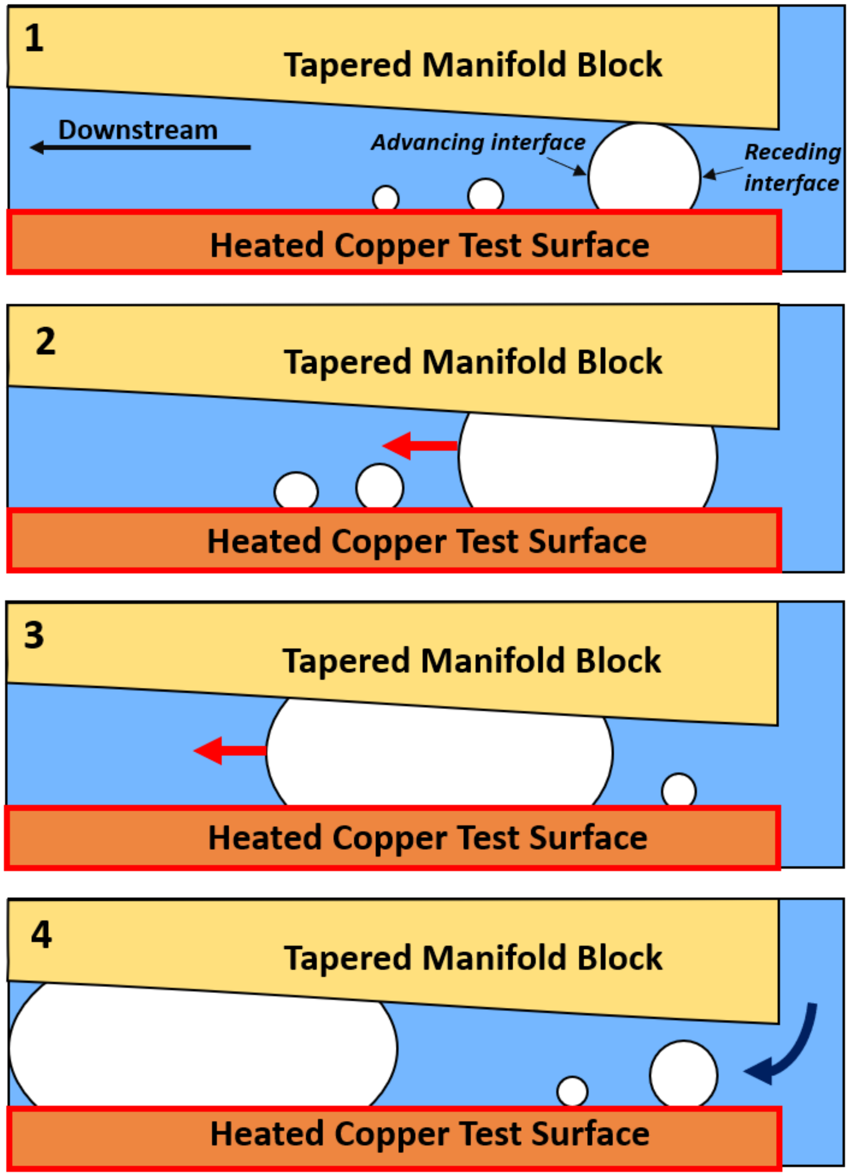

Figure 23: Schematic showing the bubble expansion and departure mechanism in a tapered microgap section.

towards the downstream along the increasing cross-section of the tapered microgap. In the second image, as the bubble continues to grow, it is squeezed between the manifold block and the heated surface. The receding interface is pinned, and the advancing interface moves along the taper as shown by red arrow. In the third image, advancing interface continues to move towards left and receding interface also travels along the taper. This creates free space on the heater surface for bubble nucleation, and a new bubble nucleates near the inlet of the tapered microgap. In the fourth image, the expanding bubble leaves the tapered region, and this creates a liquid pumping effect near the inlet of the microgap as shown by blue arrow. The expanding cross section in the tapered region helps in pressure recovery thus reducing the total pressure drop along the flow and improves the flow stability in the boiling domain. The bubble squeezing mechanism creates a liquid pumping effect from the bulk into the tapered microgap region and this helps in continuous surface rewetting. In a thermosiphon loop, the gravitational head and bubble squeezing mechanism provides the combined liquid pumping effect in the tapered microgap. The pressure recovery and bubble squeezing mechanisms are discussed in detail later in Chapter 4 and Chapter 8, respectively.

The objectives of this research work are, (i) to develop a fundamental theoretical model to predict the pressure recovery, total pressure drop, mass flux, and HTC due to tapered microgap geometry in a pool boiling system to (ii) improve the CHF and HTC of a pool boiling system using dual tapered manifold on a plain copper surface and characterize the performance as a function of geometrical and operating parameters, (iii) evaluate the heat dissipation performance of an innovative evaporator containing the dual tapered manifold in a thermosiphon loop for CPU cooling in data center, and (iv) obtain high speed images of bubble squeezing mechanism in a tapered microgap and present a theoretical analysis.

3.3 Research Layout

The various objectives accomplished in this research and the corresponding chapters are discussed below.

1. ***Chapter 4: Theoretical model for pressure drop and HTC predictions in pool boiling.***

(a) A theoretical model was developed to evaluate the two-phase flow characteristics and effect of different geometric and operational parameters on thermal performance of dual tapered manifold block. The model was developed to predict the pressure drop, pressure recovery, mass flux, and HTC in the tapered microgap region. This helps in establishing a fundamental understanding of the two-phase flow mechanism in the microgap.

2. Chapter 5 and Chapter 6: Pool boiling performance using dual tapered manifold.

(a) The aim of this study was to evaluate the heat dissipation performance of a dual tapered manifold placed on a plain cooper test surface in a pool boiling system, since the current pool boiling heat transfer enhancement studies are focused on surface modifications such as nano-microstructures, porous coatings, and microchannels. Such enhancement techniques involve expensive and highly skilled fabrication processes. The aim is to develop simple, robust, add-on technique to enhance the heat dissipation on a plain surface.

(b) An experimental study was conducted to evaluate the effect of geometrical design parameters - taper angle, and inlet height on the heat dissipation performance. The study was conducted for two different working fluids, water in Chapter 5, and HFE7000 in Chapter 6. The HFE7000 fluid was used considering the electronics cooling application due to its dielectric nature.

(c) The theoretical HTC values from Chapter 4 are presented and compared with the experimental results to validate the theoretical model.

3. ***Chapter 7: Thermosiphon loop for CPU cooling using dual tapered manifold design.***

a) The aim of this study was to design, fabricate, and test an evaporator containing a dual tapered manifold in a thermosiphon loop for CPU cooling in data center using a dielectric liquid (HFE7000) as the working fluid. Thermosiphon loop is a gravity driven system and does not require external pumping power for fluid circulation, hence low operational cost can be achieved for large applications.

b) The heat dissipation performance of thermosiphon loop with dual tapered manifold was evaluated and compared with the commercial air and water-based coolers. These single-phase air and water coolers are currently used for CPU cooling in RIT's data center and the potential of the tapered manifold design was investigated in data center cooling application.

4. ***Chapter 8: High speed imaging and theoretical analysis of bubble squeezing mechanism.***

a) High speed images of bubble squeezing mechanism were obtained in the tapered microgap for different taper angles and inlet gap heights. During this study, the motion of advancing and receding interfaces was tracked to gain insight into the stable and unstable bubble squeezing mechanisms. A preliminary force balance model was also developed to evaluate the effect of multiple forces acting on advancing and receding interfaces.

Chapter 4

4.0 Theoretical Model for Pressure Drop and HTC Prediction in Pool Boiling

A theoretical model was developed to predict the two-phase flow characteristics such as mass flux, pressure recovery, net pressure drop, and the HTC for a tapered microgap in a pool boiling configuration as shown earlier in Fig. 22. The theoretical analysis provides a fundamental insight into the two-phase heat transfer, and this could provide a more efficient optimization approach for tapered microgap based geometry. The approach followed to develop the theoretical model consists of five steps as discussed below.

1. **Input parameters:** The two types of input parameters are, (a) geometric, and (b) operational. The geometric parameters include the design parameters such as taper angle, flow length, inlet gap height, and flow width. The operational parameters include the type of working fluid and the dissipated heat flux at steady state.

2. **Pressure drop model:** The second step is to evaluate the pressure drop and pressure recovery effects and calculate the net pressure drop in the microgap region. Homogeneous flow model was adopted to evaluate the net pressure drop in the boiling region for different input parameters [60]. A detailed discussion on the pressure drop analysis in provided later in this chapter.

3. **Estimate the mass flux:** The third step is to estimate the mass flux at the center of the expanding tapered section. It is assumed a ‘stable operating point’ is achieved when the pressure drop is balanced by the pressure recovery effect for a given set of input parameters. The ‘stable operating point’ suggests that a stable pumpless

two-phase flow is developed in the tapered microgap region. The mass flux values were calculated at ‘stable operating points’ for different input parameters. A detailed discussion on this is presented later in this chapter.

4. **Prediction of heat transfer coefficient (HTC):** The fourth step is to predict the HTC for the obtained ‘stable operating points’. The boiling correlation by Kandlikar [61] was used to predict the HTCs for different estimated mass fluxes. A detailed discussion on the boiling correlation is presented later in this chapter.

5. **Validation of theoretical model:** The fifth step is to validate the theoretical HTC predictions by comparing with the experimentally obtained HTCs for different tapered configurations and working fluids. The validation and accuracy of the model is presented later in Chapter 5 for water and Chapter 6 for HFE7000. A chart representing the summary of the approach used for developing the theoretical model is shown in Fig.24.

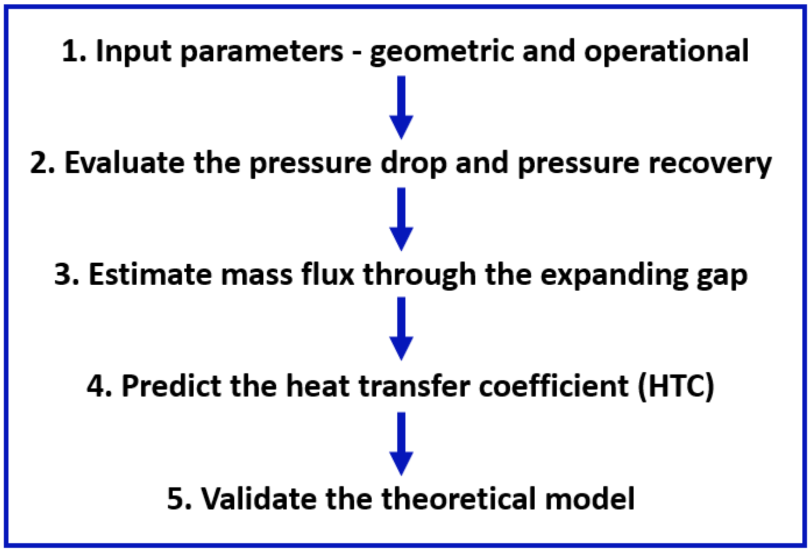

Figure 24: The flow chart representation of the approach adopted for theoretical model.

4.1 Homogeneous Flow Model for Pressure Drop

The homogeneous flow model [60] was used to evaluate the pressure drop and pressure recovery effects for different input parameters. The model was also adopted by Kalani and Kandlikar [62] for flow boiling study in a tapered gap geometry. The equation used to calculate the total pressured drop due to friction, momentum change, gravity, and entrance-exit losses is shown in Eq. (2). The three major assumptions in the homogeneous flow model are, (a) the liquid and vapor phases exist in a thermodynamic equilibrium, (b) a pseudo phase fluid flow in the microgap and the properties of this pseudo fluid are calculated using the actual properties of liquid and vapor phases, and (c) the liquid and vapor phases travel with equal velocities.

$$\int_0^{L_{tp}} -\left(\frac{dP}{dz}\right) dz = \overset{Term\ 1}{\frac{\frac{2f_{TP}G^2 v_f}{D_h}\left[1 + x\left(\frac{v_{fg}}{v_f}\right)\right]}{1 + G^2 x\left(\frac{dv_g}{dP}\right)}} + \overset{Term\ 2}{\frac{G^2 v_{fg}\frac{dx}{dz}}{1 + G^2 x\left(\frac{dv_g}{dP}\right)}} + \overset{Term\ 3}{\frac{\frac{Sin\Theta}{v_{fg}\left[1 + x\left(v_{fg}/v_f\right)\right]}}{1 + G^2 x\left(\frac{dv_g}{dP}\right)}} + \overset{Term\ 4}{\Delta P_e} \qquad (2)$$

The first term - ‘Term 1’ on the right side represents the pressure drop in the microgap due to friction. This pressure drop is due the fluid viscosity and shear stress at the walls. The second term – ‘Term 2’ on the right side represents the pressure drop due to momentum change in a boiling system. During the bubble expansion period, the evaporation i.e., mass transfer from liquid to vapor phase occurs across the liquid-vapor interface. Since the total mass remains conserved across the interface, as a result, a sudden increase in the interface velocity is observed along the downstream direction. Due to this phenomenon a pseudo force is experienced against the flow direction, therefore creating a pressure drop along the flow domain. This pressure drop is represented as the pressure drop due to momentum change. The third term – ‘Term 3’ on the right side represents the pressure drop due to gravity. In this pool boiling study, the boiling surface is always oriented parallel to the ground ($\Theta = 0°$). Therefore, pressure drop due to gravity is not considered in this study. The fourth term – 'Term 4' on the right side represents the pressure drop due to entrance and exit losses for the tapered microgap geometry.

In Eq.(2) L_{tp} is the total flow length of the two-phase region, dz is the element length along the flow direction, dP is the pressure drop along element dz, θ is the angle of inclination with respect to the horizontal plane, v_g is the specific volume of vapor phase, v_f is the specific volume of liquid phase, v_{fg} is the difference in the specific volumes of the vapor and liquid phases, G is the mass flux, D_h is the hydraulic diameter, f_{TP} is the two phase friction factor, and x is the exit quality.

The exit quality is calculated using Eq. (3), where $\mathrm{h_{fg}}$ is the latent heat, q" is the heat flux, A_c is the area of section cross of the tapered microgap, and ṁ is the mass the flow rate.

$$x = \frac{1}{\mathrm{h_{fg}}}\left[\left(\frac{\mathrm{q''}A_c}{\dot{\mathrm{m}}}\right)\right] \qquad (3)$$

The two-phase friction factor (f_{TP}) was calculated using the Blasius equation as given by Eq. (4).

$$f_{tp} = 0.079\left(\frac{GD_h}{\mu_{tp}}\right)^{-0.25} \qquad (4)$$

In Eq. (4) the two-phase viscosity (μ_{tp}) is calculated by McAdams et al.[63] equation using liquid and vapor phase viscosities as given by Eq. (5), where μ_g and μ_f are the dynamic viscosities of vapor and liquid phases.

$$\frac{1}{\mu_{tp}} = \frac{x}{\mu_g} + \frac{1-x}{\mu_f} \qquad (5)$$

The pressure recovery per unit flow length due to the increasing cross-section area in the tapered microgap is calculated using Eq. (6), where dA/dz represents the change in cross-sectional per unit flow length.

$$\left(\frac{dP}{dz}_{taper\ area}\right) = \frac{\frac{2G^2 v_f}{A_c}\left[1 + x\left(\frac{v_{fg}}{v_f}\right)\right]\frac{dA}{dz}}{1 + G^2 x\left(\frac{dv_g}{dp}\right)} \qquad (6)$$

The net pressure drop was calculated considering the pressure drop from Eq.(2) and pressure recovery from Eq.(6). The pressure recovery due to taper balances the pressure drop due to friction, momentum change, and entrance-exit losses. When this condition is satisfied, a 'stable operating point' is obtained, and the mass flux value is estimated at the mid cross-section of the tapered section. The mass flux values at the 'stable operating points' were used in the boiling correlation by Kandlikar [61] to obtain the HTC values. The heat transfer correlation is presented in the next section.

4.2 Heat Transfer Correlation

The boiling correlation by Kandlikar [61] was used to calculate the HTC for different mass fluxes obtained from the pressure drop analysis. This boiling correlation was developed for flow boiling systems but since a local flow boiling heat transfer is developed in the tapered microgap, the correlation was used in this pool boiling study.

The boiling correlation used to predict the HTC is shown by Eq. (7), where h_f is the single-phase heat transfer coefficient, Co is the convection number, Bo is the boiling number, F_f is the liquid dependent parameter, and C_1 to C_4 are the constants.

$$\frac{HTC}{h_f} = C_1 Co^{C_2} + C_3 Bo^{C_4} F_f \qquad (7)$$

The single-phase heat transfer coefficient, convection number, and boiling number were calculated using the Eqs. (8 - 10).

$$h_f = 0.023 Re_f^{0.8} Pr_f^{0.4} \left(k_f / D_h\right) \qquad (8)$$

$$Co = \left(\frac{1-x}{x}\right)^{0.8} \left(\frac{\rho_g}{\rho_f}\right)^{0.5} \qquad (9)$$

$$Bo = \frac{q^{"}}{G h_{fg}} \qquad (10)$$

In the above equations, Re_f is the liquid Reynolds number, Pr_f is the liquid Prandtl number, k_f is thermal conductivity of the liquid, $D_h$is the hydraulic diameter, ρ_f is liquid density, ρ_g is vapor density, h_{fg} is latent heat of vaporization, G is mass flux, and $q^{"}$ is the heat flux.

The theoretical model was used for water, and HFE7000 as the working fluids. The theoretical predictions form the pressure drop analysis is presented in the following section.

4.3 Results of Pressure Drop Analysis for Water

The theoretical pressure drop analysis, and mass flux estimation for water as the working fluid are presented in this section. The calculations were performed for two different taper angles (α) 10°, and 15° with 1.27 mm inlet gap height (h_i). The bubble departure diameter in pool boiling with water is ~ 2.5 mm, hence the inlet gap height was selected considering the bubble squeezing mechanism near the inlet of the microgap.

The net pressure drop plots at different heat fluxes were obtained for 15°, and 10° taper angles using homogeneous flow model. In Fig. 25 for 15° taper angle, the net pressure drop (kPa) is shown along the Y-axis, and mass flux (kg/m^{2}s) at the mid-section of the tapered microgap is shown along the X-axis. The pressure drop curves were plotted for various heat fluxes which are represented by different colored lines, these heat flux values were obtained from the experimental study. The x-intercept of the pressure drop curves provide the 'stable operating points' as shown by block dots. The 'stable operating point' is obtained by balancing the pressure drop due to friction, momentum change, entrance-exit losses by pressure recovery due to expanding cross-section. It is assumed that a stable two-phase flow is achieved in the tapered microgap configuration when pressure drop is balanced by the pressure recovery effect. The mass fluxes at the 'stable operating points' were obtained from the pressure drop analysis for heat fluxes, 101 W/cm^2 to 287 W/cm^2.

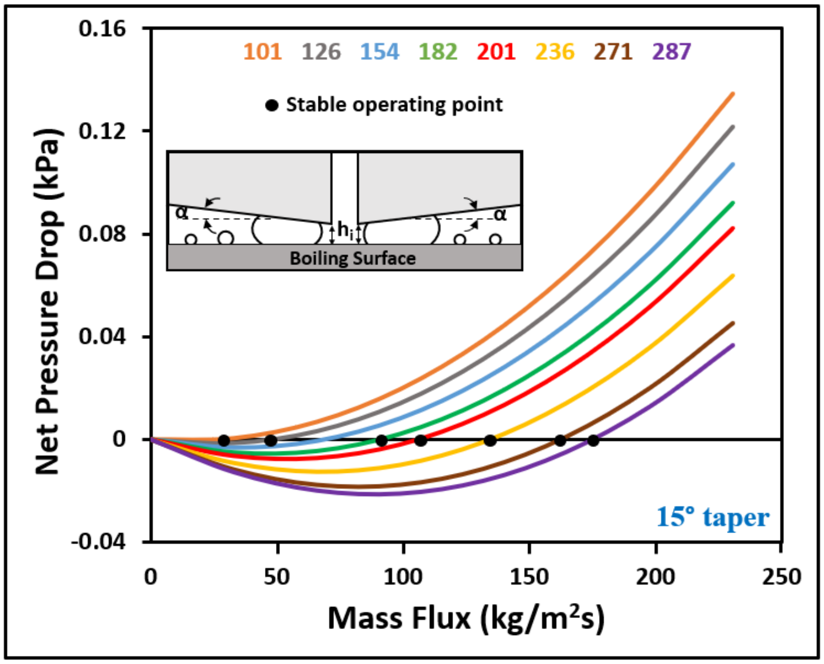

Figure 25: The pressure drop curves at various heat fluxes for 15° taper angle (α) and 1.27 mm inlet gap height (h_i). The colored numbers represent the heat flux in W/cm^2.

In Fig. 26 for 10° taper angle, the net pressure drop curves were obtained for heat fluxes, 38 W/cm^2 to 218 W/cm^2 based on the experimental data. Similar to 15° taper, the different heat fluxes are represented by colored lines. For the given range of heat flux, no x-intercept was obtained, hence no 'stable operating point' can be achieved using the pressure drop analysis based on homogeneous flow model. Therefore, no stable two-phase flow can be achieved since pressure drop is always greater than the pressure recovery effect for 10° taper angle with 1.27 mm inlet gap. But stable flow conditions were achieved for this geometric configuration and heat transfer enhancement was obtained during the experimental study as discussed later in Chapter 5. The bubble squeezing mechanism in the tapered microgap develops the required pumping head for stable-phase flow. The effect of bubble squeezing mechanism is not included in the pressure drop model, hence this geometric configuration presents the limitation of this theoretical approach.

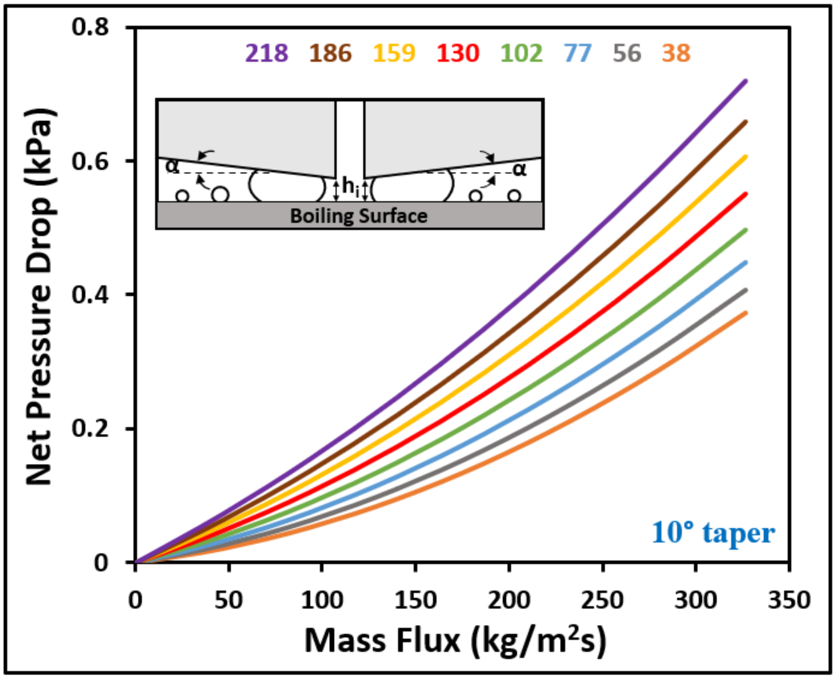

Figure 26: The pressure drop curves at various heat fluxes for 10° taper angle (α) and 1.27 mm inlet gap height (h_i). The colored numbers represent the heat flux in W/cm^2.

The mass flux values obtained from the pressure drop analysis at 'stable operating points' for 15° taper and 1.27 mm inlet gap height are shown in Fig. 27. These values were used in the boiling correlation to predict HTC at different heat fluxes. The HTC predictions are shown later in Chapter 5 while comparing the predicted values with experimental values.

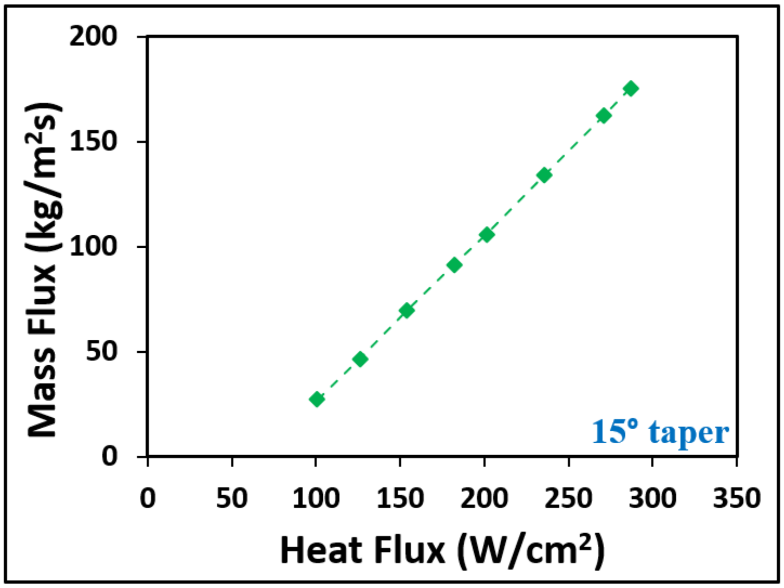

Figure 27: The estimated mass flux values at different heat fluxes for 15° taper angle with 1.27 mm inlet gap height.

4.4 Results of Pressure Drop Analysis for HFE7000

The theoretical pressure drop analysis, and mass flux estimation for HFE7000 as the working fluid are presented in this section. The calculations were performed for five different taper angles (α) - 5°, 10°, 15°, 20° and 25° for two inlet gap heights (h_i) - 0.8mm, and 1.27 mm. The bubble departure diameter in pool boiling with HFE7000 is ~ 1.7 mm, hence the inlet gap height was selected considering the bubble squeezing mechanism near the inlet of the microgap.

5° to 25° taper angles with 0.8 mm inlet gap height: The pressure drop analysis for 5°, and 10° taper angles with 0.8 mm inlet gap height is shown in Fig. 28. The net pressure drop (kPa) is shown along the Y-axis, and mass flux (kg/m^{2}s) at the mid-section of the tapered microgap is shown along the X-axis. The pressure drop curves were plotted for various heat fluxes which are represented by different colored lines, these heat flux values were obtained from the experimental study.

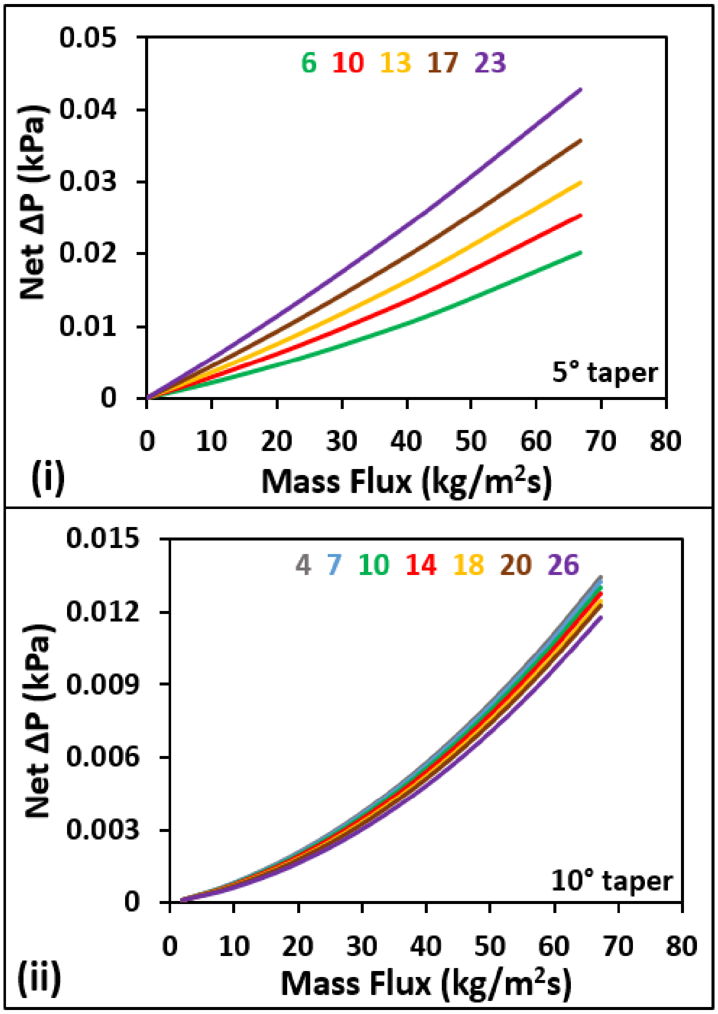

Figure 28: The pressure drop curves at various heat fluxes for 5°, and 10° taper angles with 0.8 mm inlet gap height. The colored numbers represent the heat flux in W/cm^2. No stable operating points were obtained for these cases.

The net pressure drop curves do not intersect with the mass flux axis for any heat flux value. This suggests that pressure drop is always greater than the pressure recovery effect for 5°, and 10° taper angles. Therefore, 'no stable operating' point i.e., operating mass flux value can be obtained using the homogeneous flow model. Similar to water pool boiling in 10° taper angle, the bubble squeezing mechanism is responsible for providing the pumping head for two-phase flow in 5°, and 10° taper angles with 0.8 mm inlet gap. In these two configurations, the pressure recovery effect is small hence reduced CHF was obtained compared to ‘no manifold block’ configuration as discussed later in the experimental study in Chapter 6.

Figure 29, shows the pressure drop analysis for 15°, 20°, and 25° taper angles with 0.8 mm inlet gap height. For 15° taper angle, no x-intercept was obtained for heat flux less than 9 W/cm^2, hence no mass flux corresponding to the ‘stable operating point’ can be achieved. For 20°, and 25° taper angles, ‘stable operating points’ were obtained for heat fluxes in the range of 5 W/cm^2 to 30 W/cm^2.

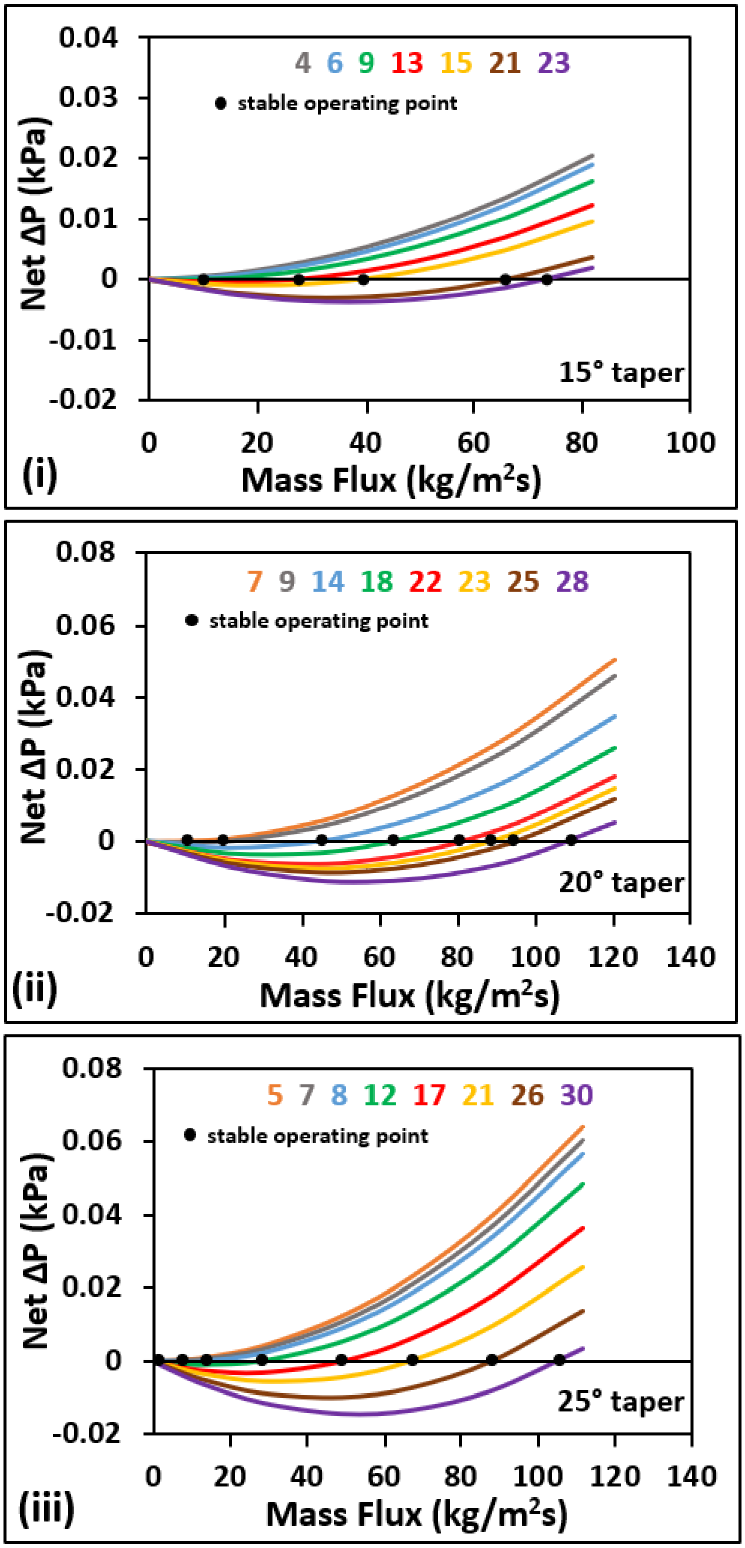

Figure 29: The pressure drop curves at various heat fluxes for 15°, 20°, and 25° taper angles with 0.8 mm inlet gap height. The colored numbers represent the heat flux in W/cm^2.

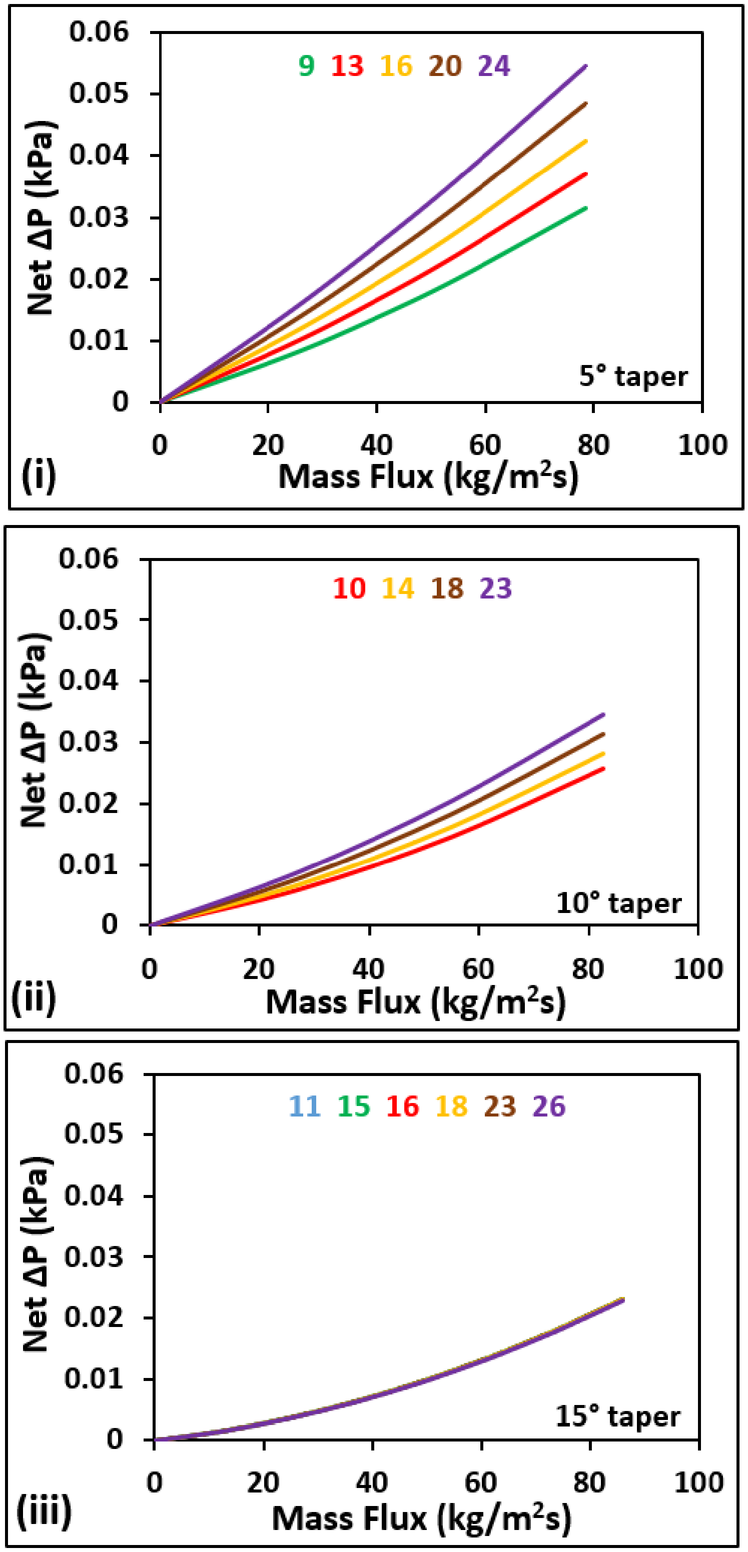

Figure 30: The pressure drop curves at various heat fluxes for 5°, 10°, and 15° taper angles with 1.27 mm inlet gap height. The colored numbers represent the heat flux in W/cm^2. No stable operating points were obtained for these cases.

5° to 25° taper angles with 1.27 mm inlet gap height: The plots obtained from the pressure drop analysis for 5°, 10°, and 15° taper angles with 1.27 mm inlet gap height are shown in Fig. 30. Similar to previous representations, the net pressure drop (kPa) is shown along the Y-axis, and mass flux (kg/m^{2}s) at the mid-section of the tapered microgap is shown along the X-axis. The different colored numbers in represent the heat flux (W/cm^2) values obtained from the experimental study. For 5°, 10°, and 15° taper angles, no x-intercept was obtained hence no 'stable operating point' can be achieved based on the homogeneous flow model. For these configurations, the pressure recovery effect along the flow domain is less than the pressure drop, therefore reduced CHFs were obtained for these taper angles as discussed later in the experimental study in Chapter 6.

Figure 31 shows the pressure drop analysis for 20°, and 25° taper angles. For 20° taper, the 'stable operating points' were not obtained for heat fluxes less than 24 W/cm^2, and for 25° taper, no 'stable operating points' were achieved for heat fluxes less than 15 W/cm^2. At low heat fluxes the pressure drop dominates over the pressure recovery effect, hence net pressure drop is always greater than zero. The theoretical approach is based on homogeneous flow model and does not include pumping effect of the bubble squeezing mechanism, and at low heat fluxes the bubble squeezing mechanism significantly drives the two-phase flow in the tapered microgap.

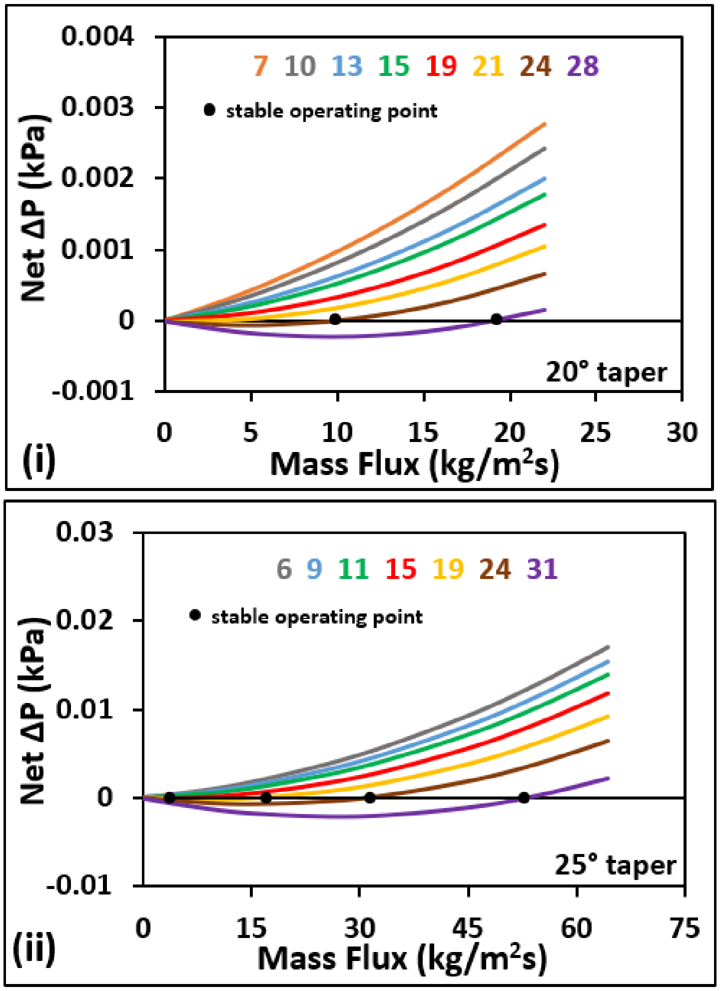

Figure 31: The pressure drop curves at various heat fluxes for 20°, and 25° taper angles with 1.27 mm inlet gap height. The colored numbers represent the heat flux in W/cm^2.

The mass fluxes obtained from the pressure drop analysis for various taper angles and inlet gap heights are shown in Fig. 32. These values were used in the boiling correlation to predict HTC at different heat fluxes. The HTC predictions are shown later in Chapter 6 while comparing the predicted values with experimental values.

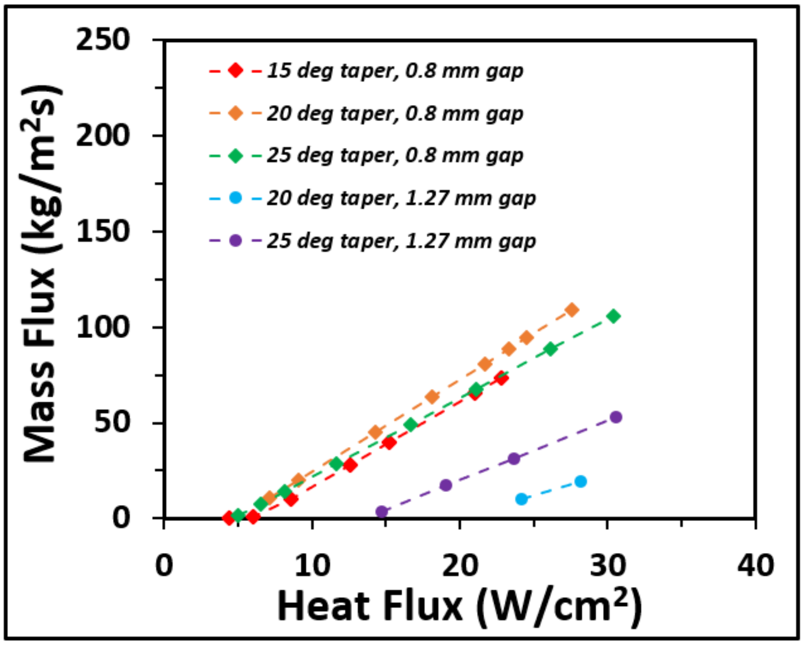

Figure 32: The predicted mass flux values at 'stable operating points' for different geometric configurations.

4.5 Major Outcomes of the Theoretical Analysis

The theoretical model based on homogeneous flow model and boiling heat transfer correlation was developed to predict the two-phase flow characteristics - mass flux, pressure recovery, net pressure drop, and the HTC for a tapered microgap in a pool boiling system. The ‘stable operating points’ were obtained for various geometric configurations and heat fluxes with water, and HFE7000 as the working fluids. The stable operating point is obtained when pressure recovery balances the pressure drop, this denotes that stable two-phase flow will be established in the microgap. It was observed that for smaller taper angles, and low heat fluxes, pressure recovery is less than pressure drop hence no ‘stable operating points’ were obtained. For such cases, bubble squeezing effect provides the driving force for fluid flow as discussed later in Chapter 8. For HFE7000 with smaller taper angles, reduced CHF values were recorded during the experimental study as discussed later in Chapter 6 suggesting flow instabilities in the tapered microgap. This shows that pressure recovery effect is critical in obtaining the enhanced heat dissipation performance. For cases where pressure recovery was able to balance the pressure drops with sustained two-phase flow, the HTC values were predicted and validated by comparing with experimental findings shown later in Chapter 5 for water, and Chapter 6 for HFE7000.

Chapter 5

5.0 Pool Boiling Performance of Dual Tapered Manifold with Water

In this study, a dual tapered manifold block was used on a plain copper surface with water as the working fluid in a pool boiling system. An experimental study was conducted with two different taper angles and enhancement in CHF and HTC was evaluated. The experimental setup, experimental procedure, data reduction, heat transfer results, and conclusion of the study are presented in this chapter.

5.1 Experimental Setup

The schematic of experimental setup used in the pool boiling study with water as the working fluid is shown in Fig.33. The two main sub-assemblies in the setup are the boiling test section contained in the water reservoir, and a copper heater block assembly. An aluminum block was used as the reservoir to contain the saturated water, and the boiling test section was fixed at the bottom face of the aluminum block. A cartridge heater was immersed in the water to maintain saturation temperature throughout the study. A ceramic chip holder was designed and fabricated to hold the copper test chip and minimize the heat losses from the test chip. The edges of the test surface were covered by kapton tape to project 10mm ×10mm area for the heat dissipation. A dual-tapered manifold block containing the dual taper was secured over the plain copper chip and a steel plate of thickness 1.27 mm was used between the manifold block and copper test chip to provide desired inlet gap height. The manifold was machined from polysulfone material which has a glass transition temperature of 185°C. Two different dual taper angles tested in this study were - 10°, and 15°. The front and rear sides of the aluminum block were enclosed by high

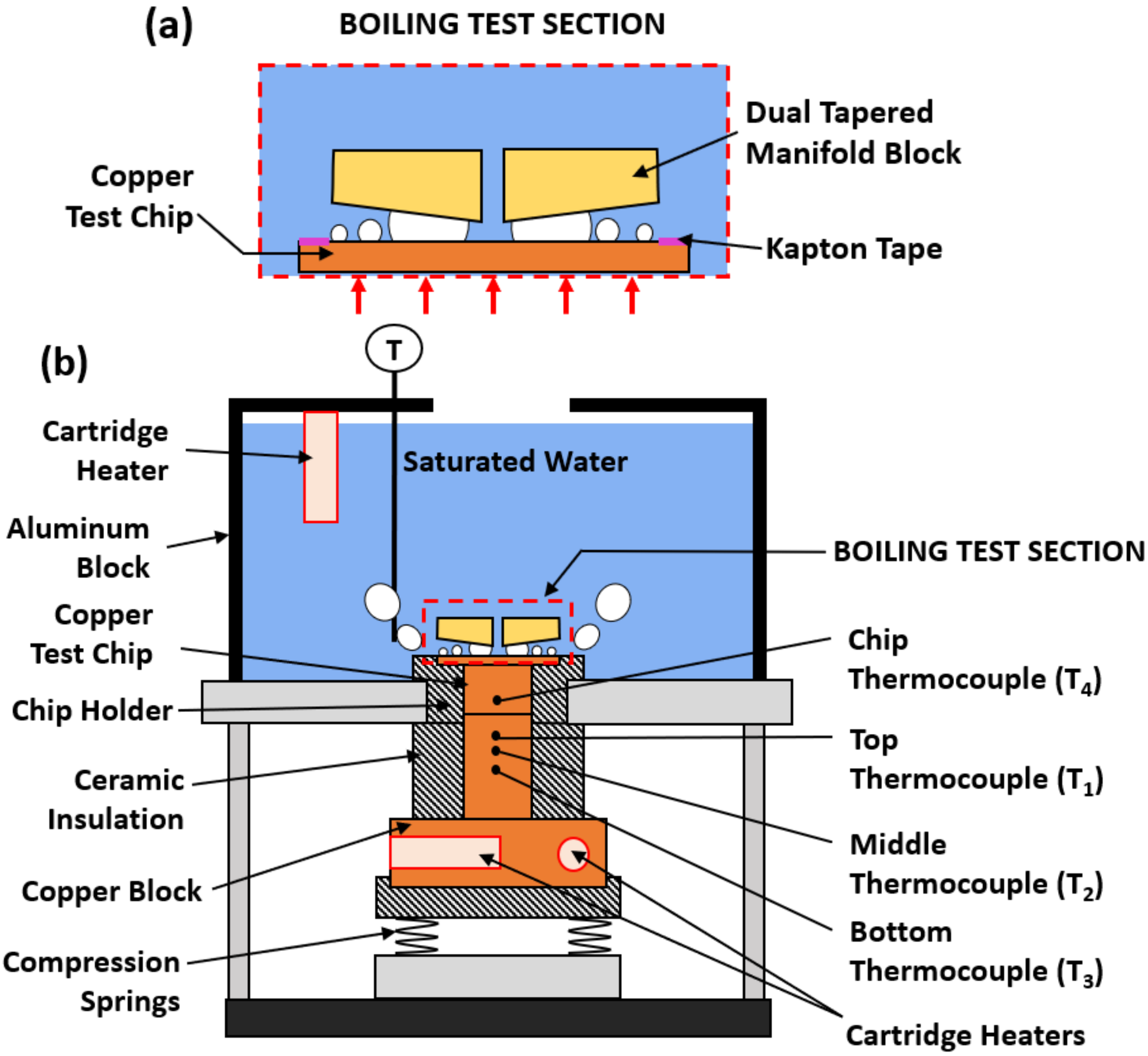

Figure 33: Schematic representations of (a) boiling test section with dual tapered manifold block, and (b) pool boiling experimental setup with water. (Schematics are not to scale)

temperature resistant borosilicate glass for clear visualization. Below the boiling test section, a copper heater block containing four cartridge heaters (200 W each) was secured in direct contact with the copper test chip. The cartridge heaters were connected to an external dc power supply. The copper heater block consists an extended stem with cross section 10 mm × 10 mm, matching the dimensions of copper test chip's stem. The stem of the copper heater block was enclosed by a ceramic sleeve to minimize the heat losses. Four

K-type thermocouples (T_1-T_4) were used for temperature measurement along the heater block and test chip stems. The copper heater block was supported on a ceramic plate using four compression springs. The compression springs were used to maintain a good contact between the copper test chip and copper heater block. A grafoil sheet was also used between the copper test chip and copper heater block to further reduce the thermal contact resistance.

5.2 Experimental Procedure

The procedure followed while conducting experiments for all the tapered configurations is discussed in this section.

- **Step 1:** Distilled water was filled in the aluminum reservoir and the cartridge heater immersed in the water was turned on to heat the water till saturation temperature.
- **Step 2:** The thermocouples in the test setup were connected to the cDAQ device. The setup was monitored by a Labview VI program and the National Instruments cDAQ – 9174 and MOD – 9211.
- **Step 3:** The external power supply was turned on and power was supplied to the four cartridge heaters in the copper block. The voltage was increased in steps of 5V for each data point.
- **Step 4:** The temperature readings were recorded at steady state for all heat fluxes. For every heat flux, 80 data points were collected from all the thermocouples. The steady state was indicated by the LabVIEW program when the temperature variations was less than 0.1 ^{o}C for all thermocouples for 20 minutes.

- **Step 5:** The heat transfer parameters – heat flux, wall superheat, and HTC were calculated as discussed in the following ‘data reduction’ section.

5.3 Data Reduction

The one-dimensional heat conduction in the copper heater assembly is shown in Fig.34. The heat dissipation parameters - heat flux (q"), heat transfer coefficient (HTC) and, wall superheat (ΔT_{sat}) were calculated to evaluate the performance of dual-tapered manifold block using the following equations.

The heat flux conducted through the copper column was calculated using Fourier’s law for 1D conduction:

$$q'' = -k_{Cu} dT/dx \qquad (11)$$

The temperature gradient (dT/dx) along the heater was calculated using Taylor’s three-point backward difference formula, as shown by Eq.12.

$$\frac{dT}{dx} = \frac{3T_1 - 4T_2 + T_3}{2\Delta x} \qquad (12)$$

The temperature values were recorded using four K-type thermocouples (T_1 to T_4) as shown in Fig.34. The heater block was insulated from all sides using a ceramic sleeve.

The spacing between successive thermocouples, $T_1 – T_2$, and $T_2 – T_3$ (Δx) was 5 mm. The surface temperature (T_s) was then calculated using the temperature gradient (dT/dx), the top thermocouple temperature (T_4), and the distance between the top thermocouple and the surface (x_1), 7.1 mm.

$$T_s = T_4 + \frac{dT}{dx} x_1 \qquad (13)$$

The wall superheat (ΔT_{sat}) was calculated using the surface temperature and the saturation temperature of the liquid (T_{sat}), as shown by Eq.14.

$$\Delta T_{sat} = T_s - T_{sat} \tag{14}$$

HTC was calculated using the heat flux (q''), and wall superheat (ΔT_{sat}), as shown by Eq.15.

$$HTC = \frac{q''}{\Delta T_{sat}} \tag{15}$$

The uncertainty analysis was conducted for all the heat transfer parameters and for detailed discussion on uncertainty calculation please refer Appendix. The uncertainty values for heat flux and HTC are shown as error bars in the Section 5.4.

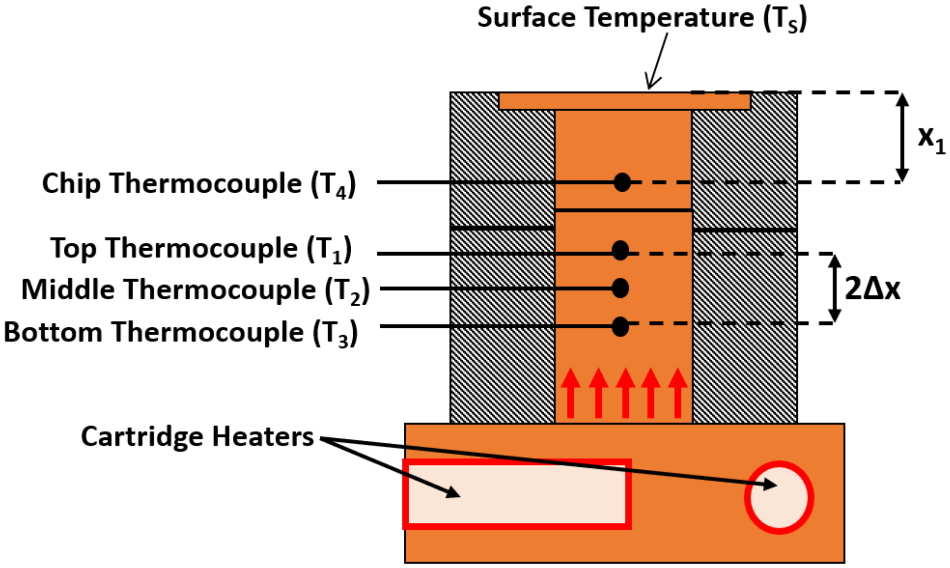

Figure 34: Heat flow in copper heater block in the pool boiling setup with water.

Validation of one-dimensional heat conduction: The heat transfer parameters were calculated assuming one-dimensional heat conduction through the stem of the copper heater block. Therefore, a linear temperature gradient is expected through the thermocouples, T_3 to T_1. The temperature variation along the stem of the heater at three thermocouple locations for 15° taper angle is shown in Fig. 35. The linear equations for different heat fluxes are shown in the plot, and the linear regressions (R^2) for the heat fluxes tends to 1. This proves the authenticity of the linear temperature profile and the one-dimensional heat conduction. This assumption was validated for all the experimental configurations by plotting the temperature variation at equidistant thermocouple locations along the heater stem.

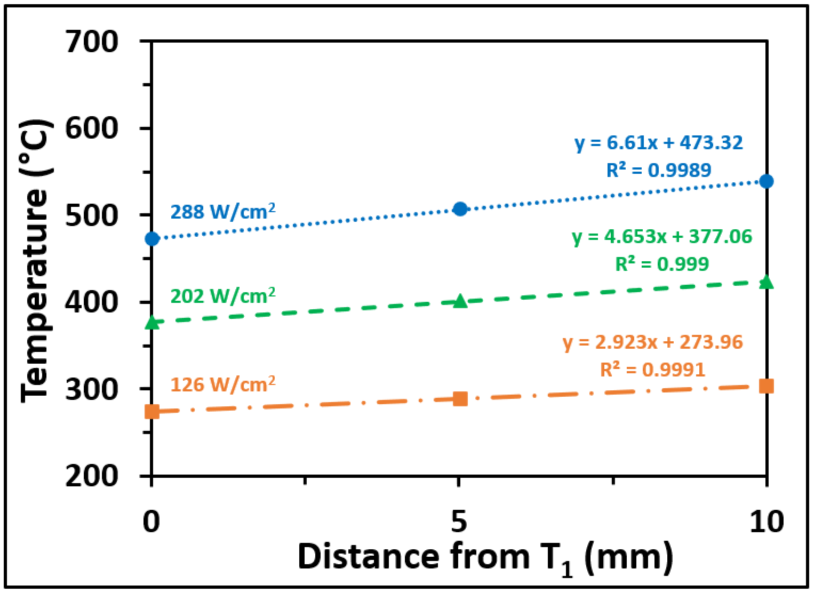

Figure 35: The temperature variation at different heat fluxes along the copper heater block for 15° dual taper angle.

5.4 Experimental Results for Enhancement on Plain Surface

The effect of taper angle on heat flux dissipation, and HTC was evaluated in this study. The performance plots showing the variation in heat flux with respect to wall superheat, and HTC with respect to heat flux are presented in this section.

5.4.1 Effect of Taper Angle on Critical Heat Flux (CHF)

The pool boiling curves showing the variation in heat flux (W/cm^2) with respect to wall superheat (°C) are shown in Fig.36. The units W/cm^2 are used for heat flux to follow the convention used in electronics cooling application. The heat dissipation performances of the dual-tapered manifolds with 10° and 15° taper angles are compared with the ‘no manifold block' baseline configuration, where no manifold block was placed on the top of plain copper surface. Both dual tapered manifold blocks dissipate higher heat fluxes compared to the 'no manifold block' configuration for all wall superheats. The highest CHF achieved was 288 W/cm^2 for 15° angle at a wall superheat of 24.1°C. The CHF obtained for the 10° angle was 218 W/cm^2 at a wall superheat of 20.5°C. The 'no manifold block' configuration resulted in a CHF of 124 W/cm^2 at a wall superheat of 23.8°C. A 2.3X enhancement in CHF was obtained with 15° dual taper compared to 'no manifold block' configuration.

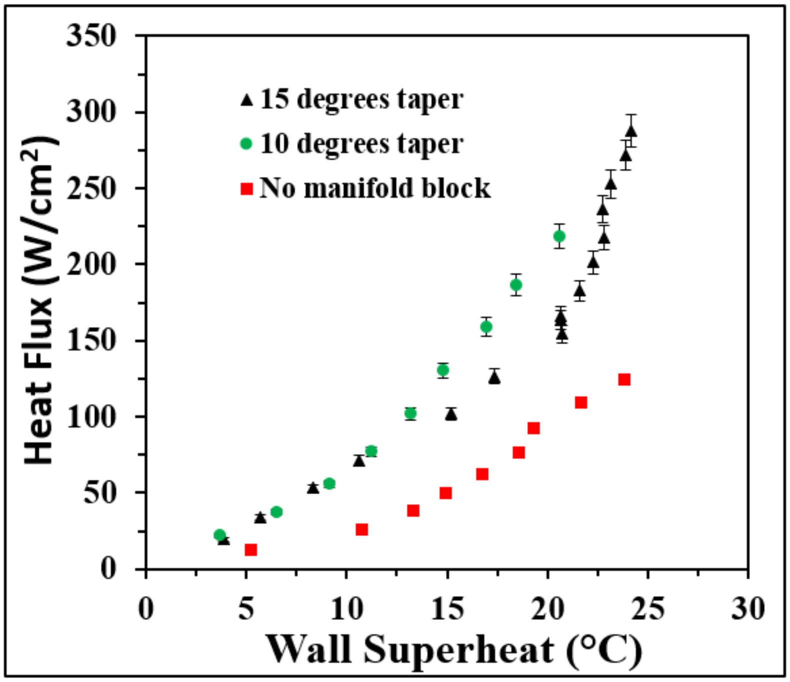

Figure 36: Pool boiling curves showing the performance of 10° and 15° dual taper angle and comparison with 'no manifold block' configuration.

5.4.2 Effect of Taper Angle on Heat Transfer Coefficient (HTC)

The variation in HTC (kW/m^2°C) at different heat fluxes (W/cm^2) for 15° dual taper, 10° dual taper, and 'no manifold block' baseline configuration are shown in Fig.37. The manifold block for both-10° and 15° dual taper angles achieved higher HTC values for all the heat fluxes compared to ‘no manifold block’. This suggests a greater heat dissipating efficiency is achieved using dual tapered manifold configurations. The maximum HTC values for 10°, 15°, and ‘no manifold block’ were 106 kW/m^2°C, 119 kW/m^2°C, and 52.5 kW/m^2°C respectively. The maximum HTC values were obtained at CHF for all configurations.

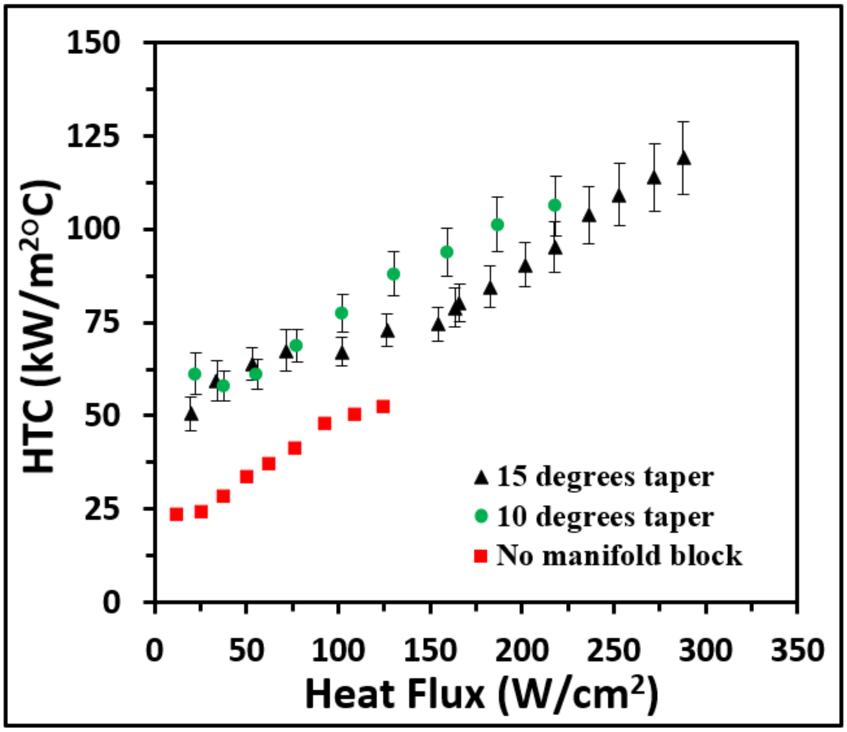

Figure 37: The variation in heat transfer coefficient (HTC) at different heat fluxes for 15° dual taper, 10° dual taper, and 'no manifold block’ configurations.

5.4.3 Two-Phase Flow Mechanism Created by Dual Tapered Manifold Block

The liquid flow from bulk into the dual tapered manifold block and two vapor outlets are shown in Fig.38. The vapor columns at the exit of manifold block are shown by red dotted lines, the liquid inflow direction is shown by blue arrow, and the inlet slot is shown by blue dashed lines. The image was captured during the experimental study at 140 W/cm^2 for 15° taper angle. A stable liquid inflow and vapor outflow mechanism was observed at high heat fluxes, thus showing efficient working of the dual taper design at high heat load conditions. In the tapered microgap region, the bubble squeezing mechanism provides the liquid pumping effect on the heating surface thus developing continuous surface rewetting mechanism in the microgap. And the pressure recovery along the taper due to continuous increase in cross-section area helps in achieving reduced pressure drops, therefore the pumping action provided by the bubble squeezing mechanism is able to establish stable two-phase flow in the tapered region. This transforms a pool boiling system into a local flow boiling system since higher fluid velocities are achieved using tapered microgap design compared to conventional pool boiling systems, and enhanced CHF and HTC values are obtained. A detailed analysis on bubble squeezing mechanism and interface velocities is presented later in Chapter 8.

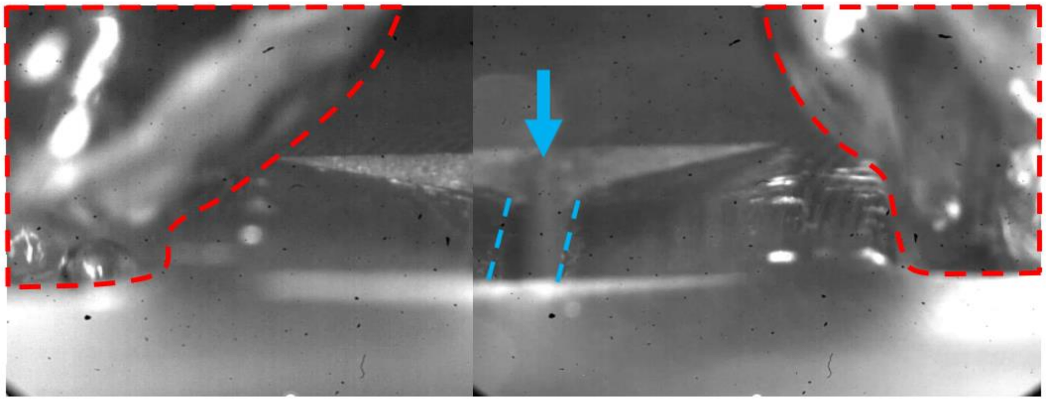

Figure 38: The image showing the establishment of two vapor columns with a central liquid inlet at 140 W/cm^2 for 15° dual tapered manifold block.

5.5 Theoretical HTC Results and Experimental Validation

The estimated mass flux values were used in the boiling heat transfer correlation by Kandlikar [61] to predict the HTC values at different heat fluxes as discussed earlier in Chapter 4. The predicted HTC values and the comparison with experimental results is shown in Fig. 39. It was observed that the theoretical model underpredicts the HTC values for all the heat fluxes. The theoretical model does not include the effect of bubble squeezing mechanism, hence the additional mass flux established in the tapered microgap due to the pumping head provided by bubble squeezing is not included in the estimated mass flux values. This concludes that bubble squeezing mechanism is critical for 15° taper angle with 1.27 mm inlet gap height for the range of heat fluxes, 101 W/cm^2 to 287 W/cm^2.

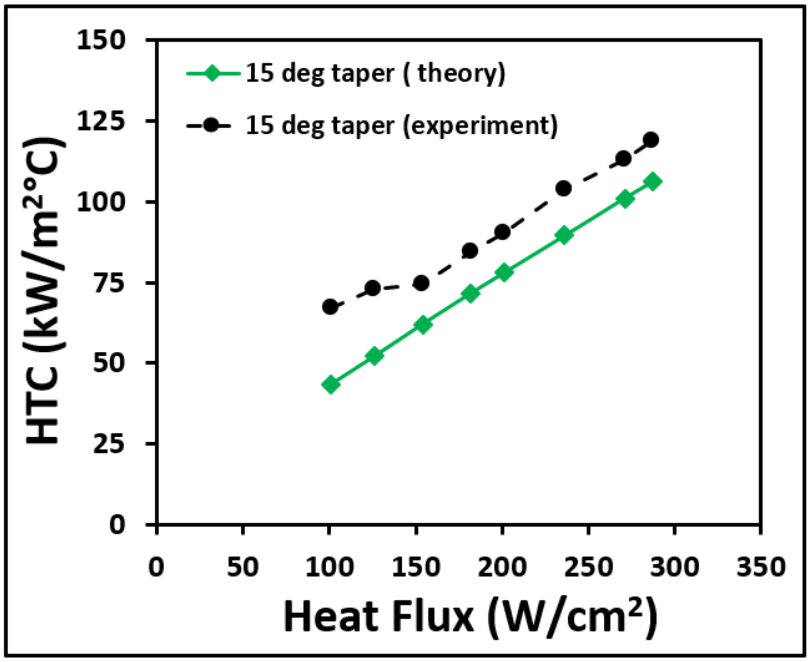

Figure 39: The predicted HTC values and the comparison with experimental results.

Table 2 shows the estimated mass flux, predicted HTC values, experimental HTC values, and the percentage deviation in the theoretical and experimental results. The deviation between theoretical and experimental HTC values decreases with increase in heat flux. The two-phase flow in the tapered microgap is driven by heat flux, hence better accuracy is achieved at high heat fluxes.

Table 2: Comparison between the theoretical and experimental HTC values for 15° dual taper and 1.27 mm inlet gap height with water.

Heat Flux$_{exp}$ (W/cm^2)	**Mass Flux$_{theory}$ (kg/m^{2}s)**	**HTC$_{theory}$ (kW/m^{2o}C)**	**HTC$_{exp}$ (kW/m^{2o}C)**	**Deviation %** $\left\lvert\frac{HTC_{exp} - HTC_{theory}}{HTC_{exp}}\right\rvert \times 100$
101	52.8	43.5	67	35%
126	65.3	52.3	72.9	28%
154	80.6	62	74.5	17%
182	95.8	71.7	84.5	15%
201	105.6	78	90.5	14%
236	124.1	89.6	103.8	14%
271	143.2	101.1	113	11%
287	151.4	106.3	119	11%

5.6 Major Outcomes from Experimental Study and Theoretical Analysis

Experimental Study: The dual taper angles of 10° and 15° achieved higher CHF and HTC values compared to 'no manifold block' configuration. Therefore, efficient high heat flux dissipation can be achieved using a dual tapered design on a plain surface. The CHF values obtained for 15°, 10°, and 'no manifold block' configurations were 288 W/cm^2, 218 W/cm^2, and 124 W/cm^2 at the wall superheats of 24.1°C, 20.5°C, and 23.8°C, respectively. The maximum HTC values for these configurations were 106 kW/m^2°C, 119 kW/m^2°C, and 52.5 kW/m^{2o}C. A 2.3X enhancement in CHF and HTC was obtained using a dual tapered manifold design on a plain copper surface. The dual taper design can significantly improve the performance of a plain surface and expensive surface enhancement techniques such as microporous coatings, and nano-microstructures are not required.

A stable two-phase flow mechanism was observed in the dual tapered manifold configuration at high heat fluxes. This shows the efficiency of bubble squeezing and pressure recovery mechanism at high heat flux conditions. The high fluid velocities established in tapered microgap region develops a local flow boiling mechanism in the pool boiling system, hence significantly enhanced heat transfer performance can be achieved.

Theoretical Analysis: The model could not predict HTCs for 10° taper angle due to limited pressure recovery effect that was unable to provide a sustained two-phase flow as discussed earlier in Chapter 4. For 15° taper angle, the HTC values were predicted and validated by comparing with the experimental findings. The deviation between theoretical and experimental HTC values decreases with increasing heat flux and minimum deviation value was 11% near CHF. The fluid flow in tapered microgap is driven by heat flux hence the accuracy of theoretical model improves at higher heat fluxes.

Chapter 6

6.0 Pool Boiling Performance of Dual Tapered Manifold with HFE7000

In this study, a dual tapered manifold block was used on a plain copper surface with HFE7000 as the working fluid in a pool boiling system. An experimental study was conducted with five different taper angles (5°, 10°, 15°, 20°, 25°) and two inlet gap heights (0.8mm, 1.27mm). The heat transfer enhancement was evaluated for different configurations. The experimental setup, experimental procedure, data reduction, heat transfer results, and conclusion of the study are discussed in this chapter.

6.1 Experimental Setup

The closed loop experimental setup for dielectric liquid with the boiling test section used in this study is shown in Fig. 40. The setup consists of a fluid chamber with a boiling test section test section, a condenser coil, and a heater block assembly underneath the test section. The fluid chamber was built using a mild steel cylinder with a visualization window. The boiling test section at the bottom wall of the chamber contains a plain copper test chip, garolite chip holder, steel spacer, and a dual tapered manifold block. The garolite chip holder was designed and fabricated to minimize the heat losses from the stem of the copper test chip. The dual tapered manifold block was secured over the test chip, and the steel spacer was placed between the manifold block and the test chip to develop the desired inlet gap height. The boiling surface (10 mm × 10 mm) was exposed to the working fluid by covering the edges of the test chip with kapton tape. The working liquid was maintained at saturation using a cartridge heater which was fixed adjacent to the test section, completely immersed in the liquid. The saturation state of the liquid was recorded using a

K-type thermocouple. A condensing copper coil was attached to the top wall of the chamber to condense HFE7000 vapor back to liquid phase. The copper coil was connected to an external water chiller outside the boiling chamber. A pressure gauge, vacuum port, and a liquid charging port were also attached outside the mild steel chamber.

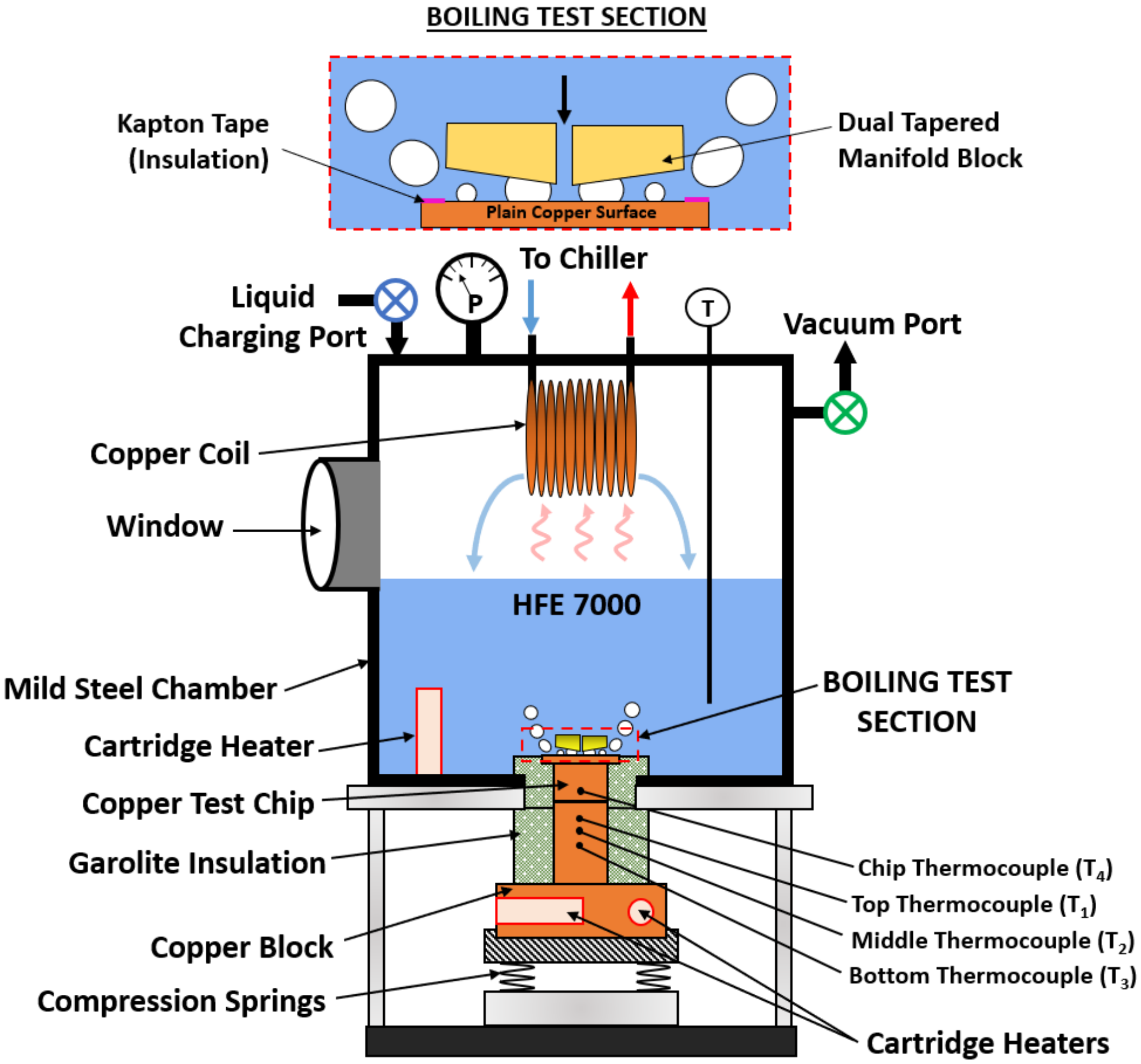

Figure 40: Schematic showing the experimental setup and boiling test section used for pool boiling study with dual tapered manifold bock and HFE7000.

A heater block assembly was placed underneath the test section to supply heat to the copper chip in the test section. The assembly consists of a copper heater block, a garolite insulation sleeve, four cartridge heaters (200W each), and four compressed springs on a fixed platform. The cartridge heaters were connected to an external dc power supply and were used to heat the copper block. The compressed springs were used to push the heater block assembly against the fixed boiling chamber. This developed an effective contact between the copper heater block and the test chip. To further reduce the contact resistance, a grafoil sheet was used between the heater block and the test chip. Three K-type thermocouples were inserted in the copper heater block, and the recorded temperatures were used to calculate the performance parameters.

6.2 Experimental Procedure

The procedure followed while conducting experiments for all the tapered configurations is discussed in this section.

- **Step 1:** The experimental test setup was assembled on a benchtop and the working liquid (HFE7000) was charged in the system through the liquid charging port.
- **Step 2:** A vacuum pump was attached to the vacuum port in the steel chamber, and 15 psi vacuum was created in the setup. Since the presence of air in the chamber reduces the efficiency of copper coil, vacuum was created to eliminate the existing air from the chamber.
- **Step 3:** The dc power supply was turned on and power was supplied to the cartridge heaters in the copper heater block. The cartridge heater in the steel chamber was

turned on to maintain the bulk working liquid at its saturation temperature of 34°C at 1 atm.

- **Step 4:** The external water chiller was turned on to maintain the system pressure at 1 atm. Onset of nucleate boiling was confirmed through the visualization window attached in the test chamber.
- **Step 5:** The voltage in the supper supply was increased in the steps of 2V to 5V, and temperature readings from all thermocouples were recorded at steady state through a LabVIEW program. The steady state was confirmed when the temperature variation for all thermocouples (T_1-T_4) was less than 0.1°C over a period of 25 minutes.
- **Step 6:** The chiller water temperature and power supply to cartridge heater in the working liquid were adjusted to maintain liquid at saturation temperature and an absolute pressure of 1 atm.

The temperature data was recorded for different heat fluxes until CHF was achieved for each configuration.

6.3 Data Reduction

The data reduction methodology adopted for this study is similar to the data reduction performed in Chapter 5. The heat transfer parameters - heat flux (q''), boiling surface temperature (T_s), wall superheat (ΔT_{sat}), and HTC were calculated from the temperature recordings from the various thermocouples in the test setup. Similar data reduction approach was adopted in previous pool boiling studies [64–66]. The heat transfer equations, Eqs. (11 – 15) were used to calculate all the performance parameters. As shown in Fig.41, the values of Δx and x_1 parameters were 5 mm and 7.1 mm, respectively.

The uncertainty analysis was conducted for all heat transfer parameters and the detailed discussion on uncertainty calculation is presented in Appendix. The uncertainty values for heat flux and HTC are shown as error bars in the section 6.4 - experimental results.

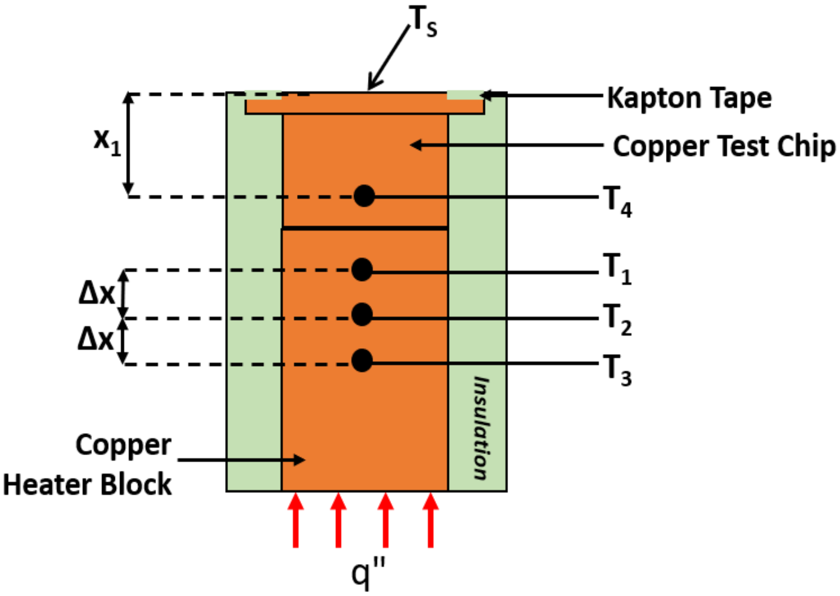

Figure 41: Heat transfer in 1D along the copper heater block and copper test chip.

Validation of one-dimensional heat conduction: The heat transfer parameters were calculated assuming one-dimensional heat conduction through the stem of the copper heater block. Therefore, a linear temperature gradient is expected through the thermocouples, T_1 to T_3. The temperature variation along the stem of the heater at three thermocouple locations for 25° taper angle with 0.8mm inlet gap height is shown in Fig. 42. The linear equations at different heat fluxes are shown, and the linear regressions (R^2) for the heat fluxes tends to 1. This proves the authenticity of the linear temperature profile and the one-dimensional heat conduction. This assumption was validated for all the experimental configurations by plotting the temperature variation at equidistant thermocouple locations along the heater stem.

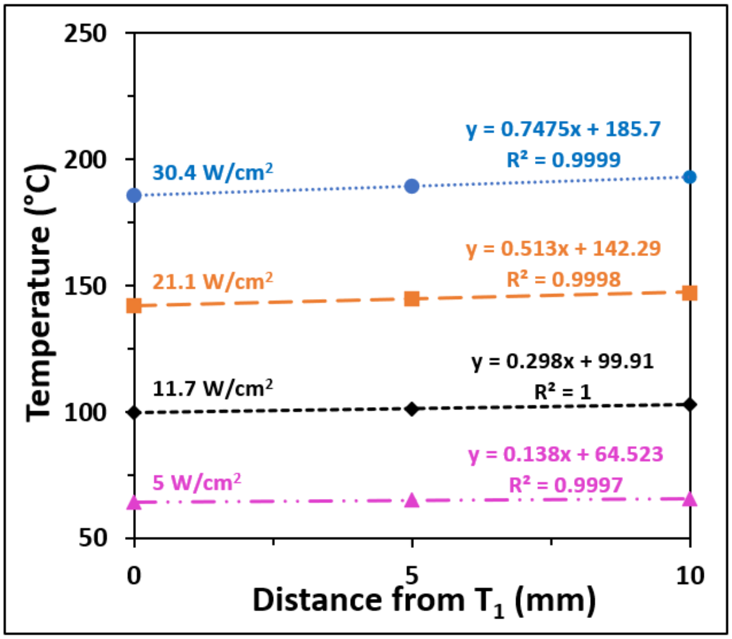

Figure 42: The temperature variation at different heat fluxes along the copper heater block for 25° dual taper angle and 0.8 mm inlet gap height.

6.4 Experimental Results for Enhancement on Plain Surface

The pool boiling results using dual taper tapered microgap with HFE7000 as the working fluid are presented in this section. Five different taper angles – 5°, 10°, 15°, 20°, and 25° were studied with two inlet gap heights – 0.8 mm, and 1.27 mm.

6.4.1 Effect of Taper Angle on Heat Transfer Parameters

Heat transfer results for 0.8 mm inlet gap and dual taper angles (5° - 25°)

The heat dissipation performance of dual tapered microgap is compared with the ‘no manifold block’ baseline configuration where no manifold block was used on the plain copper test chip. The pool boiling curves for different configurations are shown in Fig.43(a), and Fig.43(b) shows the variation in HTC with increasing heat flux.

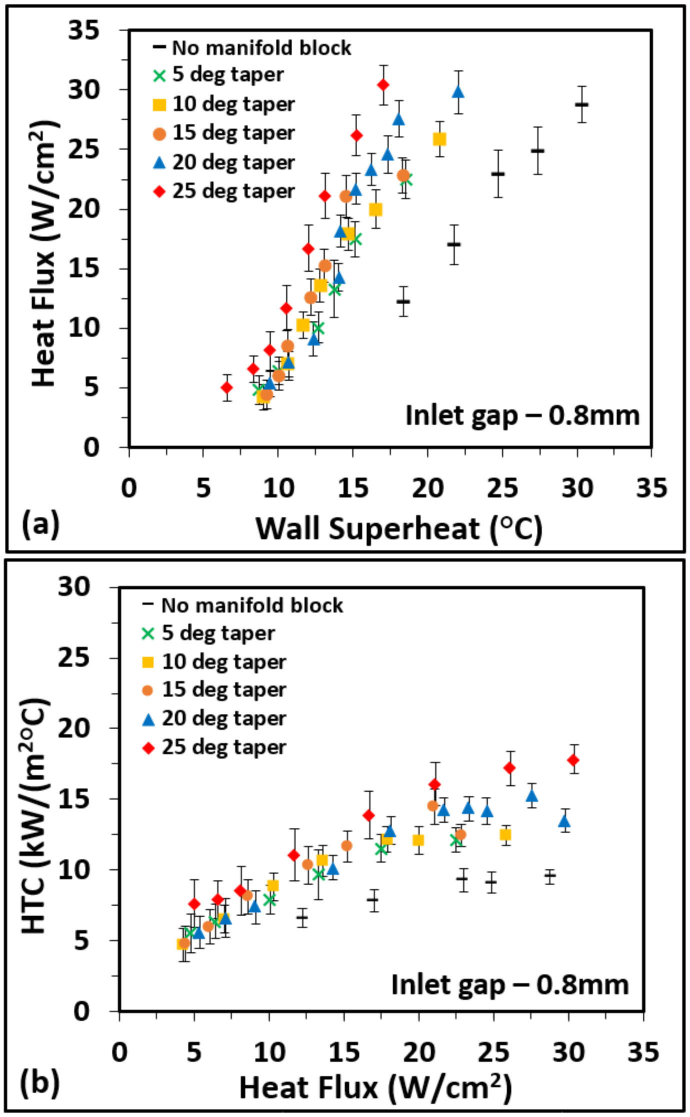

Figure 43: Pool boiling results for 0.8 mm inlet gap height and different dual taper angles (5°-25°), (a) Variation in heat flux with respect to wall superheat, (b) Variation in heat transfer coefficient (HTC) with respect to heat flux.

The maximum CHF and HTC were obtained for 25° dual taper angle. The highest CHF and HTC values achieved were 30.4 W/cm^2 and 17.8 kW/(m^2°C) respectively at a wall superheat of 17°C. The CHF and HTC values obtained for 'no manifold block' configuration were 28.8 W/cm^2 and 9.5 kW/m^2°C. Approximately, 2X enhancement was observed in the HTC using 25° taper angle; this proves high heat dissipating efficiency can be achieved using dual tapered microgap. For all the dual taper angles, higher HTCs were obtained compared to 'no manifold block' configuration. For 5°, 10°, and 15° taper angles, a reduction in CHF was observed, whereas for 20°, and 25° taper angles similar CHF was obtained compared to 'no manifold block' configuration. The CHF and maximum HTC values for all taper angles with 0.8 mm gap and 'no manifold block' configuration are shown in Table 3.

Table 3: Pool boiling results for 0.8 mm inlet gap and different dual taper angles with HFE7000.

Taper Angle	**HTC (kW/m^2°C)**	**ΔT_{sat} (°C)**	**CHF (W/cm^2)**
No manifold block	9.5	30.3	28.8
5°	12.1	18.5	22.5
10°	12.4	20.8	25.9
15°	12.4	18.3	22.8
20°	13.5	22	29.8
25°	17.8	17	30.4

Heat transfer results for 1.27 mm inlet gap and dual taper angles (5° - 25°)

Figure 44 shows the effect of different taper angles for 1.27 mm inlet gap height. The pool boiling performance of dual tapered manifold is compared with the 'no manifold block' configuration. The pool boiling curves for different configurations are shown in Fig.44(a), and the variation in HTC with increasing heat flux is shown in Fig.44(b).

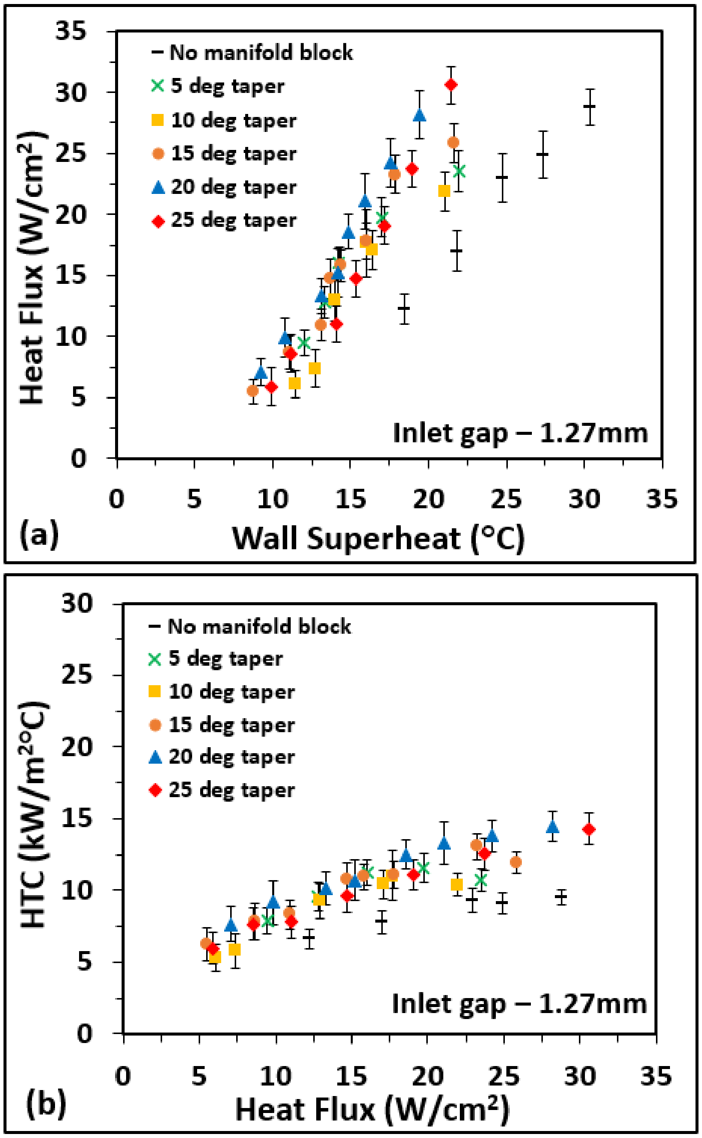

Figure 44: Pool boiling results for 1.27 mm inlet gap height and different dual taper angles (5°-25°), (a) Variation in heat flux with respect to wall superheat, (b) Variation in heat transfer coefficient (HTC) with respect to heat flux.

The best heat transfer performances were obtained for 25° and 20° dual taper angles. The CHF and HTC values obtained for 25° dual taper were 30.6 W/cm^2 and 14.3 kW/m^2°C respectively. These values were obtained at a wall superheat of 21.4°C. The CHF and HTC values achieved for 20° dual taper were 28.1 W/cm^2 and 14.5 kW/m^2°C, respectively at a wall superheat of 19.4°C. The 1.5X enhancement in HTC was obtained using 25°, and 20° dual taper angles compared to 'no manifold block' configuration. Similar to 0.8 mm inlet gap configuration, higher HTCs were obtained for all the taper angles compared to the 'no manifold block' configuration. For 5°, 10°, and 15° taper angles, a reduction in CHF was observed, whereas for 20° and 25° taper angles similar CHF was obtained compared to 'no manifold block' configuration. The CHF and maximum HTC values for all taper angles with 1.27 mm gap and 'no manifold block' configuration are shown in Table 4.

Table 4: Pool boiling results for 1.27 mm inlet gap and different dual taper angles with HFE7000.

Taper Angle	HTC (kW/m^2°C)	ΔT_{sat} (°C)	CHF (W/cm^2)
No manifold block	9.5	30.3	28.8
5°	10.7	21.9	23.5
10°	10.4	21.7	21.9
15°	11.9	21.6	25.8
20°	14.5	19.4	28.1
25°	14.3	21.4	30.6

6.4.2 Effect of Inlet Gap on Heat Transfer Parameters

The pool boiling curves for different taper angles and inlet gap heights is shown in Fig.45. The aim of this representation is to evaluate the effect of inlet gap height for different dual taper angles. For 5°, 10°, 15°, and 20° dual taper angles, no significant effect was observed on the heat transfer performance. Whereas an enhanced heat transfer performance was observed for 0.8 mm inlet gap compared to 1.27 mm gap with 25° dual taper angle. The HTC, CHF, and wall superheat values for all the configurations are shown previously in Table 3 and Table 4.

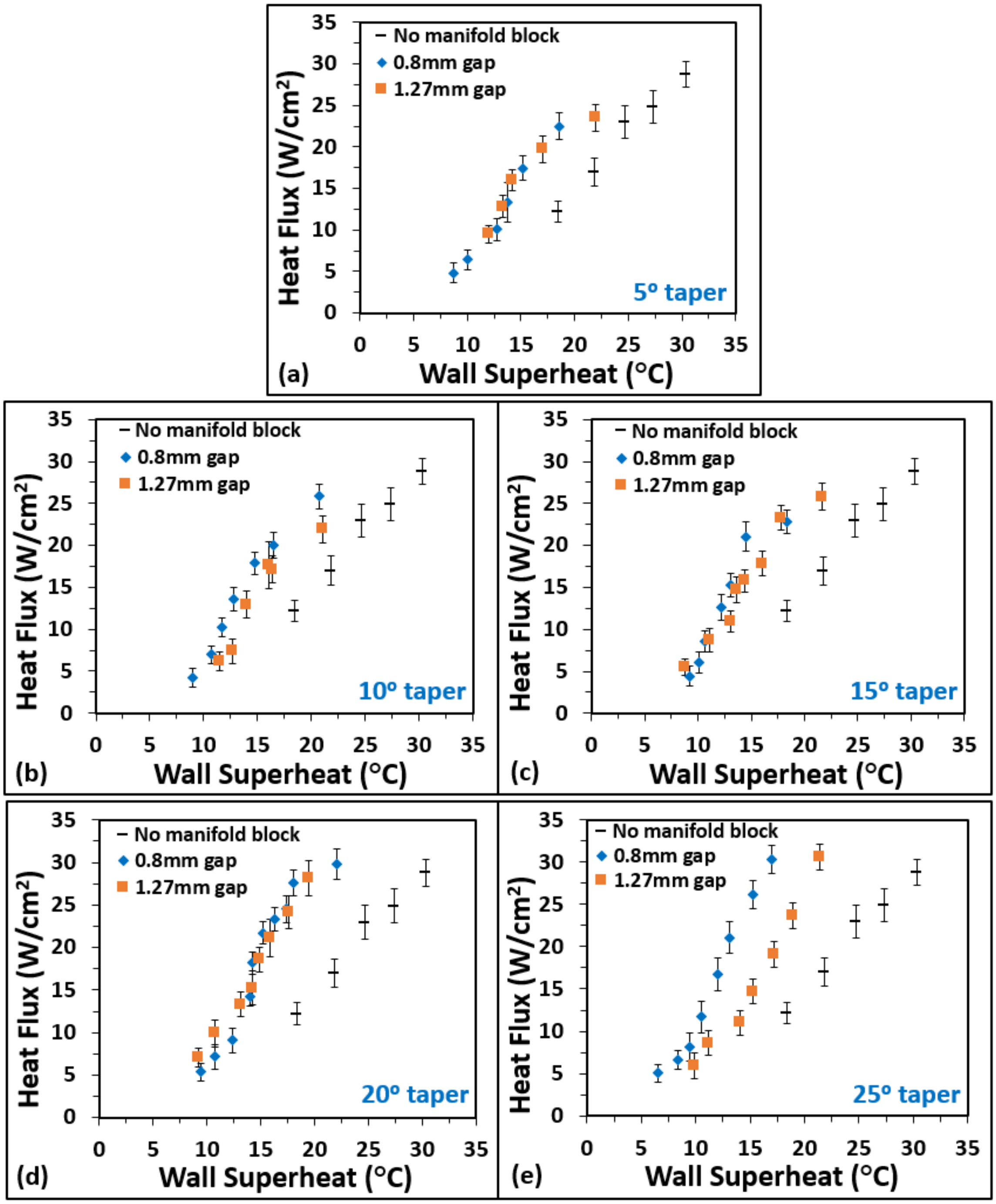

Figure 45: Pool boiling curves for 5°, 10°, 15°, 20°, and 25° taper angles comparing the effect of 0.8 mm and 1.27 mm inlet gap heights.

6.4.3 Discussion on Observed Heat Transfer Performance

The bubble squeezing and pressure recovery effects are responsible for creating a stable fluid flow along the flow length in the tapered microgap region. The bubble squeezing mechanism is discussed in detail in Chapter 8 and the schematic showing the bubble squeezing process was shown earlier in Fig.23 in Chapter 3. As the squeezed bubble leaves the tapered microgap region and it creates liquid pumping effect from the bulk into the microgap. The pressure recovery effect due to expanding cross-section helps in reducing the total pressure drop thus improving the flow stability with low pumping power requirement. A detailed discussion on the pressure recovery and total pressure drop was discussed in Chapter 4. For the dielectric liquid (HFE7000) in this study, enhanced HTCs were obtained but no improvement in CHF was achieved. At higher heat fluxes, large vapor films are developed near the heater surface due to high bubble nucleation frequency and bubble coalescence causing poor heat transfer. An effective removal of vapor lumps and liquid resupply is essential to obtain high CHF and HTC values. Further study is recommended to improve the CHF values with smaller inlet gap heights less than 0.8 mm.

6.5 Theoretical HTC Results and Experimental Validation

The HTC values were predicted for 15°, 20°, 25° taper angles with 0.8 mm inlet gap, and 20°, 25° taper angles with 1.27 mm inlet using the boiling correlation by Kandlikar [61] as discussed earlier in Chapter 4. The model was validated by comparing the predicted HTC values with the experimental results. The comparison between predicted and experimental values is shown in Fig. 46. The accuracy of the theoretical predictions increases with heat increase in heat flux, and maximum accuracy is obtained near CHF since fluid is driven by heat flux in the tapered configurations. To improve the accuracy of the theoretical values, the effect of bubble squeezing mechanism can be included in the future developments. A preliminary force balance on the bubble during expansion is presented later in Chapter 8. The force balance can be adopted to develop a dynamic bubble squeezing model to evaluate the pumping action provided by the interface motion. The additional pumping action due to bubble squeezing will increase the predicted mass flux values, hence improved

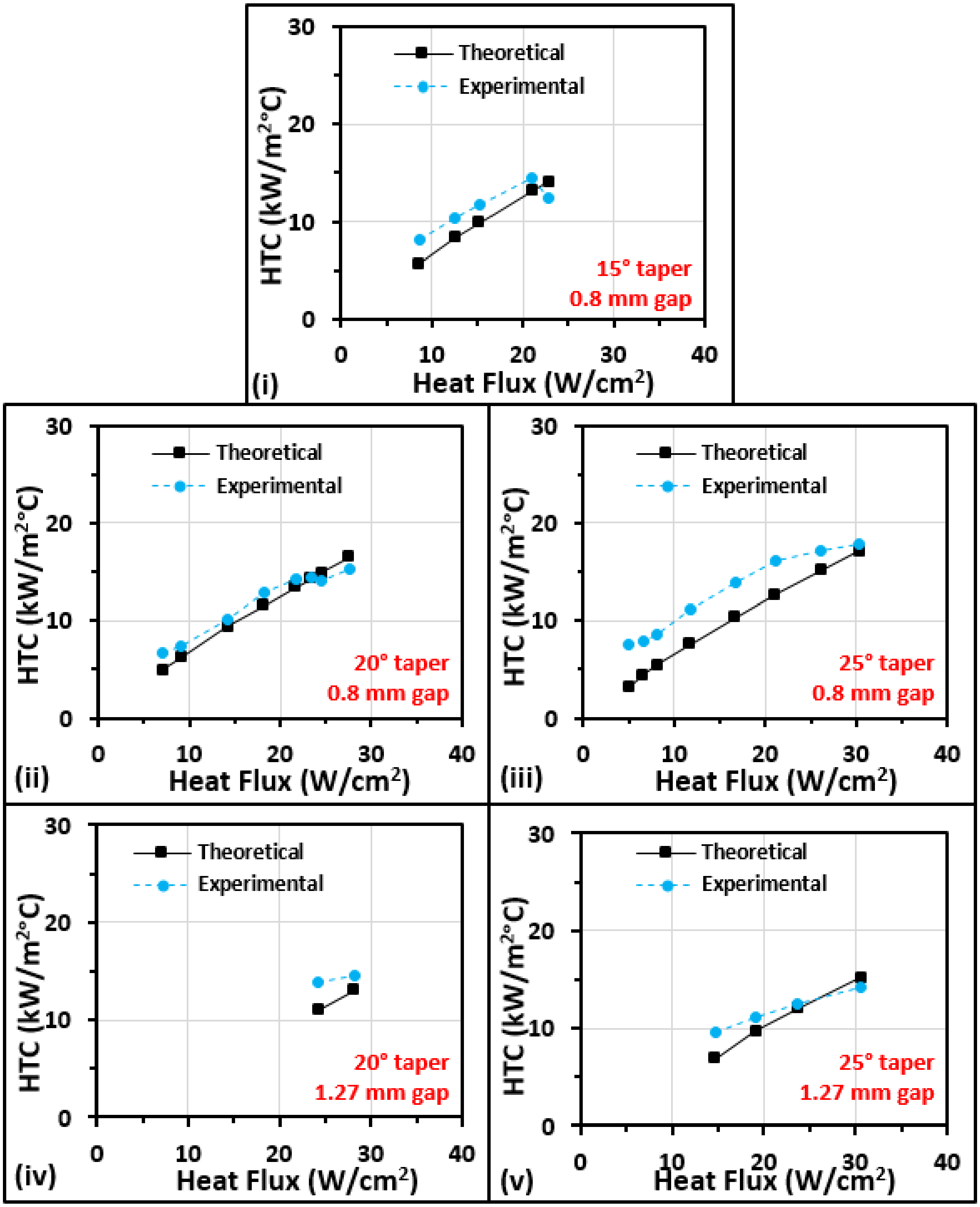

Figure 46: The predicted HTC values and the comparison with the experimental results for different geometric configurations.

theoretical predictions can be made at low heat fluxes. Table 7 shows the comparison between predicted and experimental HTC values at CHF for different geometric configurations.

Table 5: Comparison between the theoretical and experimental HTC values at CHF for different geometric configurations for 1.27 mm inlet gap with HFE7000.

Inlet gap (mm)	Taper angle (°)	Experimental HTC at CHF (kW/m^2°C)	Theoretical HTC at CHF (kW/m^2°C)	Deviation % $\left\lvert\frac{HTC_{exp} - HTC_{theory}}{HTC_{exp}}\right\rvert \times 100$
0.8	15	12.4	14.1	13.3
0.8	20	15.3	16.5	7.9
0.8	25	17.8	17.2	3.8
1.27	20	14.5	13.1	9.7
1.27	25	14.3	15.2	6.3

6.6 Major Outcomes from Experimental Study and Theoretical Analysis

Experimental Study: Dual tapered manifold design is seen to significantly influence the heat transfer parameters. The dual tapered design was tested for five taper angles - 5°, 10°, 15°, 20°, and 25° with two inlet gap heights – 0.8 mm, and 1.27 mm. Reduction in CHF was observed for 5°, 10°, and 15° taper angles with 0.8 mm, and 1.27 mm inlet gaps due lower pressure recovery effects in smaller taper angles. Higher HTCs were achieved for all taper angles compared to ‘no manifold block’ configuration thus suggesting enhancement in heat dissipation efficiency. The HTCs obtained for 20°, and 25° taper angle with 0.8 mm inlet gap heights were 13.5 kW/m^2°C, and 17.8 kW/m^2°C at a CHF of 30 W/cm^2. For 1.27 mm inlet gap, the HTC achieved for 20°, and 25° taper angles was 14.5 kW/m^2°C at CHFs of 28.1 W/cm^2 and 30.6 W/cm^2, respectively. A 2X and 1.5X enhancement in HTC was recorded using 25° taper angle with 0.8 mm, and 1.27 mm inlet gaps respectively compared to ‘no manifold block’ configuration.

Theoretical Analysis: The model could not predict HTCs for 5°, 10° taper angles with 0.8 mm inlet gap height and 5°, 10°, 15° taper angles with 1.27 mm inlet gap height. For these configurations pressure drop is greater than pressure recovery effect for all heat fluxes. For cases where pressure recovery was able to balance the pressure drops with stable flow, the HTC values were predicted and validated by comparing with experimental findings. The maximum deviation in the theoretical and experimental HTC value was 13.3% for 15° taper with 0.8 mm inlet gap. For all other configurations less than 10% deviation was obtained, thus validating the use of homogeneous model in the theoretical approach.

Chapter 7

7.0 Thermosiphon Loop with Dual Tapered Manifold for CPU Cooling

In this study, an innovative evaporator design in a thermosiphon loop is introduced for CPU cooling application in servers assembled horizontally in a rack in data center. The manifold block containing a dual taper design is used in the evaporator to develop a stable two-phase fluid circulation in a thermosiphon loop. The thermal performance of the thermosiphon loop was compared with the currently used air based, and water-based coolers.

The three taper angles studied in this work are 2°, 2.5°, and 3°. Based on the previous flow boiling work on tapered manifold by Kalani and Kandlikar [34,41], it was observed that taper design reduces the flow instabilities and decreases the total pressure drop along the flow length. Based on these observations, the taper angle of 2° was selected as the lower limit in the current study. However, Kalani and Kandlikar showed 3.4° taper angle produced best heat dissipation performance over a flow length of 10 mm. Since the flow length in the presented study is larger, two additional angles of 2.5° and 3° were also studied. The flow length in the presented work is based on the dimensions of the targeted CPU.

7.1 Methodology

The experimental study was conducted in three phases – a) benchtop thermosiphon loop on a mock CPU heater, b) thermosiphon loop on an actual CPU under thermal stressful conditions, and c) comparison of thermosiphon loop, air cooler, and water cooler under high heat flux conditions.

a) **Benchtop thermosiphon loop on a mock CPU heater:** In this phase of the study, a standalone version of thermosiphon loop was designed and built to evaluate the heat dissipation ability of the loop for different taper angles. The study was performed on a copper heater (mock CPU) with dimensions same as the dimensions of the CPU's heat spreader. The targeted CPU is a i7-930 processor with a thermal design power (TDP) 130 W and heat spreader measurements, 34.5 mm x 32 mm.

b) **Thermosiphon loop on an actual CPU under thermal stressful conditions:** In this phase of the study, the performance and adaptability of the thermosiphon loop for actual CPU cooling was evaluated under thermal stressful conditions. The evaporator of the thermosiphon loop developed in the benchtop study was mounted on an i7-930 processor, and the cooling performance was compared with the commercial air based, and water based coolers.

c) **Comparison of thermosiphon loop, air cooler, and water cooler under high heat flux conditions:** In this phase of the study, the cooling performance of the three coolers was evaluated on the mock CPU heater under high heat flux conditions. The actual CPU cooling study provides performance comparison at low heat flux based on the TDP of CPU, therefore this study was performed to compare the performance of the three coolers at high heat flux conditions.

7.2 Benchtop Thermosiphon Loop on a Mock CPU Heater

7.2.1 Experimental Setup of the Standalone Loop

A benchtop thermosiphon loop was designed and fabricated for experimental study under the heat flux-controlled environment. The data obtained from this configuration was used to evaluate the ability of a dual-tapered evaporator for CPU cooling in a thermosiphon loop. The benchtop loop contains an evaporator, a condenser, two risers, and a downcomer as

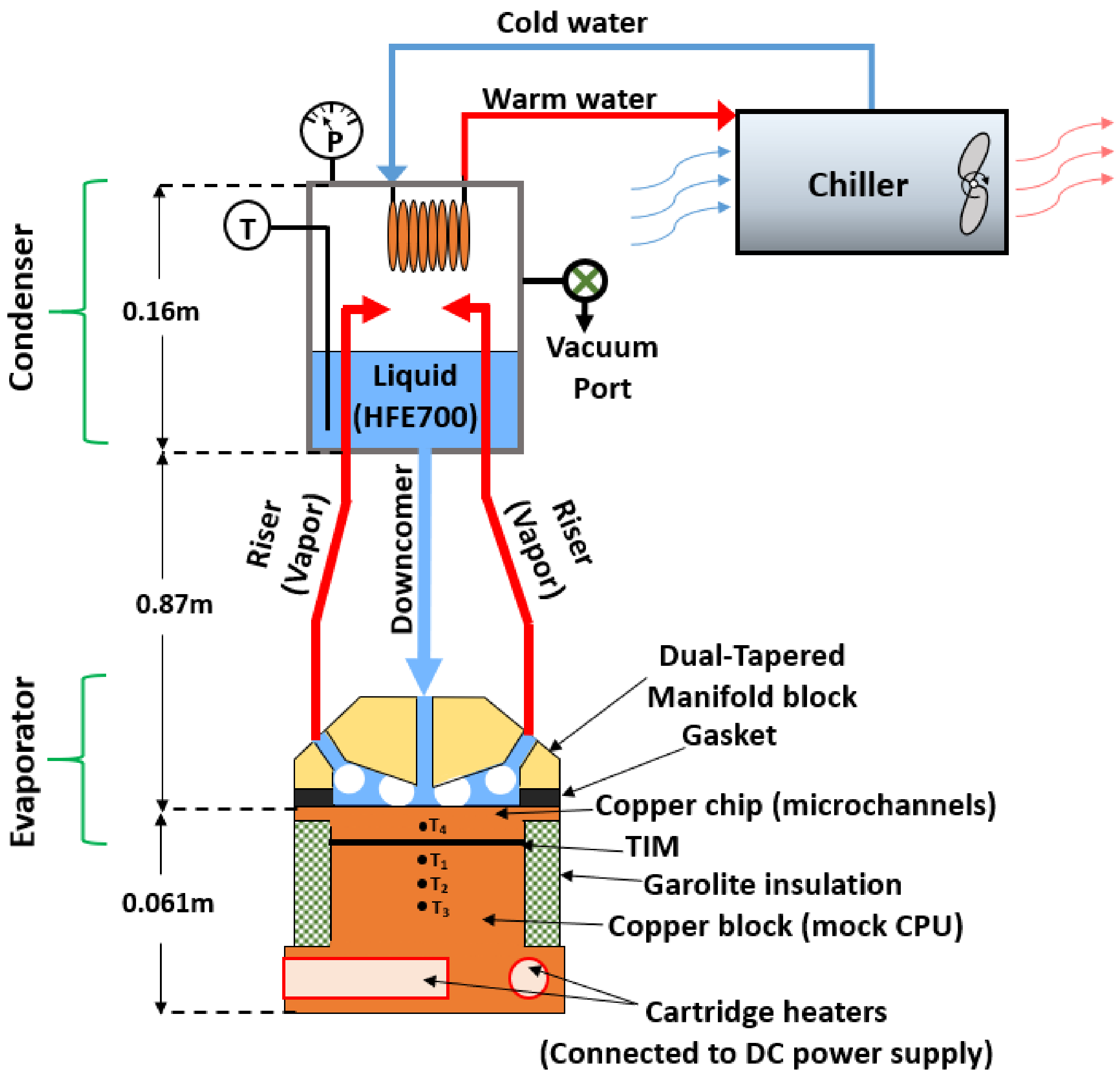

Figure 47: The schematic of benchtop thermosiphon loop with dual-tapered manifold in the evaporator and mock CPU.

shown in Fig.47. The dielectric fluid, HFE7000 was used as the working fluid considering the electronics cooling application. In a server, the CPU temperature is low during less loading conditions, but during stressful conditions under high load, the CPU reaches its maximum processing ability, and the CPU temperature increases significantly. The saturation temperature of HFE7000 is 34°C at 1 atm, hence this fluid allows boiling heat transfer over a wide range of operating CPU temperature.

<u>Condenser:</u> The condenser unit was built using a stainless-steel cylinder, and a copper coil was installed at the top surface inside the cylinder. The copper coil is connected to a water-cooled loop using an external chiller. The condenser acts as a reservoir for the working fluid and a downcomer was attached to the bottom surface of the condenser which supplies working liquid to the evaporator. Two risers were attached on either side of the downcomer such that outlet of the risers is above the liquid interface. To record the temperature of the working fluid, a K-type thermocouple was immersed in the bulk liquid. A pressure gauge was also attached to the condenser to ensure atmospheric pressure is maintained inside the condenser. The presence of air in the condenser reduces the efficiency of the copper coil therefore a vacuum port was also attached to the condenser which was connected to a vacuum pump to remove air from the condenser before conducting the experiments.

The head between the evaporator and the condenser was 0.87m. This was decided based on the compatibility of thermosiphon loop with server racks at RIT’s data center. The head may change depending upon the rack dimensions and the available overhead space in the server room And the condenser may supply working fluid to multiple evaporators down the rack during actual application.

__Evaporator:__ The evaporator section contains a dual-tapered manifold block, mounting bracket, gasket, mounting ring, and a copper chip. The exploded CAD model of the evaporator is shown in Fig.48.

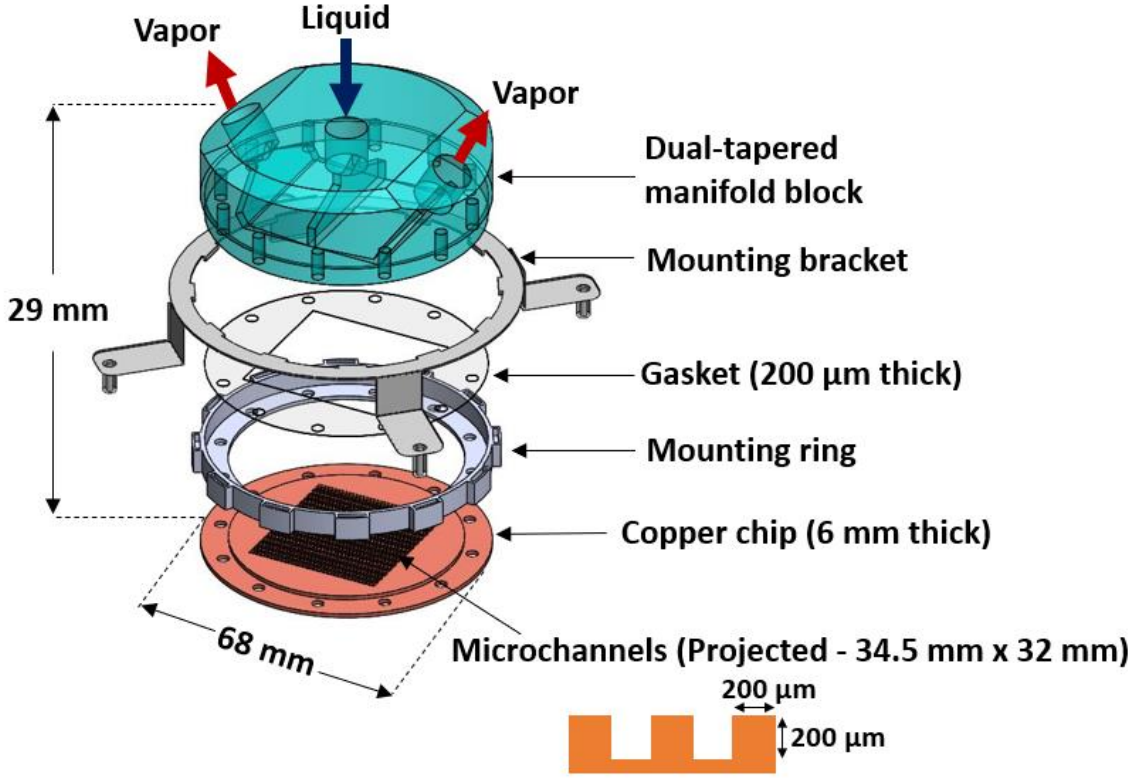

Figure 48: The 3D CAD exploded model of the evaporator assembly.

The dual-tapered manifold was machined from polycarbonate (Lexan) material which has a glass transition temperature of 135°C. The manifold block contains a central liquid inlet, two symmetric tapered sections, and two vapor outlets. The copper chip with microchannels is placed under the manifold block with a 200 µm thick silicon gasket between the copper chip and manifold block. The gasket thickness defines the inlet gap of the tapered microgap region. The copper chip contains microchannels with channel depth, channel height, and fin width as 200µm. These channel dimensions were based on the flow boiling work by Kalani and Kandlikar [34,41]. The copper contains a 34.5mm×32mm×4mm step at the bottom. This step was designed in order to place the chip directly in contact with the mock CPU heater and allow enough space to put a thermocouple to measure the chip temperature. The assembly of manifold block, copper chip, and gasket are held together using an aluminum ring and 12 hex screws. The whole evaporator assembly is mounted on the mock CPU heater using a mounting bracket and thermal interface material (TIM) was applied on the heater. As shown in Fig.47, the mock CPU heater was fabricated using a copper block and was heated via joule heating using four cartridge heaters (200 W each). The cartridge heaters were connected to an external DC power supply. The heat transfer projected area was 34.5mm×32mm, these dimensions were decided based on the CPU dimensions (i7-930). Three K-type thermocouples were inserted in the copper heater block to calculate the heat flux for different configurations. The stem of the heater block was surrounded by a garolite insulation to minimize the heat losses.

7.2.2 Experimental Procedure

The procedure followed while conducting experiments for all the tapered configurations is discussed in this section.

- **Step 1:** Refrigerant HFE7000 (175ml volume) was charged in the condenser and the fill volume 175ml was selected based on previous study on optimum fill volume in thermosiphon loop [67].
- **Step 2:** The vacuum pump was turned on and air was removed through the vacuum port from the system before all experiments.

- **Step 3:** The thermocouples in the test setup were connected to the cDAQ device. And the setup was monitored by a Labview VI program and the National Instruments cDAQ – 9174 and MOD – 9211.

- **Step 4:** The external dc power supply was turned on and power was supplied to the four cartridge heaters in the mock CPU heater.

- **Step 5:** The boiling heat transfer was visually confirmed throughout the experiment and voltage was increased in steps of 5V for each heat flux data point.

- **Step 6:** Data was recorded at steady state conditions after about fifteen minutes of steady operation as indicated by the LabVIEW program. Steady state was confirmed when the temperature variation was less than 0.1ºC for all the thermocouples.

- **Step 7:** Pressure in the system was maintained at 1atm by controlling the cooling water temperature in the copper coil in condenser.

7.2.3 Data Reduction

The data reduction procedure adopted for this study was similar to the ‘pool boiling performance of dual tapered manifold with water’ as discussed earlier in Chapter 5. The heat transfer parameters - heat flux (q''), heat transfer coefficient (HTC) and, wall superheat (ΔT_{sat}) were calculated using the Eqs. (11 – 15). For this study, the value of Δx and x_1 parameters as shown in Fig.49 were 5 mm and 4 mm, respectively. The uncertainty analysis was conducted for all heat transfer parameters and a detailed discussion on uncertainty calculation is presented in Appendix. The uncertainty values for heat flux and HTC are shown as error bars in the ‘experimental results’ section 7.2.4.

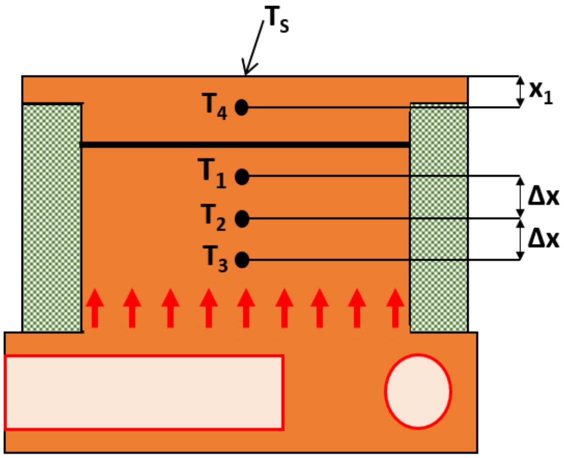

Figure 49: Heat flow in copper block in benchtop thermosiphon loop.

7.2.4 Heat Transfer Results

The heat dissipation performance of the benchtop thermosiphon loop was evaluated by mapping the boiling curve and heat transfer coefficient for three dual taper angles - 2°, 2.5°, and 3°. The highest heat flux values reported in this research indicate the maximum heat fluxes achieved during the experiments, these are not the critical heat flux (CHF) values. The maximum heat flux for all the configurations was limited by the heat transfer capacity of copper coil in the condenser.

7.2.4.1 Boiling Curve for Benchtop Thermosiphon Loop Testing

The boiling curves obtained for the benchtop thermosiphon loop testing for different dual taper angles are shown in Fig. 50. The degree of subcooling for all the experimental configurations was kept below 5°C. The degree of subcooling is defined as the difference between the saturation temperature and actual temperature of the working liquid at the condenser outlet in the downcomer. The boiling curve shows the variation in heat flux with respect to wall superheat for 2°, 2.5°, and 3° dual taper angles. The highest heat flux was achieved using 2° taper angle; 26 W/cm^2 at a wall superheat of 11.5°C. For 2.5° taper angle, the highest heat flux obtained was 25 W/cm^2 at a wall superheat of 15.5 °C. The taper angle of 3° provided the lowest performance compared to 2°, and 2.5° dual taper angles. The maximum heat flux achieved for 3° taper was 21 W/cm^2 at wall superheat of 14°C. The maximum heat flux values for different dual taper angles is shown in Fig. 51.

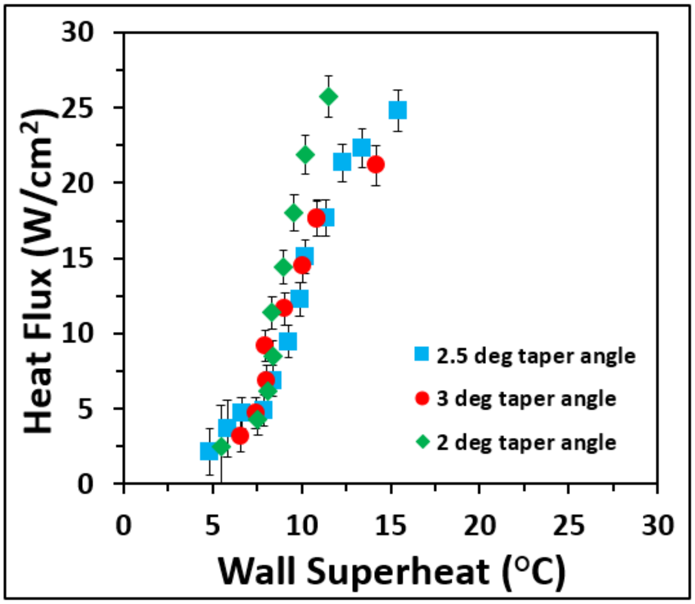

Figure 50: Boiling curve showing the variation in heat flux with respect to wall superheat for different dual taper angles in benchtop thermosiphon loop.

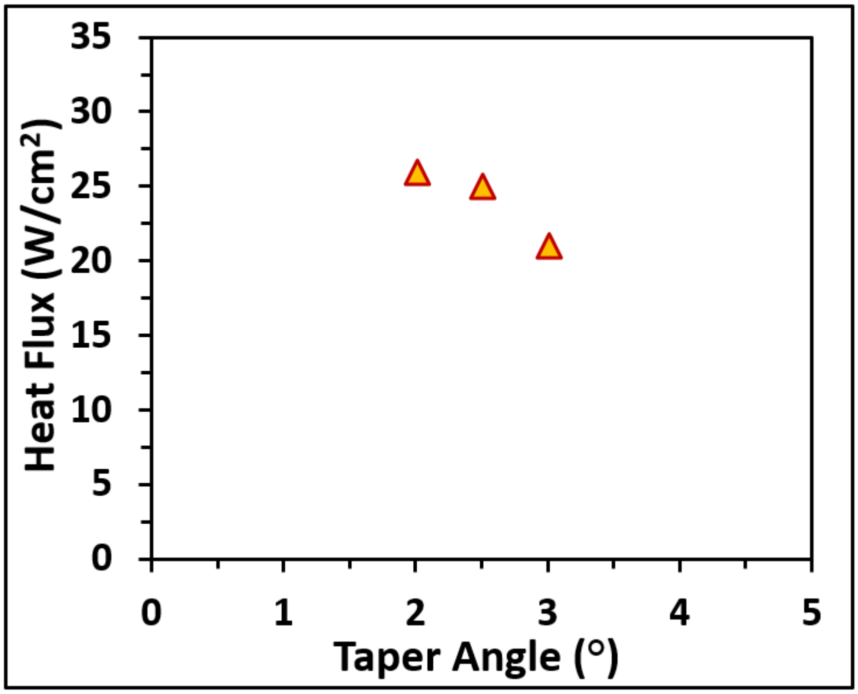

Figure 51:Maximum heat fluxes dissipated for different dual taper angles in benchtop thermosiphon loop.

7.2.4.2 Variation in Heat Transfer Coefficient (HTC)

The variation in heat transfer coefficient (HTC) with respect to dissipated heat flux for 2^o, 2.5^o, and 3^o dual taper angles is shown in Fig. 52. The efficiency of the heat transfer process in a system is defined by the HTC values. The highest HTC was achieved using 2° dual taper angle; 22.5 kW/m$^{2\circ}$C at a heat flux of 26 W/cm^2. For 2.5^o taper angle the maximum HTC obtained was 17.4 kW/m^{2o}C at a heat flux of 21 W/cm^2. The taper angle of 3° provided the lowest HTC value compared to 2°, and 2.5° dual taper angles. The maximum HTC achieved for 3° was 15 kW/m^{2o}C at the heat flux of 21 W/cm^2.

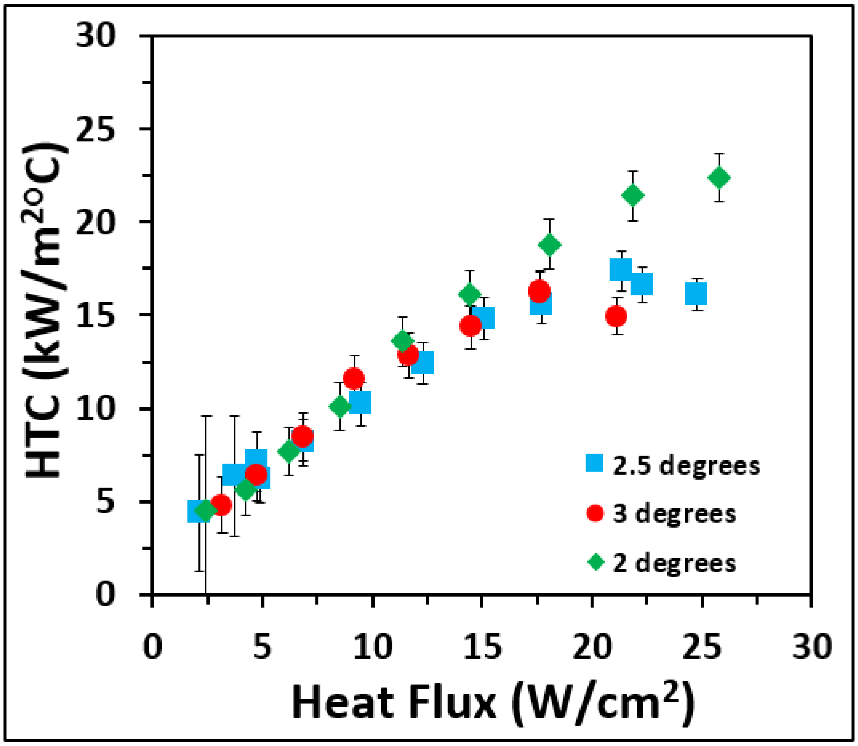

Figure 52: Variation in heat transfer coefficient (HTC) with respect to heat flux for different dual taper angles in benchtop thermosiphon loop.

The 2° dual taper angle dissipated more heat flux compared to 2.5°, and 3° and achieved higher HTC values. This suggests that 2° taper dissipates more heat with better efficiency. The tapered design allows pressure recovery which helps in developing a unidirectional flow thus enhancing heat transfer by continuously rewetting the heated surface. For higher taper angles - 2.5° and 3°, the liquid inertia reduces due to larger cross section along the flow length. This mitigates the bubble removal process in the flow domain. This results in high wall superheats and smaller HTC values. The heat flux dissipation ability of such tapered systems is proportional to the liquid inertia as shown by Kalani and Kandlikar [44].

7.2.5 Thermal Simulation of Mock CPU in ANSYS Static Thermal

The copper heater used in the benchtop configurations was developed based on the dimensions of i7-930 processor which is used in RIT's data center. The scale and the geometrical configuration of the evaporator used in thermosiphon loop study makes this configuration first of its kind. Since no other data is available for this setup, a numerical study was performed in ANSYS 18.1 to validate the experimental findings. A 3D heater model was designed in SolidWorks and was imported in the ANSYS design modeler as shown in Fig.53. An unstructured mesh consisting of 120,302 tetrahedral elements was generated as shown in Fig.54.

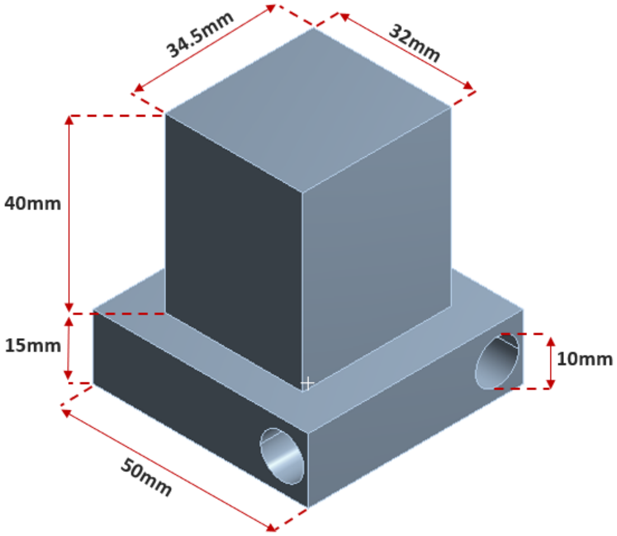

Figure 53: The 3D CAD model of mock CPU used in the benchtop thermosiphon loop study.

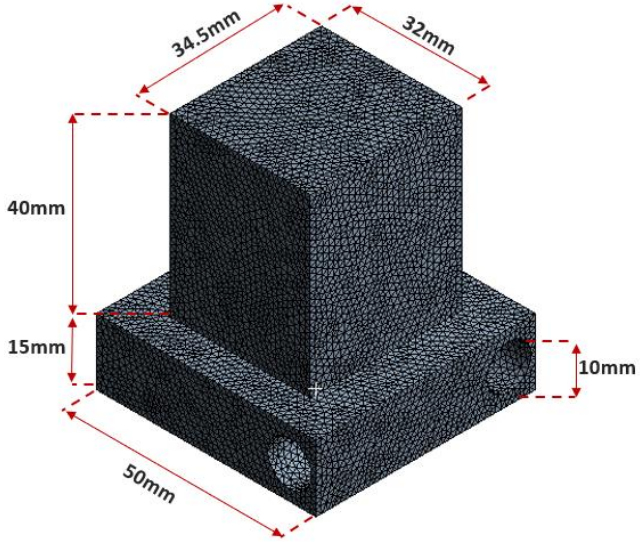

Figure 54: An unstructured mesh consisting of tetrahedral elements for simulation study in ANSYS static thermal.

Boiling heat transfer was simulated at the top surface of the heater block. According to the experimental findings the maximum and most-efficient heat dissipation was achieved for a 2° taper angle. Therefore, the experimental boundary conditions for 2° taper angle were used for the simulation. A total of 280 W of power was applied at the four holes where cartridge heaters were inserted during the experimental study. The heat transfer coefficient (HTC) of 22.38 kW/m^2°C achieved for 2° taper angle was applied at the top surface. The base and the sides of the copper heater were insulated using garolite which was exposed to air at the room temperature. HTC of 5 W/m^2°C was applied on the surfaces exposed to the air, this HTC value was calculated based on the thermal resistances due to garolite and the air pocket between heater wall and garolite sleeve.

The temperature distribution along the heater was obtained as shown in Fig. 55(a). A maximum temperature of 93°C was achieved near the holes where cartridge heaters were inserted. And minimum temperature of 56.3°C was achieved at the heater's top surface.

The temperatures at three thermocouple locations -T_1, T_2, and T_3 as shown in Fig. 55(b) were obtained as 59.5°C, 62.7°C, and 66°C, respectively.

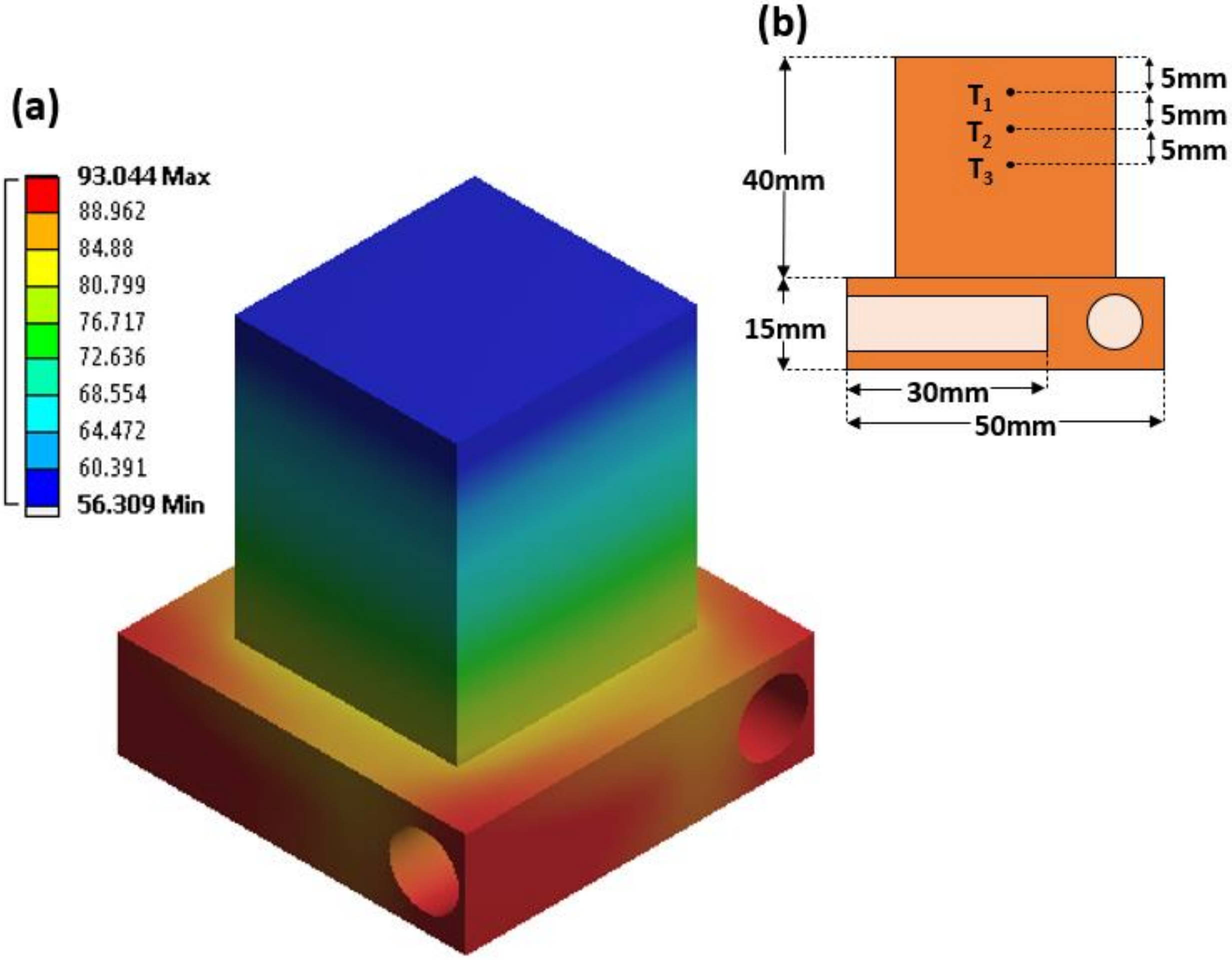

Figure 55: (a) The temperature contours obtained from the 3D simulation study of mock CPU heater, (b) A 2D schematic of mock CPU heater showing the thermocouple locations during experimental study.

The temperatures values at T_1, T_2, and T_3 from the experimental and numerical studies were compared as shown in Table 6. The difference between the measured and computed temperatures are comparable to the individual thermocouple uncertainty of 0.1 °C. This shows the validity of the data obtained during the experimental study of thermosiphon loop.

Table 6: The temperature comparison between experimental and numerical results at T_1, T_2, and T_3 during benchtop thermosiphon loop study.

Temperature location	Experimental (T_E) °C	Numerical (T_N) °C	$\lvert T_N - T_E \rvert$ °C
T_1	59.7	59.5	0.2
T_2	62.8	62.7	0.1
T_3	65.5	66	0.5

7.3 Thermosiphon Loop on an actual CPU under Thermal Stressful Conditions

7.3.1 Experimental Setup

The thermosiphon loop used for CPU cooling was same as the one used in benchtop testing, except for the mock CPU copper heater, the evaporator was mounted on a motherboard in direct contact with an actual CPU. The schematic of the whole assembly is shown in Fig. 56. The image of actual evaporator mounted directly on the CPU attached to the motherboard is shown in Fig. 57. The CPU used for the study was Intel i7-930 processor with a thermal design power (TDP) of 130W, which used in RIT's data center. To minimize the contact resistance, Arctic Silver thermal grease was used between the evaporator and the CPU. The heat dissipation performance of the thermosiphon loop was compared with SilenX air cooler (296g, 2.4W SilenX EFZ-80HA2), and Alienware water cooler (2.5W Alienware Area 51 W550R PP749). The detailed description of the air, water coolers is presented later in the Appendix.

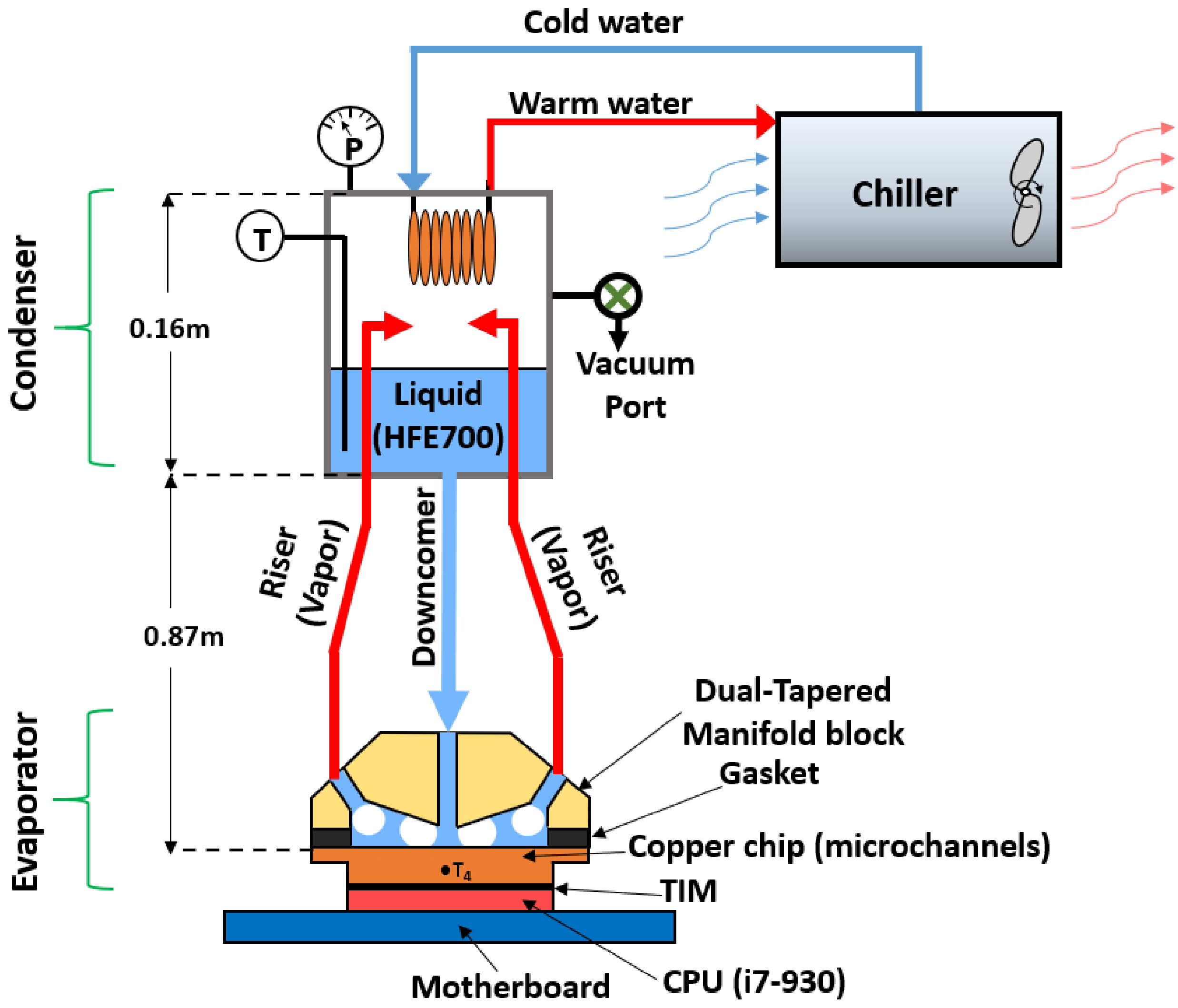

Figure 56: Schematic of experimental setup for actual CPU cooling using dual tapered evaporator in the thermosiphon loop.

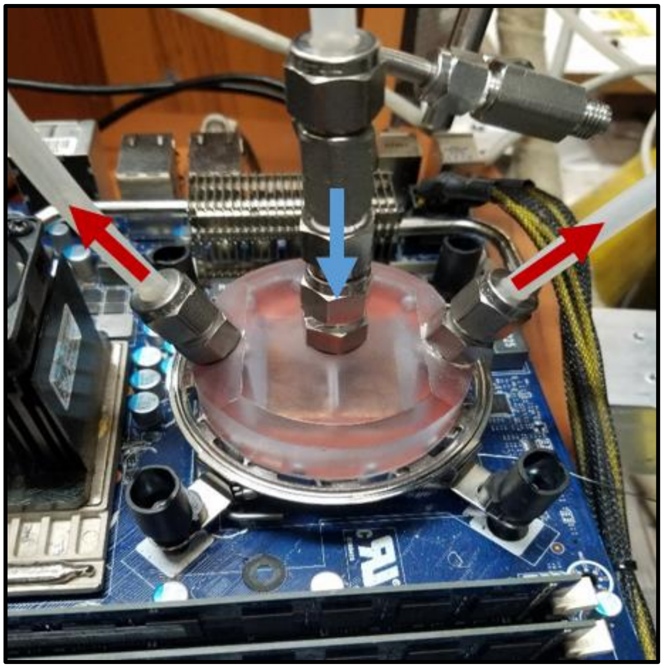

Figure 57: An actual image of evaporator containing dual tapered manifold mounted on the motherboard in direct contact with the CPU (i7-930 processor).

7.3.2 Experimental Procedure

The heat dissipation testing of three coolers – thermosiphon loop, air-based cooler, and water-based cooler was performed in two steps, 1) Baseline Test, and 2) Stress Test.

7.3.2.1 Baseline Test

The CPU was attached to an uninterruptible power source (UPS) which supplied continuous power for CPU operation. The UPS also displays the power consumed by the whole server. The server contains CPU, graphics processing unit (GPU) and cooling system as the main power consuming parts. Baseline testing was executed by turning ‘on’ the whole system and not putting any stress on the CPU. The power consumption was recorded for 3 hours for all the cooling setups tested, i.e. air cooler, water cooler, and thermosiphon loop.

7.3.2.2 Stress Test

In the data center CPU works under stressful conditions. Therefore, to evaluate the heat dissipation performance under stressful conditions, CPU was brought to its extreme performing capability by initiating a stress test. The stress test was performed by a Linux based stress package. The code simply calculates multiple roots continuously to bring CPU under stress thus increasing the temperature of all four cores. For all three coolers, the mean temperature of four cores was calculated and considered as the temperature of CPU (T_{CPU}) for the performance evaluation.

7.3.3 Data Reduction

A temperature difference parameter $\theta_{J\text{-}CW}$ was introduced in this study to compare the heat dissipation performance of air cooler, water cooler, and thermosiphon cooler.

7.3.3.1 $\theta_{J\text{-}CW}$ for Air Cooler and Water Cooler

The $\boldsymbol{\theta_{J\text{-}CW}}$ parameter for air, and the water cooler is defined as the temperature difference between the CPU and the chiller water. The two temperature drops identified between the CPU and the chiller water are between CPU- air and, air-chiller. The temperature drop between air and the chiller considered in the calculation is 18°C based on the study by Thangavelu et al. [68] on chiller study for commercial buildings. The temperature difference between CPU and air is determined from the experimental findings in this study. The thermal resistance diagram (Fig. 58) shows the heat flow path and temperature drops across the above mentioned steps.

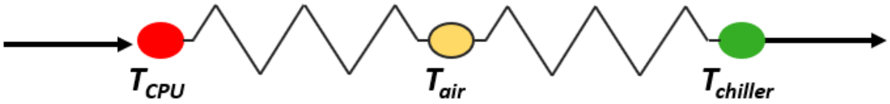

$$(T_{CPU} - T_{air}) + (T_{air} - T_{chiller}) = \theta_{J\text{-}CW}$$

Figure 58: Schematic of temperature drops between CPU - air, and air - chiller for air based, and water based coolers.

7.3.3.2 $\theta_{J\text{-}CW}$ for Thermosiphon Loop

The $\theta_{J\text{-}CW}$ parameter for the thermosiphon cooler is also defined as the temperature difference between CPU and the chiller water. The two temperature drops identified between CPU and the chiller are between CPU – saturated refrigerant and, saturated refrigerant - chiller. The temperature drop between the saturated refrigerant (T_{sat}) and the chiller considered in the calculations is 8°C based on the study by Matkovic et al. [69] on refrigerant condensation. The temperature difference between the CPU and the saturated refrigerant is determined from the experimental findings in this study. The thermal resistance diagram for thermosiphon loop (Fig. 59) shows the heat flow path and temperature drops across the above mentioned steps.

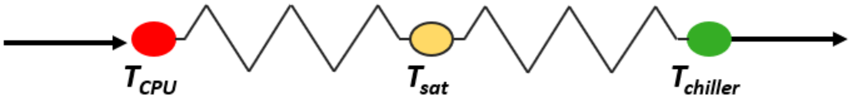

$$(T_{CPU} - T_{sat}) + (T_{sat} - T_{chiller}) = \theta_{J\text{-}CW}$$

Figure 59: Schematic of temperature drops at the CPU-refrigerant, and refrigerant-chiller interfaces for thermosiphon loop.

7.3.2 Heat Transfer Results - Comparison Study of Water Cooler, Air Cooler, and Thermosiphon Loop

To evaluate the heat dissipation performance of the thermosiphon loop, CPU cooling results of thermosiphon loop with dual taper tapered manifold were compared with commercial air and water-based coolers. Three dual taper angles - 2º, 2.5º, and 3º were tested in the thermosiphon loop configuration. The heat dissipation performance of all the coolers in terms of $\theta_{J\text{-}CW}$ is shown in Fig. 60. The CPU was under no stress initially during baseline phase, as the stress command was executed the temperature of four cores shoots up instantly. The CPU was dissipating ~ 12 W/cm^2 during the stress test. As shown in the performance plot, thermosiphon loop with 2º dual taper angle achieved minimum $\theta_{J\text{-}CW}$ during stressful conditions. This shows that this configuration dissipates heat from the CPU most efficiently compared to other configurations. The worst performance was observed for air-based cooler obtaining the highest $\theta_{J\text{-}CW}$ value. All dual taper angles in thermosiphon loop achieved better performance than air, and water coolers. The average $\theta_{J\text{-}CW}$ values for all the coolers during stress test is shown in Table 7.

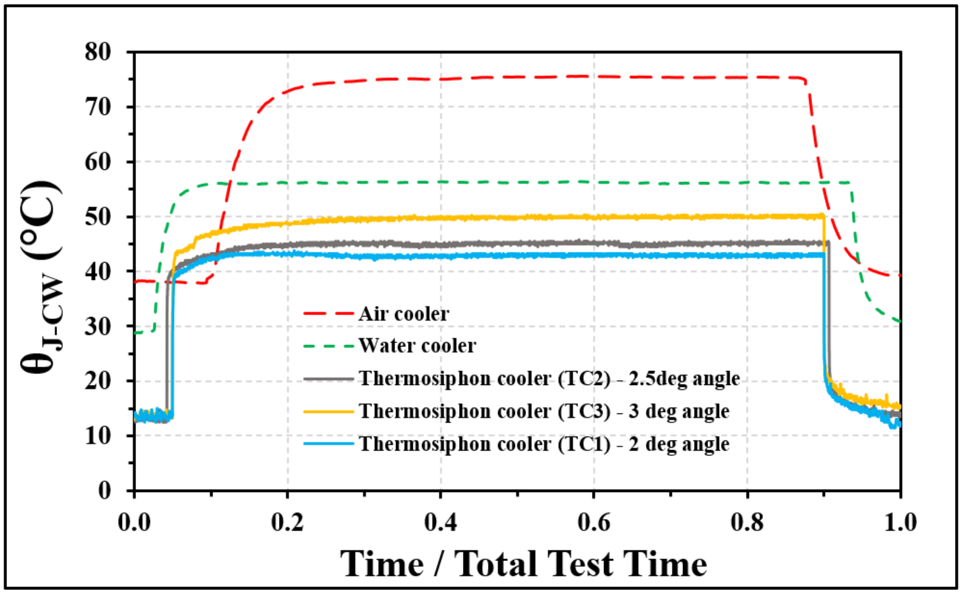

Figure 60: Plot showing the thermal performance of thermosiphon loop, air cooler, and water during thermal tests on the CPU (i7-930 processor).

Table 7: The comparison of average $\theta_{J\text{-}CW}$ values for air cooler, water cooler, and different thermosiphon loop configurations.

Cooler	Dual Taper Angle	$\theta_{J\text{-}CW}$ (°C)
Air	-	74
Water	-	56
Thermosiphon Loop (TC1)	2°	43
Thermosiphon Loop (TC2)	2.5°	45
Thermosiphon Loop (TC3)	3°	49

A thermosiphon loop containing an evaporator with single taper manifold was also tested to demonstrate the superior heat dissipation performance the dual taper. Figure 61 shows the cooling performance comparison of single and dual taper configurations of thermosiphon loop. The dual taper maintains lower $\theta_{J\text{-}CW}$ value throughout the baseline and stress test. Higher pressure drop occurs in single taper configuration due to larger flow length. The higher pressure drop causes reduced flow rate in single taper system and the heat dissipation performance suffers. Also, the liquid inertia reduces significantly along the flow length in single taper configurations due to high degree of cross section expansion. These factors lead to inefficient vapor removal from microchannels surface in the evaporator thus reducing the heat transfer performance of the single taper evaporator.

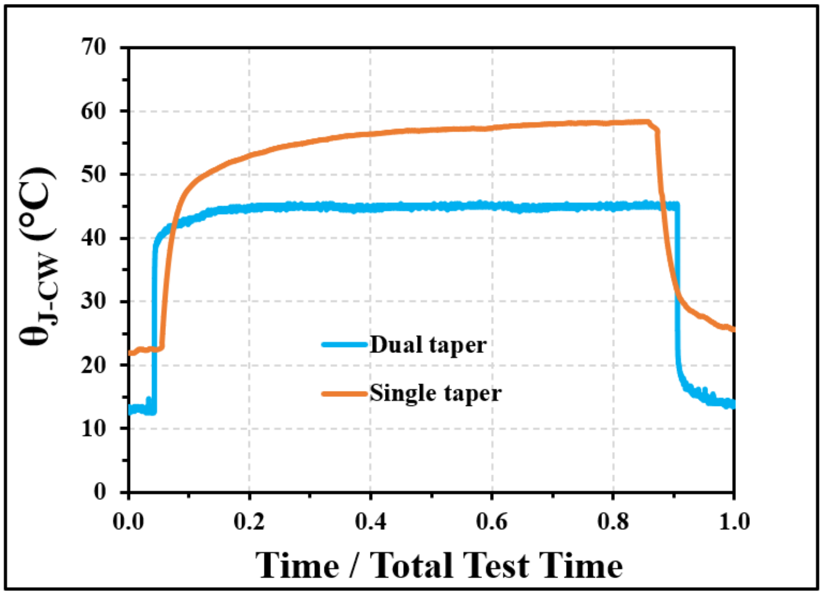

Figure 61: Plot showing the thermal performance of single taper and dual taper manifolds in thermosiphon during thermal tests on the CPU.

A flow boiling loop can also be implemented as a CPU cooling technique for high heat flux dissipation. The flow boiling system may obtain lower CPU temperature compared to thermosiphon loop, but it requires an additional continuous pumping power for fluid circulation. The primary advantage of a thermosiphon loop compared to a flow boiling loop is the absence of a pump and additional system components. The microchannels chip used in the evaporator of the thermosiphon loop may contain nanostructured surfaces or porous coating to improve the heat dissipation efficiency but this will add significant cost to the cooling process for any large scale application such as data center.

7.4 Comparison of Thermosiphon Loop, Air Cooler, and Water Cooler under High Heat Flux Conditions

7.4.1 Experimental Setup

In this study, the three CPU coolers – SilenX air cooler, Alienware water cooler, and thermosiphon cooler with 2.5° dual taper were tested on the mock CPU which was used earlier in the benchtop thermosiphon loop testing. The experimental setup and procedure were same as described in Section 7.2. Since the heat flux generated by an actual CPU (i7-930) was limited to 12 W/cm^2, mock CPU was used in this study to compare the heat dissipation performance of three coolers under high heat flux conditions. Following the current miniaturization trend in electronics, high heat flux dissipating coolers are needed in the industry. The schematic of the experimental setup for three coolers is shown in Fig. 62. The diameter of the evaporator footprint in the thermosiphon loop is the same as the commercial water cooler used in the study, 68mm. The evaporator is designed such that the mounting bracket of water cooler can be used to mount the evaporator of thermosiphon loop as well. The heights of the evaporator, water cooler, and air cooler are 29mm, 57mm, and 105mm respectively therefore, the evaporator of the thermosiphon loop occupies minimum space in the server.

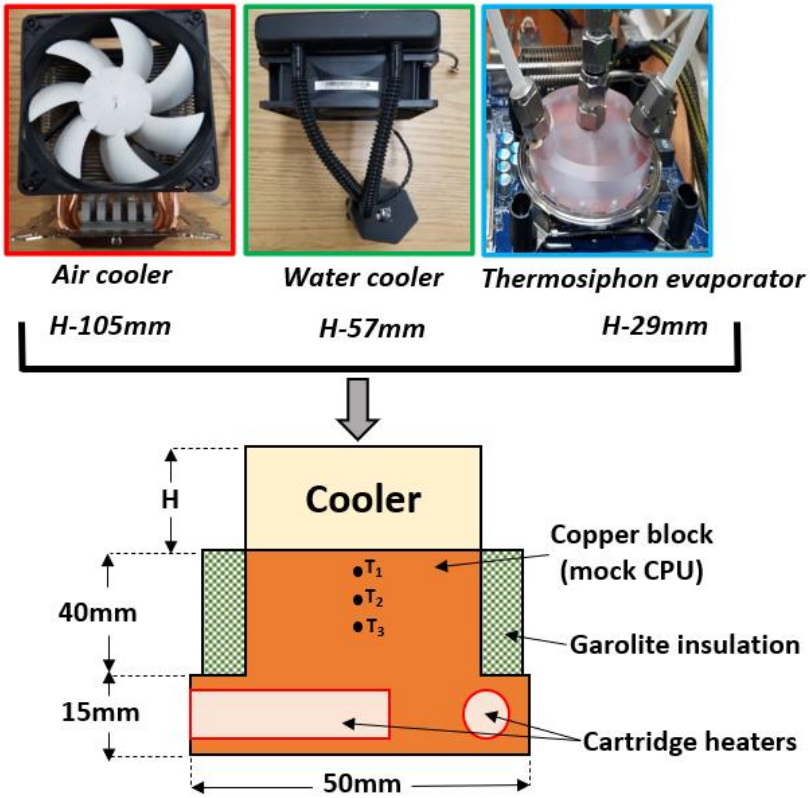

Figure 62: Schematic of the mock CPU heater and actual pictures of different coolers used in the study. 'H' represents the height of each cooler mounted on the top of mock CPU.

7.4.2 Heat Transfer Results

The variation in heat flux with respect to corresponding $\theta_{J\text{-}CW}$ values for SilenX air cooler, Alienware water cooler, and thermosiphon cooler are shown in Fig. 63. The thermosiphon loop with 2.5° dual taper was able to dissipate highest heat flux; 25 W/cm^2 at $\theta_{J\text{-}CW}$ of 36.5ºC without reaching the critical heat flux (CHF). The air cooler and water cooler were able to dissipate 9 W/cm^2 and 19 W/cm^2 at $\theta_{J\text{-}CW}$ 52ºC and 50ºC, respectively. This performance plot does not represent the maximum heat dissipation limit of any cooler, the objective of this study is to identify the cooling performance trend of three coolers for high power density applications. Therefore, it can be concluded that thermosiphon loop develops efficient cooling at high heat fluxes compared to air, and water based coolers.

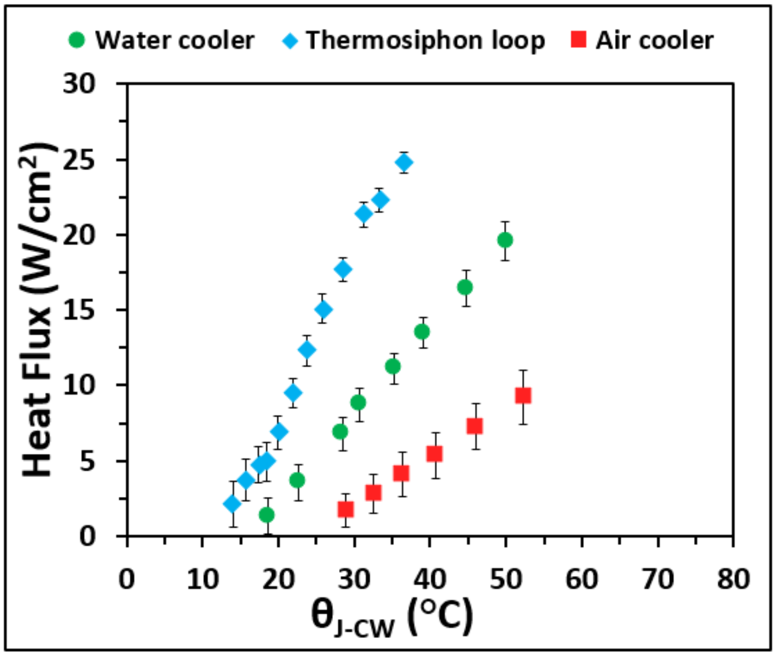

Figure 63: Plot showing the thermal performance of thermosiphon loop, air cooler, and water during thermal tests on the mock CPU under varying heat flux conditions.

7.5 Major Outcomes from the Experimental Thermosiphon Loop Study

In this chapter, an innovative dual tapered manifold in the evaporator of a thermosiphon loop is evaluated for CPU cooling application in a server in data center. The cooling performance of the thermosiphon loop was compared with the commercially available air and water-based coolers.

The benchtop thermosiphon loop testing was performed on a mock CPU with three different dual taper angles in the manifold – 2º, 2.5º, and 3º. The performance of 2° dual taper angle was the best among all tested configurations. The 2° taper was able to dissipate 280W without reaching critical heat flux and this value was limited by the efficiency of the copper coil in the condenser. The heat transfer coefficient of 22.5 kW/m^{2º}C at a surface temperature of 45.5ºC was obtained for 2° taper. Due to dual tapered manifold in thermosiphon loop, reduced pressure drop results in achieving a higher flow rate, which is helpful in improving both CHF and HTC. However, as the taper increases, the heat transfer performance deteriorates due to reduced fluid velocities at the outlet of the tapered manifold. Hence for any specific geometry and the fluid used in the evaporator, there is an optimum taper angle to dissipate heat most efficiently.

In the thermosiphon loop during actual CPU cooling application, the evaporator of the thermosiphon loop was installed on the motherboard in direct contact with the CPU (i7-930 processor). The cooling performance of thermosiphon loop was compared with SilenX air cooler, and Alienware water cooler during thermal stress test. The performance comparison parameter, $\theta_{J\text{-}CW}$ was defined as the temperature difference between the junction (or mock CPU surface) and the chilled water temperature for all three coolers. Thermosiphon cooler with 2° dual taper angle maintained the minimum $\theta_{J\text{-}CW}$ value at 43ºC during the thermal stress test and the values for water, and air based coolers were 56°C and 74°C respectively. Also, the other taper angles – 2.5°, and 3° obtained smaller $\theta_{J\text{-}CW}$ values compared to air, and water coolers hence establishing superior heat dissipation performance.

The benchtop comparison of thermosiphon, air, and water CPU coolers was also studied on a mock CPU to compare the cooling performance of different coolers under high heat flux conditions. The thermosiphon loop with 2.5º dual taper angle was able to dissipate 25 W/cm^2 at $\theta_{J\text{-}CW}$ of 36.5ºC without reaching the CHF. The air and water coolers were able to dissipate 9 W/cm^2 and 19 W/cm^2 at $\theta_{J\text{-}CW}$ 52ºC and 50ºC, respectively. These heat flux values does not represent the maximum heat dissipation limit of the coolers; these values were obtained to obtain the performance trend for different coolers.

7.6 Design Guidelines

Based on the experience gained from the experimental study where thermosiphon evaporator was mounted directly on the CPU, some of design guidelines are provided in this section. The heat transfer performance in a thermosiphon loop can be enhanced by sustaining the two-phase flow stability with continuous surface rewetting. This can be obtained by evaluating the effect of various operational parameters such as the type of working fluid, the head between the evaporator and the condenser, and the pressure drop. The design parameters such as taper angle, inlet gap height, and flow length also need to be considered depending on the targeted CPU.

1) Type of working fluid: In the presented work HFE7000 was used as the working fluid. HFE7000 is a dielectric fluid, hence it can be used in electronics application. Also, the low saturation temperature, 34°C at 1 atm, allows in establishing the two-phase heat transfer under a no stress conditions. The working fluid can be changed depending on the saturation temperature and latent heat requirements. It is suggested to use a dielectric fluid in electronics cooling application considering the safety of the electronic devices. Water as the working fluid will provide the best cooling performance, but such loop requires operation in vacuum condition, and this adds complexity to the cooling structure. Also, the possibility of leakage leading to a catastrophic failure of the expensive electronic equipment have prevented the widespread usage of water in thermosiphon loops for electronics cooling application.

2) Head between the evaporator and the condenser: Based on the compatibility of the thermosiphon loop with the racks at RIT’s data center, a head of 0.87 m was developed between the evaporator and the condenser. The head between the evaporator and the condenser helps in developing the fluid inertia across the tapered boiling region. The greater head develops higher fluid inertia at the inlet of the evaporator therefore increases the heat transfer rate. In general, it is suggested to use the highest available head based on the space and piping constrains in the server room.

3) Pressure drop: The flow instability or fluctuations results in reversed flow in the evaporator leading to high pressure drops and this degrades the cooling performance of the thermosiphon loop. Also, increasing the flow lengths result in high pressure drops. The use of dual paper is suggested to reduce the flow length for a given tapered manifold. For larger evaporators than those tested in this study, further increasing the number of differed tapered regions with multiple inlets and outlets may be considered to reduce the pressure drop.

4) Effect of flow length and taper angle: The flow length and taper angle affect the total pressure drop along the boiling domain significantly. The taper angle provides additional expanding volume along the flow length towards the evaporator outlet. This allows bubble to grow in the vertical space above the heating surface thus avoiding lateral dry outs. Therefore, a stable fluid flow can be established with a lower pressure drop using such configuration. A detailed theoretical analysis on pressure recovery effect due to tapered region is discussed earlier in Chapter 4. The value of taper angle can be increased until an optimized value is obtained depending on the flow length and flow width. This optimization process requires an independent parametric study for a specific evaporator design.

In a tapered region, due to the continuous expansion in the flow domain, the fluid inertia continuously decreases along the flow length. Hence, a greater expansion is experienced for larger flow lengths resulting in inefficient bubble removal especially towards the evaporator outlet and an overall performance deterioration. For the same taper angle, the dual taper design allows lesser expansion along the flow direction compared to the single taper design since the flow length is reduced by half. In a dual taper configuration, adequate fluid inertia is maintained along the flow length for smaller taper angles therefore resulting in a better thermal performance.

Chapter 8

8.0 High Speed Visualization and Theoretical Analysis of Bubble Squeezing Mechanism

The bubble squeezing mechanism in the tapered microgap section provides a liquid pumping effect from the bulk into the microgap. The bubble nucleation, bubble expansion, and departure in the microgap are discussed in this chapter. The high-speed images of bubble growth and departure were obtained for different taper angles and inlet gap heights using water as the working fluid. The stable and unstable bubble expansion cases were obtained, and the interface tracking of a single bubble provided insight into motion of the receding and advancing interfaces. A preliminary force balance on a single squeezed bubble is also presented under static conditions.

8.1 Experimental Setup

The schematic of the experimental setup used to obtain the high-speed images of the bubble squeezing mechanism with water as the working fluid is shown in Fig.64. The setup contains a boiling test section at top and a heating assembly at the bottom. The boiling test section is supported on an adjustable platform with a copper test chip held in a ceramic chip holder. The ceramic is used to prevent heat losses from the heated test chip. The edges of the copper test surface are covered by kapton tape providing a 10 mm x 10 mm boiling surface for the bubble nucleation. A polysulfone block with a tapered surface is placed over the copper test chip in the liquid reservoir. The tapered surface on the block is machined based on the required taper angle in the microgap. The two taper angles (α) used in this study are 2°, and 10°. The inlet gap height (h_i) between the edge of the tapered surface and copper test surface varies from 0.35 mm to 1.2 mm. The saturated water was contained in a quartz glass reservoir to achieve clear visualization. The quartz reservoir was pushed against the test chip using hex screws with a silicon gasket between the reservoir and the test chip.

At the bottom, a copper heater block assembly was used to heat the copper test chip. The heater assembly was supported on compressed springs. The springs pushes the heater block against the test chip to reduce the contact resistance. To further minimize the contact resistance a grafoil sheet was placed between the test chip and the heater block. Four cartridge heaters (200 W each) were inserted in the heater block. The cartridge heaters were connected to an external DC power supply. Three K-type thermocouples (T_1-T_3) were inserted in the copper test chip to measure the temperature gradient in the test chip. A

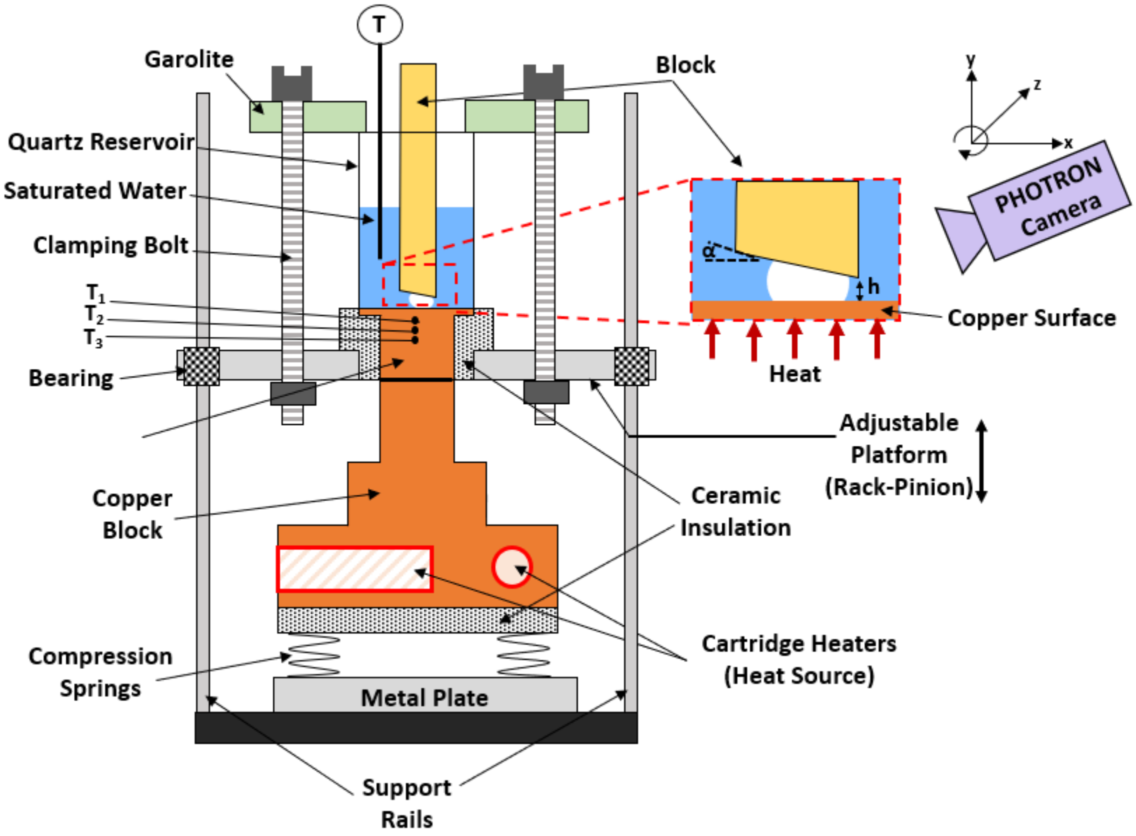

Figure 64: Schematic of the experimental setup used for obtaining high-speed imaging of bubble squeezing mechanism in the tapered microgap.

Photron high speed camera was placed adjacent to the test surface supported on a four axes platform. The platform allows smooth motion control of the camera thus helps in achieving the required focus on the targeted bubbles.

8.2 Experimental Procedure

The quartz tube reservoir was initially filled with the saturated water before each high-speed recording. The DC power supply was turned on and the voltage was supplied to the cartridge heaters in the copper heater block. The videos were obtained at low heat flux ~ 5 W/cm^2 to obtain clear visualization. At higher heat fluxes, the clear visualization is not achieved due to generation of multiple ‘rogue bubbles’ along the edge of the silicon gasket. The saturation state of the water reservoir was observed using a K-type thermocouple during the recordings. The tapered block was inserted in the water reservoir and the nucleating bubble was squeezed between the copper test chip and the tapered surface in the expanding microgap.

The high-speed videos for different taper angles and inlet gap heights were recorded at 2000 fps (frames per second) using a PHOTRON high speed camera using a Photron Fastcam View (PFV) software. The pixel size in the videos was determined by observing a wire of known diameter before each recording. The high-speed videos were post processed in the Photron Fastcam Analyzer (PFA) software to obtain the images and velocity data as presented in this chapter.

8.3 Stable Bubble Expansion in Tapered Microgap

During the actual boiling application in a tapered microgap, a stable bubble expansion is preferred along the expanding cross section. This creates the required unidirectional two-phase flow and the liquid pumping effect along the flow domain. The stable bubble expansion was observed for 10° taper angle with 0.8 mm inlet gap, and 10° taper angle with 1.2 mm inlet gap.

8.3.1 10° taper angle with 0.8 mm inlet gap: The high-speed images of the sequence of stable bubble squeezing mechanism obtained for the 10° taper angle with 0.8 mm inlet gap are shown in Fig. 65. The bubble interface is shown by red dotted lines and the cross-sectional area in the tapered microgap increases from right to left, therefore the bubble expansion and departure is expected from right to left as shown by the blue arrows. In the first image at t = 0s, two bubbles of different sizes are observed on the surface of the copper test chip in the tapered microgap. The bigger bubble on the left is in contact with the tapered surface and a smaller bubble nucleates on the right side near the inlet of the microgap. In the second image at t = 0.059s, the bubble near the inlet of the microgap meets the tapered surface and expands towards the right side outside the microgap. In the third image at t = 0.114s, the bubbles continue to expand and begin to coalesce towards the left to form a bigger bubble at t = 0.1255s as shown in the fourth image. In the fifth image at t = 0.1385s, the big bubble continues to move towards left and exits the microgap at t = 0.1845s. This provides space for bubble nucleation and a new bubble nucleates near the inlet as shown in the sixth image. The bubble departure along the taper causes liquid pumping effect into the microgap from the right side.

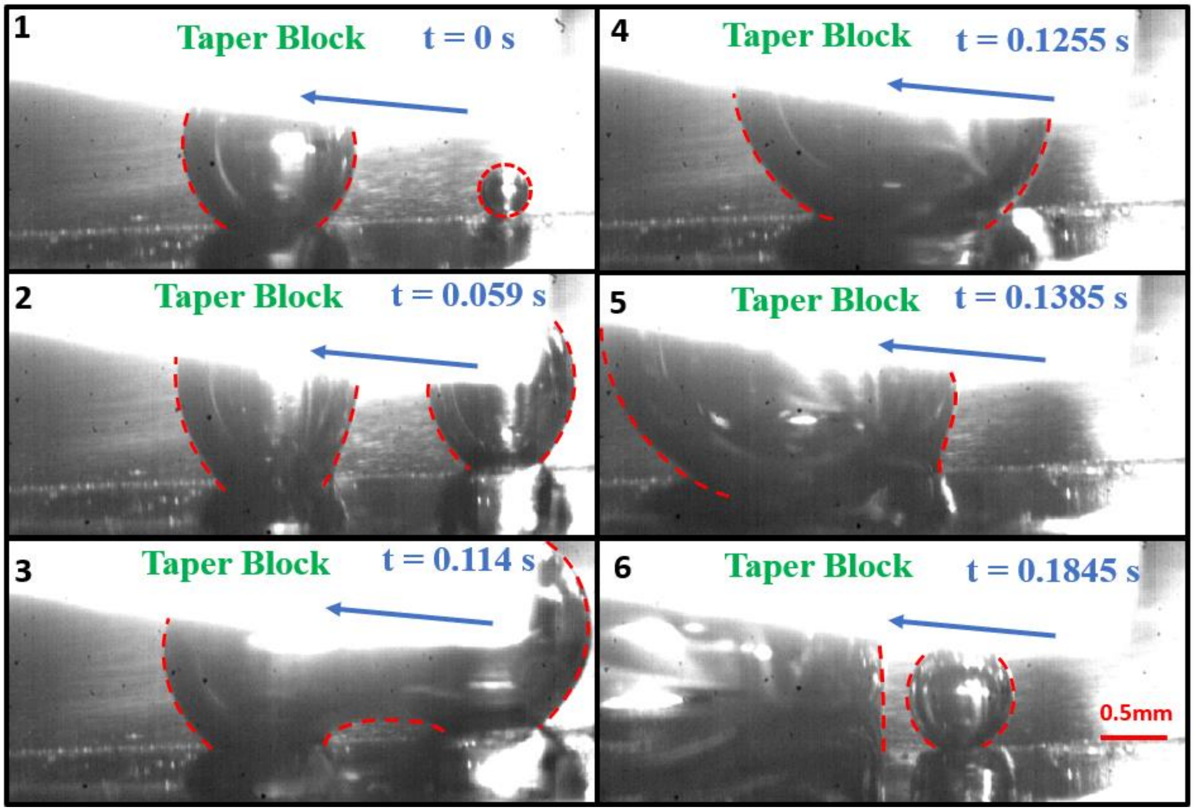

Figure 65: Bubble squeezing mechanism in tapered microgap with 10º taper angle and 0.8 mm inlet gap height.

8.3.2 10° taper angle with 1.2 mm inlet gap: The high-speed imaging of bubble squeezing mechanism in 10º taper angle with 1.2 mm inlet gap is shown in Fig.66. The cross-sectional area in the microgap increases from right to left, therefore the expected bubble expansion is from right to left as shown by the blue arrows. In the first image at t = 0s, three bubbles are shown in the microgap on the copper surface. The bubble near the inlet is bigger and is in direct contact with the taper block. In the second image at t = 0.07s, the bubbles begin to coalesce and form a bigger coalesced bubble at t = 0.1905s as shown in the third image. Also, a bubble nucleates near the inlet of the microgap. In the fourth image at t = 0.136s, the coalesced bubble has expanded towards left and the smaller bubble near the inlet continues to grow. The big expanding bubble and the smaller bubble coalesce at t = 0.1445s to form a vapor lump as shown in the fifth image. In the sixth image at t = 0.178s, the expanding bubble leaves the microgap and two bubbles nucleate near the inlet. The departure of the bubble causes liquid inflow from right side on the heater surface into the microgap.

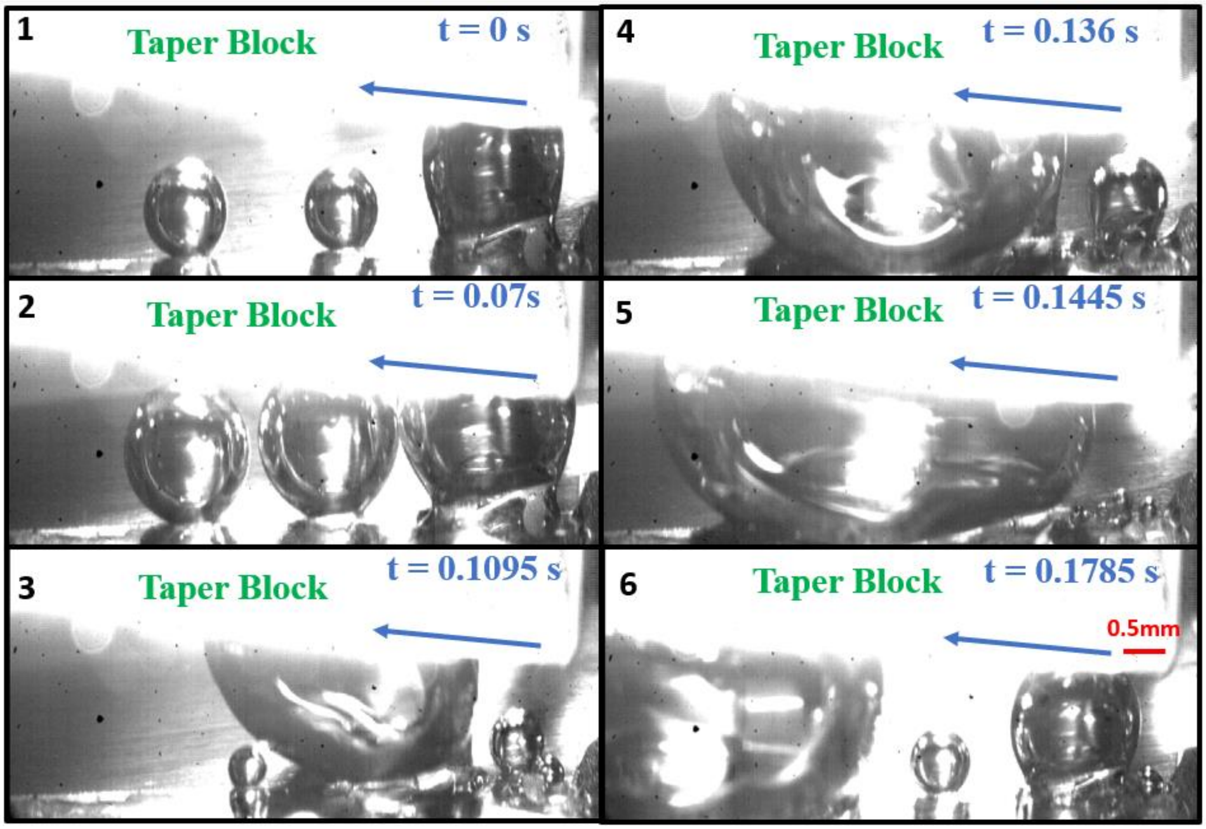

Figure 66: Bubble squeezing mechanism in tapered microgap with 10° taper angle and 1.2 mm inlet gap height.

8.4 Unstable Bubble Expansion in Tapered Microgap

The unstable bubble expansion was observed for 10° taper angle with 0.35 mm inlet gap, and 2° taper angle with 1mm inlet gap. For these configurations, the bubble leaves the tapered microgap region from side, perpendicular to the desired flow direction along the taper.

8.4.1 10° taper angle with 0.35 mm inlet gap: Figure 67 shows the sequence of bubble squeezing mechanism for 10^{o} taper angle and 0.35mm inlet gap. The cross-sectional area in the microgap increases from right to left, therefore the expected bubble expansion is from right to left as shown by the blue arrows. The bubble interface is shown by red dotted lines. Unlike the two cases discussed previously in stable bubble expansion section, in this case unstable bubble expansion was observed perpendicular to the flow direction. In the first image at t = 0s, a nucleated bubble on the copper surface was observed in contact with the taper block at the top and the bubble begins to grow along the taper towards left. In the second image at t = 0.0315s, the bubble continues to grow along and a second bubble nucleates near the inlet of the microgap. In the third image at t = 0.048s, both bubbles grow along the taper and continue to expand towards left side as observed in the fourth image at t = 0.052s. In the fifth image at t = 0.0565s, the two expanding bubbles coalesce to form a large vapor lump significantly occupying the flow space in the microgap. In the sixth image at t = 0.068s, the unstable vapor expansion is observed, and the bubble leaves the microgap, in the direction perpendicular to the blue arrow. This type of bubble departure is not desired in a pool boiling system.

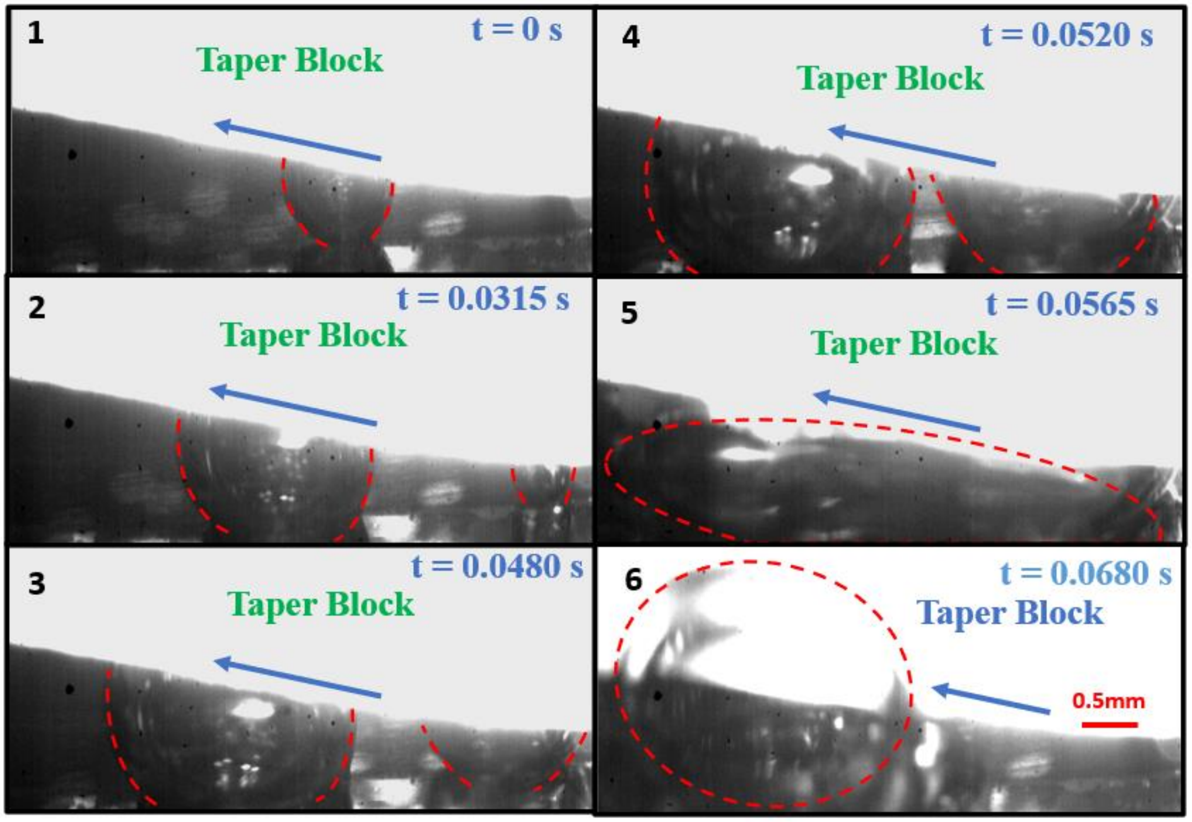

Figure 67: Bubble squeezing mechanism in tapered microgap with 10º taper angle and 0.35 mm inlet gap height.

8.4.2 2° taper angle with 1 mm inlet gap: Figure 68 shows the sequence of bubble squeezing mechanism for 2º taper angle and 1mm inlet gap. The cross-sectional area in the microgap increases from left to right, therefore the expected bubble expansion is from left to right as shown by the blue arrows.

The bubble interface is shown by the red dotted lines. In the first image at t = 0s, multiple nucleated bubbles are observed on the heated copper surface. In the second image at t = 0.029s, the multiple bubbles coalesce to form two large bubbles. The two large bubbles begin to leave the microgap region from the side like previous case with '10º taper angle and 0.35mm inlet gap'. In the third image at t = 0.0385s, the two large bubbles coalesce to form a big vapor lump and occupy significant space along the taper length. This vapor lumps leaves the tapered microgap from the side perpendicular to the desired flow direction.

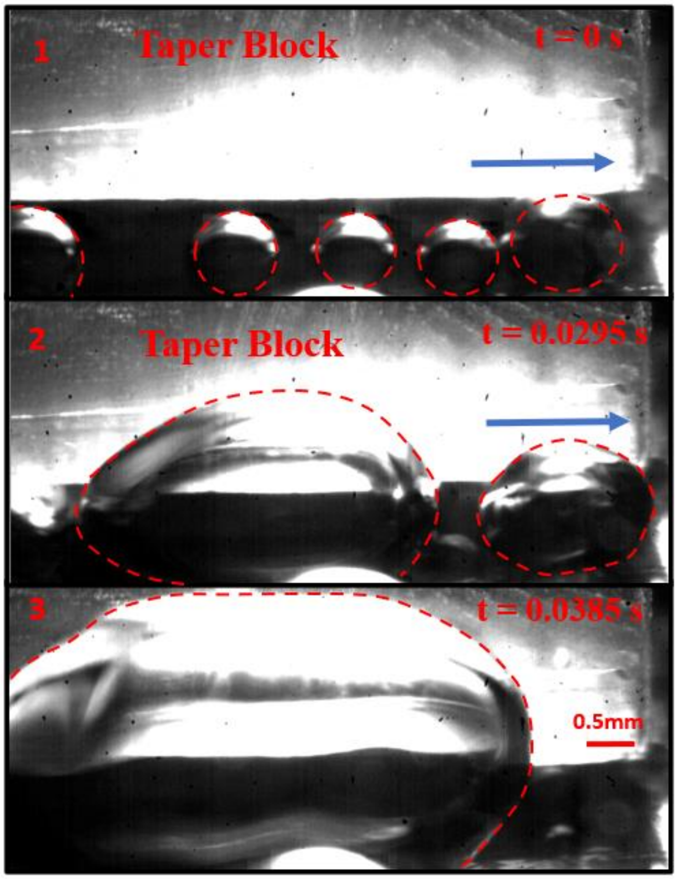

Figure 68: Bubble squeezing mechanism in tapered microgap with 2° taper angle and 1 mm inlet gap height.

8.5 Advancing and Receding Interface Motion

The motion of advancing and receding interfaces was tracked during the bubble expansion process for a 10° taper angle as shown in Fig. 69. The aim is to analyze the interface velocities and develop an insight into the liquid pumping effect.

In Fig. 69, the bubble nucleates at t = 0s and comes in contact with the surface of the tapered block at t = 0.014s. The bubble continues to expand in the microgap at t = 0.164s; the receding interface moves slightly in the upstream direction and the advancing interface moves in the downstream direction. During this bubble expansion the contact line of the receding interface is pinned on the copper surface. At t = 0.211s, the receding interface being pinned at the copper surface has also moved in the downstream direction. At t = 0.304s, the advancing interface has moved significantly along the downstream. The receding interface remains pinned at the copper surface and moves slightly on the taper block surface. At t = 0.43s, the advancing interface has left the microgap region, and the receding interface has moved quickly in the downstream direction.

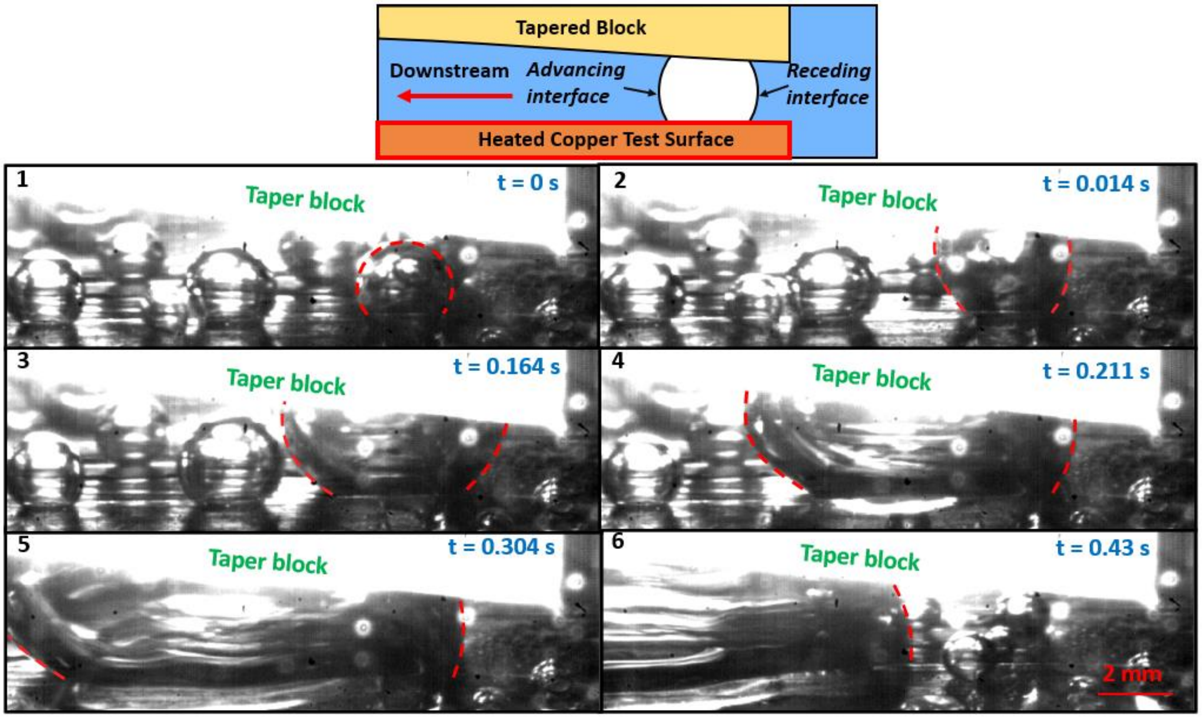

Figure 69: High speed images of bubble squeezing mechanism in a 10° tapered microgap to track the advancing and receding interface velocities along the downstream direction.

The interface velocities along the downstream direction were tracked for the advancing and receding interfaces as shown in Fig. 70. In the beginning, the advancing interface attains downstream velocity, while the receding interface shows no downstream motion. This indicates the overall bubble expansion in the downstream direction. Eventually, the receding interface moves explosively along the downstream at a high velocity exceeding 1 m/s. This interface motion causes liquid pumping effect into the microgap from the inlet end. This study was conducted at low heat flux ~5 W/cm^2. In an actual pool boiling system, high interface velocities will be developed at high heat fluxes, therefore significantly higher liquid pumping effect will be created. This transforms a conventional pool boiling system into a pumpless local flow boiling system, leading to heat transfer enhancement in a tapered microgap design.

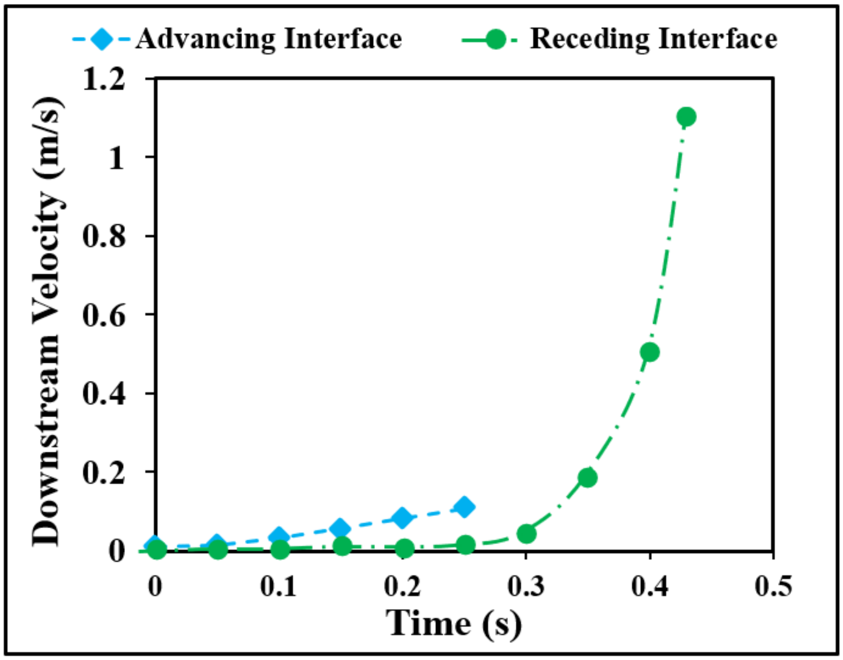

Figure 70: Plot showing the advancing and receding interface velocities with respect to time for a 10° taper angle.

8.6 Force Balance during Bubble Squeezing

An insight into the forces acting on a bubble during squeezing mechanism in a tapered microgap is discussed in this section. A bubble growing in the microgap experiences a rapid bubble growth and it contacts the tapered surface of the manifold block. The bubble in such narrow passages experiences explosive growth as presented in the literature [70,71]. The maximum pressure inside the bubble is dictated by the saturation pressure corresponding to the wall temperature. A two-dimensional force balance was developed on a growing bubble based on the approach successfully used by Mikic, Rohsenow and Griffith [72]. Figure 71 shows the forces per unit length acting on a squeezed bubble at the advancing and receding interfaces. The different forces acting on the interfaces are (a) surface tension ($F_{\sigma 1}$ and $F_{\sigma 2}$), (b) pressure difference forces (F_{p1} and F_{p2}), and (c) evaporation momentum forces (F_{em1} and F_{em2}).

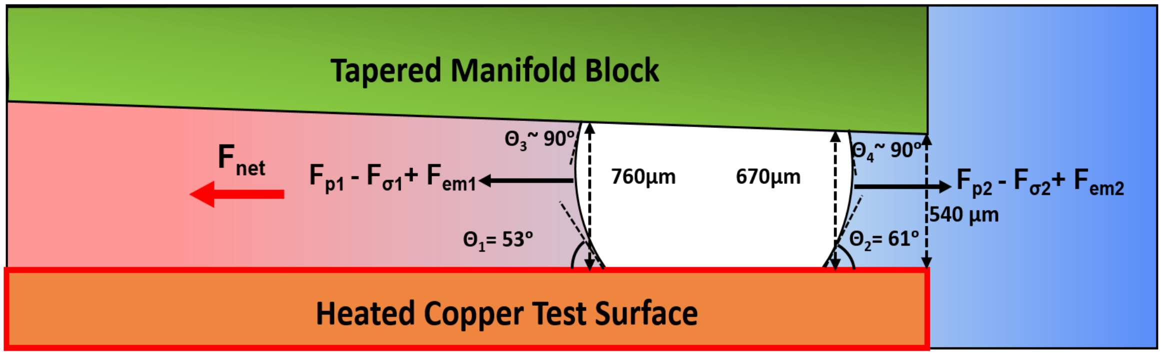

Figure 71: Schematic of forces acting on a squeezed bubble in the tapered microgap.

The net force (F_{net}) acting on the bubble along the increasing cross-section is given by Eq.15.

$$F_{net} = (F_{\sigma 2} - F_{\sigma 1}) + \left(F_{p1} - F_{p2}\right) + (F_{em1} - F_{em2}) \qquad (15)$$

Where, $F_{\sigma 1} = \sigma Cos\Theta_1$ and $F_{\sigma 2} = \sigma Cos\Theta_2$, and σ is the surface tension. Θ_1 and Θ_2 are the contact angles at the copper test surface. The contact angles and the other dimensional parameters as shown in Fig. 71 were obtained from the high-speed images. The contact angles for the advancing and receding interfaces at the surface of the manifold block are close to 90° and therefore the surface tension forces along downstream direction at the upper edges are neglected. Based on the surface tension at the heated copper surface, the net surface tension force in the upstream direction $(F_{\sigma 1} - F_{\sigma 2})$ i.e., against the expanding cross-section was 0.0058 N/m. The saturation pressure corresponding to a wall superheat of 6°C (based on the experimental data) develops a pressure difference of 25 kPa. The maximum net pressure force was calculated based on the area increase corresponding to the height difference (760 μm - 670 μm = 90 μm) between the interfaces and the pressure difference of 25 kPa. The calculated maximum net pressure force per unit length $(F_{p1} - F_{p2})$ was 2.25 N/m in the downstream direction i.e., along the expanding cross-section. The magnitude of the pressure forces is significantly higher than the surface tension forces at the interfaces.

The evaporation momentum force at the interfaces depends on the interface temperature and governs the motion of the interface at high heat fluxes [73]. The interface temperature is higher at the advancing interface compared to the receding interface since liquid temperature is higher on the left side of the bubble. Therefore, evaporation momentum force is considerably higher in the downstream direction at the advancing interface compared to the upstream direction at the receding interface. Hence, the net downstream force (F_{net}) considering the effects of pressure force, surface tension, and evaporation momentum force drives the explosive bubble growth in the microgap. The F_{net} is further aided by the lower flow resistance due to expanding cross-section in the downstream direction. For future theoretical developments, an accurate representation of the bubble growth can be developed by solving bubble growth equations considering the dynamic effects due liquid inertia, similar to the simulations conducted by Mukherjee and Kandlikar [74].

8.7 Major Outcomes from the High-Speed Imaging Study

The bubble squeezing mechanism was studied by capturing the high-speed videos of bubble growth and departure in the tapered microgap. The taper angle and inlet gap height are critical parameters in developing a stable bubble expansion mechanism in the microgap. The tracking of the interfaces showed that high receding interface velocity is obtained in the downstream direction (in the direction of expanding cross-section) at the end of the bubble growth cycle. This creates a liquid pumping effect into the tapered microgap section. And finally, a preliminary two-dimensional force balance theoretical study was performed on a squeezed bubble, and it was shown that forces due to the vapor pressure in the bubble dominate over surface tension effects and contribute significantly to drive the bubble motion in the downstream direction. The evaporation momentum force also drives the bubble along the downstream direction due to more evaporation at the advancing interface. A more detailed analysis can be developed in the future under dynamic flow conditions. Such modeling development can predict the fluid velocity due to bubble squeezing mechanism and can be coupled with the homogeneous flow model to accurately estimate the mass fluxes in the tapered microgap.

Chapter 9

9.0 Conclusion

9.1 Major Contributions

- A theoretical model was developed and validated to gain the fundamental understanding of two-phase flow characteristics in a tapered microgap geometry. The model presents the stable flow conditions based on pressure drop analysis and predicts the HTC for different working fluids and geometries.
- A dual-tapered manifold block was developed for efficient high heat flux dissipation in pool boiling, and record CHF and HTC values were obtained on a plain copper surface. No surface enhancements are required for efficient high heat flux dissipation, instead a simple, robust, add-on technique was developed for a plain surface.
- A novel evaporator was developed using dual-taper design in thermosiphon loop for CPU cooling in data centers. A significantly enhanced CPU cooling performance was obtained using thermosiphon loop compared to air cooler with heat pipes, and water cooler with microchannels under thermal stressful conditions.

9.2 Theoretical Model for Pressure Drop and HTC Prediction in Pool Boiling

A theoretical model was developed using homogeneous flow model to calculate the pressure recovery due to expanding tapered region and pressure drop due to friction, momentum change, and entrance-exit losses in a pool boiling system. For cases where pressure recovery was able to balance the pressure drop, mass flux values were predicted in the tapered microgap. These mass flux values were used to predict the HTC for different geometrical and operational parameters. The predicted values were validated by comparing with the experimental data. For water, a deviation ~10% was observed near CHF between predicted and experimental values. For HFE7000, a deviation of less than 10% was observed near CHF and the minimum deviation achieved was 3.8% for 20° taper with 0.8 mm inlet gap. The pressure recovery effect creates a stable two-phase flow along the taper, and this enhances the heat dissipation performance of a dual-tapered based pool boiling system on a plain surface. It was observed that pressure recovery effect increases with increase in taper angle, and heat flux. The fluid flow in a tapered microgap is significantly driven by heat flux, therefore the accuracy of theoretical model increases with increase in heat flux. This suggests that pressure recovery effect is dominant at high heat fluxes therefore a stable flow is established near CHF. This was also validated by observing unidirectional flow of vapor columns along the taper in experimental pool boiling study with water.

For cases where pressure drop is always greater than pressure recovery, no predictions could be made using the theoretical model. Such conditions are obtained for small taper angles, and low heat fluxes. For water with 10° taper angle, pressure drop dominates over pressure recovery, but experimental results show enhanced heat dissipation performance and stable two-phase flow in the tapered microgap. For HFE7000, during experimental study reduction in CHF was observed for small taper angles and enhanced HTCs were achieved for all heat fluxes. For these cases, the bubble squeezing mechanism provides the required liquid pumping action to establish flow in the microgap. The effect of bubble squeezing on fluid flow rate should be considered for future study, this will improve the accuracy of the theoretical model.

9.3 Pool Boiling Performance of Dual Tapered Manifold on Plain Surface

A dual-tapered design was developed to enhance the pool boiling heat transfer on a plain surface. The dual tapered manifold block with 15° taper angle and 1.27 mm inlet gap height obtained a CHF of 288 W/cm^2 on a plain copper surface using water as the working fluid. A 2.3X enhancement in CHF and HTC was observed using this tapered configuration, this is highest reported enhancement on a plain surface without using any modifications such as nano-microstructures, porous coatings, and microchannels. With HFE7000 as the working fluid, a 2X enhancement in HTC was observed using the 25° taper angle with 0.8 mm inlet gap height. Reduction in CHF was observed for 5°, 10°, and 15° taper angles with 0.8 mm, and 1.27 mm inlet gaps due lower pressure recovery effects in smaller taper angles but higher HTC values were obtained for all taper angles and inlet gap height configurations compared to the baseline configuration with no manifold block.

This suggests that efficient high heat dissipation can be achieved in low head systems using a taper design and in futuristic developments, tapered based CPU coolers can be developed where available head space is minimal. The dual taper design creates smaller flow lengths on the heated surface therefore further reducing the pressure drop and improving the flow stability. Therefore, for larger heated surfaces, several dual tapered manifolds can be developed along the length and width of the boiling surface.

9.4 Thermosiphon Loop with Dual Tapered Manifold for CPU Cooling

An innovative dual-tapered manifold design was developed and used in the evaporator of a thermosiphon loop for efficient CPU cooling in data centers. The thermal performance of a dual-tapered manifold was evaluated for efficient high heat flux dissipation in electronics. The tapered manifold design creates a stable two-phase flow on the heated surface, and this improves the heat transfer performance of the system.

The thermosiphon loop using a dual-tapered manifold in the evaporator was able to dissipate 26 W/cm^2 (280 W) from a mock CPU without reaching CHF in a benchtop configuration using HFE7000 as the working fluid. During an actual CPU cooling testing on i7-930 processor under thermal stressful conditions, thermosiphon loop showed superior heat dissipation efficiency compared to air cooler with heat pipes, and water-based cooler with microchannels. The performance of thermosiphon loop was also compared with air, and water coolers on a mock CPU under high heat flux conditions. This study was conducted considering the high heat flux dissipation demands from futuristic CPUs installed in the servers. Significantly superior cooling performance was obtained using thermosiphon loop at high heat fluxes, since thermosiphon loop is heat flux driven system, the flow stability increases with increase in heat flux resulting in improved heat transfer.

This study shows the CPU cooling potential of thermosiphon loop in data centers, where a single condenser can be installed on the top of each rack feeding liquid to several evaporators installed in multiple servers along the rack. The head between the condenser and the evaporators can be decided based on the available space and piping constraints in the room. In thermosiphon study, HFE7000 was used as the working fluid due its dielectric nature and such fluids are preferred in electronics cooling applications. But water is also adopted for cooling high power density CPUs in data centers, considering such applications water can be used in a pressure-controlled thermosiphon loop with dual-tapered evaporator and significantly high heat fluxes can be dissipated while maintaining low CPU temperatures.

9.5 High Speed Visualization and Theoretical Analysis of Bubble Squeezing Mechanism

The bubble squeezing mechanism creates a liquid pumping effect along the heater surface due to sudden vapor expansion and bubble departure along the taper. High fluid velocities can be obtained in a pool boiling system using a tapered design, and this transforms a conventional pool boiling system into a local flow boiling system. The bubble interface motion was studied for different tapered configurations by capturing high-speed images of bubble growth in the microgap, and interface velocities were obtained causing liquid pumping effect. For water as the working fluid, it was observed that receding interface leaves the tapered microgap region with high velocities greater than 1 m/s at low heat flux ~ 5 W/cm^2. This creates a sudden liquid rush into the tapered microgap, thus improving the surface rewetting. This liquid pumping action increases with increase in heat flux.

A preliminary theoretical analysis was also conducted by capturing the effects of various forces - surface tension, pressure difference, and evaporation momentum. The pressure inside the bubble dominates over surface tension force and drives the interface along towards the increasing cross-section direction along the taper. The evaporation momentum force also drives the bubble motion along the taper due to greater evaporation at the advancing interface. A more detailed bubble squeezing model can be developed in the future to evaluate the effect of squeezing mechanism on fluid flow rates.

10.0 References

[1] I. Ferain, C.A. Colinge, J.-P. Colinge, Multigate transistors as the future of classical metal–oxide–semiconductor field-effect transistors, Nature. 479 (2011) 310–316. https://doi.org/10.1038/nature10676.

[2] I. Staff, Moore's Law, Investopedia. (2003). http://www.investopedia.com/terms/m/mooreslaw.asp (accessed April 13, 2017).

[3] E.R. Masanet, R.E. Brown, A. Shehabi, J.G. Koomey, B. Nordman, Estimating the Energy Use and Efficiency Potential of US Data Centers, Proc. Ieee. 99 (2011) 1440–1453. https://doi.org/10.1109/JPROC.2011.2155610.

[4] R.R. Schmidt, E.E. Cruz, M. Iyengar, Challenges of data center thermal management, IBM J. Res. Dev. 49 (2005) 709–723. https://doi.org/10.1147/rd.494.0709.

[5] A. Capozzoli, G. Primiceri, Cooling Systems in Data Centers: State of Art and Emerging Technologies, Energy Procedia. 83 (2015) 484–493. https://doi.org/10.1016/j.egypro.2015.12.168.

[6] S.G. Kandlikar, Review and Projections of Integrated Cooling Systems for Three-Dimensional Integrated Circuits, J. Electron. Packag. 136 (2014). https://doi.org/10.1115/1.4027175.

[7] Z. Li, S.G. Kandlikar, Current Status and Future Trends in Data-Center Cooling Technologies, Heat Transf. Eng. 36 (2015) 523–538. https://doi.org/10.1080/01457632.2014.939032.

[8] S. Nukiyama, The maximum and minimum values of the heat Q transmitted from metal to boiling water under atmospheric pressure, Int. J. Heat Mass Transf. 9 (1966) 1419–1433. https://doi.org/10.1016/0017-9310(66)90138-4.

[9] M.M. Rahman, E. Ölçeroğlu, M. McCarthy, Role of Wickability on the Critical Heat Flux of Structured Superhydrophilic Surfaces, Langmuir. 30 (2014) 11225–11234. https://doi.org/10.1021/la5030923.

[10] K.-H. Chu, Y. Soo Joung, R. Enright, C.R. Buie, E.N. Wang, Hierarchically structured surfaces for boiling critical heat flux enhancement, Appl. Phys. Lett. 102 (2013) 151602. https://doi.org/10.1063/1.4801811.

[11] K.-H. Chu, R. Enright, E.N. Wang, Structured surfaces for enhanced pool boiling heat transfer, Appl. Phys. Lett. 100 (2012) 241603. https://doi.org/10.1063/1.4724190.

[12] Y. Nam, E. Aktinol, V.K. Dhir, Y.S. Ju, Single bubble dynamics on a superhydrophilic surface with artificial nucleation sites, Int. J. Heat Mass Transf. 54 (2011) 1572–1577. https://doi.org/10.1016/j.ijheatmasstransfer.2010.11.031.

[13] A. Zou, D.P. Singh, S.C. Maroo, Early Evaporation of Microlayer for Boiling Heat Transfer Enhancement, Langmuir. 32 (2016) 10808–10814. https://doi.org/10.1021/acs.langmuir.6b02642.

[14] P.A. Raghupathi, S.G. Kandlikar, Pool boiling enhancement through contact line augmentation, Appl. Phys. Lett. 110 (2017) 204101. https://doi.org/10.1063/1.4983720.

[15] B.J. Jones, J.P. McHale, S.V. Garimella, The Influence of Surface Roughness on Nucleate Pool Boiling Heat Transfer, J. Heat Transf. 131 (2009) 121009-121009–14. https://doi.org/10.1115/1.3220144.

[16] A.R. Betz, J. Jenkins, C.-J. "CJ" Kim, D. Attinger, Boiling heat transfer on superhydrophilic, superhydrophobic, and superbiphilic surfaces, Int. J. Heat Mass Transf. 57 (2013) 733–741. https://doi.org/10.1016/j.ijheatmasstransfer.2012.10.080.

[17] K.-H. Chu, Y.S. Joung, R. Enright, C.R. Buie, E.N. Wang, Hierarchically structured surfaces for boiling critical heat flux enhancement, Appl. Phys. Lett. 102 (2013) 151602. https://doi.org/10.1063/1.4801811.

[18] M.M. Rahman, E. Olceroglu, M. McCarthy, Role of Wickability on the Critical Heat Flux of Structured Superhydrophilic Surfaces, Langmuir. 30 (2014) 11225–11234. https://doi.org/10.1021/la5030923.

[19] M.M. Rahman, J. Pollack, M. McCarthy, Increasing Boiling Heat Transfer using Low Conductivity Materials, Sci. Rep. 5 (2015) 13145. https://doi.org/10.1038/srep13145.

[20] S. Mori, K. Okuyama, Enhancement of the critical heat flux in saturated pool boiling using honeycomb porous media, Int. J. Multiph. Flow. 35 (2009) 946–951. https://doi.org/10.1016/j.ijmultiphaseflow.2009.05.003.

[21] C.H. Li, T. Li, P. Hodgins, C.N. Hunter, A.A. Voevodin, J.G. Jones, G.P. Peterson, Comparison study of liquid replenishing impacts on critical heat flux and heat transfer coefficient of nucleate pool boiling on multiscale modulated porous structures, Int. J. Heat Mass Transf. 54 (2011) 3146–3155. https://doi.org/10.1016/j.ijheatmasstransfer.2011.03.062.

[22] A. Zou, S.C. Maroo, Critical height of micro/nano structures for pool boiling heat transfer enhancement, Appl. Phys. Lett. 103 (2013) 221602. https://doi.org/10.1063/1.4833543.

[23] A. Jaikumar, S.G. Kandlikar, A. Gupta, Dip Coating of Electrochemically Generated Graphene and Graphene Oxide Coatings to Enhance Pool Boiling Performance, Amer Soc Mechanical Engineers, New York, 2016.

[24] S.G. Kandlikar, Enhanced Macroconvection Mechanism With Separate Liquid–Vapor Pathways to Improve Pool Boiling Performance, J. Heat Transf. 139 (2017) 051501. https://doi.org/10.1115/1.4035247.

[25] S.G. Liter, M. Kaviany, Pool-boiling CHF enhancement by modulated porous-layer coating: theory and experiment, Int. J. Heat Mass Transf. 44 (2001) 4287–4311. https://doi.org/10.1016/S0017-9310(01)00084-9.

[26] S.G. Kandlikar, Controlling bubble motion over heated surface through evaporation momentum force to enhance pool boiling heat transfer, Appl. Phys. Lett. 102 (2013) 051611. https://doi.org/10.1063/1.4791682.

[27] A. Jaikumar, S.G. Kandlikar, Enhanced pool boiling heat transfer mechanisms for selectively sintered open microchannels, Int. J. Heat Mass Transf. 88 (2015) 652–661. https://doi.org/10.1016/j.ijheatmasstransfer.2015.04.100.

[28] A. Jaikumar, S.G. Kandlikar, Pool boiling enhancement through bubble induced convective liquid flow in feeder microchannels, Appl. Phys. Lett. 108 (2016) 041604. https://doi.org/10.1063/1.4941032.

[29] A. Jaikumar, S.G. Kandlikar, Pool Boiling Inversion on Surfaces With Separate Liquid-Vapor Pathways And Enhanced Macroconvection Mechanisms, Amer Soc Mechanical Engineers, New York, 2017.

[30] A. Jaikumar, S.G. Kandlikar, Pool boiling inversion through bubble induced macroconvection, Appl. Phys. Lett. 110 (2017) 094107. https://doi.org/10.1063/1.4977557.

[31] A. Jaikumar, S.G. Kandlikar, Ultra-high pool boiling performance and effect of channel width with selectively coated open microchannels, Int. J. Heat Mass Transf. 95 (2016) 795–805. https://doi.org/10.1016/j.ijheatmasstransfer.2015.12.061.

[32] E.G. Colgan, B. Furman, M. Gaynes, W.S. Graham, N.C. LaBianca, J.H. Magerlein, R.J. Polastre, M.B. Rothwell, R.J. Bezama, R. Choudhary, K.C. Marston, H. Toy, J. Wakil, J.A. Zitz, R.R. Schmidt, A practical implementation of silicon microchannel coolers for high power chips, Ieee Trans. Compon. Packag. Technol. 30 (2007) 218–225. https://doi.org/10.1109/TCAPT.2007.897977.

[33] D. Tuckerman, R. Pease, High-Performance Heat Sinking for Vlsi, Electron Device Lett. 2 (1981) 126–129.

[34] A. Kalani, S.G. Kandlikar, Evaluation of Pressure Drop Performance During Enhanced Flow Boiling in Open Microchannels With Tapered Manifolds, J. Heat Transf.-Trans. Asme. 136 (2014) 051502. https://doi.org/10.1115/1.4026306.

[35] T. Zhang, T. Tong, J.-Y. Chang, Y. Peles, R. Prasher, M.K. Jensen, J.T. Wen, P. Phelan, Ledinegg instability in microchannels, Int. J. Heat Mass Transf. 52 (2009) 5661–5674. https://doi.org/10.1016/j.ijheatmasstransfer.2009.09.008.

[36] K. Balasubramanian, P.S. Lee, L.W. Jin, S.K. Chou, C.J. Teo, S. Gao, Experimental investigations of flow boiling heat transfer and pressure drop in straight and expanding microchannels - A comparative study, Int. J. Therm. Sci. 50 (2011) 2413–2421. https://doi.org/10.1016/j.ijthermalsci.2011.07.007.

[37] A. Mukherjee, S.G. Kandlikar, Numerical study of the effect of inlet constriction on bubble growth during flow boiling in microchannels, Amer Soc Mechanical Engineers, New York, 2005.

[38] A. Mukherjee, S.G. Kandlikar, The effect of inlet constriction on bubble growth during flow boiling in microchannels, Int. J. Heat Mass Transf. 52 (2009) 5204–5212. https://doi.org/10.1016/j.ijheatmasstransfer.2009.04.025.

[39] C.T. Lu, C. Pan, Stabilization of flow boiling in microchannel heat sinks with a diverging cross-section design, J. Micromechanics Microengineering. 18 (2008) 075035. https://doi.org/10.1088/0960-1317/18/7/075035.

[40] Y.K. Prajapati, M. Pathak, Mohd. Kaleem Khan, A comparative study of flow boiling heat transfer in three different configurations of microchannels, Int. J. Heat Mass Transf. 85 (2015) 711–722. https://doi.org/10.1016/j.ijheatmasstransfer.2015.02.016.

[41] A. Kalani, S.G. Kandlikar, Preliminary Results of Pressure Drop Modeling During Flow Boiling in Open Microchannels with Uniform and Tapered Manifolds (OMM), Amer Soc Mechanical Engineers, New York, 2014.

[42] A. Kalani, S.G. Kandlikar, Pressure Drop Analysis Using the Homogeneous Model for Open Microchannel with Manifold (OMM), Amer Soc Mechanical Engineers, New York, 2014.

[43] S.G. Kandlikar, T. Widger, A. Kalani, V. Mejia, Enhanced Flow Boiling Over Open Microchannels With Uniform and Tapered Gap Manifolds, J. Heat Transf.-Trans. Asme. 135 (2013) 061401. https://doi.org/10.1115/1.4023574.

[44] A. Kalani, S.G. Kandlikar, Combining liquid inertia with pressure recovery from bubble expansion for enhanced flow boiling, Appl. Phys. Lett. 107 (2015) 181601. https://doi.org/10.1063/1.4935211.

[45] A. Kalani, S.G. Kandlikar, Flow patterns and heat transfer mechanisms during flow boiling over open microchannels in tapered manifold (OMM), Int. J. Heat Mass Transf. 89 (2015) 494–504. https://doi.org/10.1016/j.ijheatmasstransfer.2015.05.070.

[46] A.A. Chehade, H. Louahlia-Gualous, S. Le Masson, I. Victor, N. Abouzahab-Damaj, Experimental investigation of thermosyphon loop thermal performance, Energy Convers. Manag. 84 (2014) 671–680. https://doi.org/10.1016/j.enconman.2014.04.092.

[47] A. Franco, S. Filippeschi, Experimental analysis of Closed Loop Two Phase Thermosyphon (CLTPT) for energy systems, Exp. Therm. Fluid Sci. 51 (2013) 302–311. https://doi.org/10.1016/j.expthermflusci.2013.08.013.

[48] A. Pal, Y.K. Joshi, M.H. Beitelmal, C.D. Patel, T.M. Wenger, Design and performance evaluation of a compact thermosyphon, IEEE Trans. Compon. Packag. Technol. 25 (2002) 601–607. https://doi.org/10.1109/TCAPT.2002.807997.

[49] N. Lamaison, C.L. Ong, J.B. Marcinichen, J.R. Thome, Two-phase mini-thermosyphon electronics cooling: Dynamic modeling, experimental validation and application to 2U servers, Appl. Therm. Eng. 110 (2017) 481–494. https://doi.org/10.1016/j.applthermaleng.2016.08.198.

[50] A. Samba, H. Louahlia-Gualous, S. Le Masson, D. Nörterhäuser, Two-phase thermosyphon loop for cooling outdoor telecommunication equipments, Appl. Therm. Eng. 50 (2013) 1351–1360. https://doi.org/10.1016/j.applthermaleng.2012.05.023.

[51] S.H. Noie, Heat transfer characteristics of a two-phase closed thermosyphon, Appl. Therm. Eng. 25 (2005) 495–506. https://doi.org/10.1016/j.applthermaleng.2004.06.019.

[52] T. Saenen, M. Baelmans, Size effects of a portable two-phase electronics cooling loop, Appl. Therm. Eng. 50 (2013) 1174–1185. https://doi.org/10.1016/j.applthermaleng.2012.08.048.

[53] R.L. Webb, S. Yamauchi, S. Denko, Test results on a thermo-syphon concept to high-power cool desktop computers and servers, in: Eighteenth Annu. Ieee Semicond. Therm. Meas. Manag. Symp. Proc. 2002, Ieee, New York, 2002: pp. 151–158.

[54] R.L. Webb, S. Yamauchi, S. Denko, K.K. Tochigi, Remote heat sink concept for high power heat rejection, Ieee Trans. Compon. Packag. Technol. 25 (2002) 608–614. https://doi.org/10.1109/TCAPT.2003.809109.

[55] P.E. Tuma, Evaporator/boiler design for thermosyphons utilizing segregated hydrofluoroether working fluids, in: P. Wesling, K. Erickson (Eds.), Twenty Second

Annu. IEEE Semicond. Therm. Meas. Manag. Symp. Proc. 2006, Ieee, New York, 2006: pp. 69–77.

[56] M. Moura, E. Teodori, A.S. Moita, A.L.N. Moreira, 2 Phase Microprocessor Cooling System with Controlled Pool Boiling of Dielectrics over Micro-andNano Structured Integrated Heat Spreaders, in: 2016 15th Ieee Intersoc. Conf. Therm. Thermomechanical Phenom. Electron. Syst. Itherm, Ieee, New York, 2016: pp. 378–387.

[57] R. Furberg, R. Khodabandeh, B. Palm, S. Li, M. Toprak, M. Muhammed, Experimental Investigation of an Evaporator Enhanced With a Micro-Porous Structure in a Two-Phase Thermosyphon Loop, (2008) 327–334. https://doi.org/10.1115/HT2008-56471.

[58] R. Khodabandeh, B. Palm, Influence of system pressure on the boiling heat transfer coefficient in a closed two-phase thermosyphon loop, Int. J. Therm. Sci. 41 (2002) 619–624. https://doi.org/10.1016/S1290-0729(02)01355-8.

[59] V. Tsoi, S.W. Chang, K.F. Chiang, C.C. Huang, Thermal performance of plate-type loop thermosyphon at sub-atmospheric pressures, Appl. Therm. Eng. 31 (2011) 2556–2567. https://doi.org/10.1016/j.applthermaleng.2011.04.021.

[60] J.G. Collier, J.R. Thome, Convective Boiling and Condensation, Clarendon Press, 1994.

[61] S.G. Kandlikar, A General Correlation for Saturated Two-Phase Flow Boiling Heat Transfer Inside Horizontal and Vertical Tubes, J. Heat Transf. 112 (1990) 219–228. https://doi.org/10.1115/1.2910348.

[62] A. Kalani, S.G. Kandlikar, Effect of taper on pressure recovery during flow boiling in open microchannels with manifold using homogeneous flow model, Int. J. Heat Mass Transf. 83 (2015) 109–117. https://doi.org/10.1016/j.ijheatmasstransfer.2014.11.080.

[63] W.H. MCADAMS, Vaporization inside horizontal tubes-II, Benzene oil mixtures, Trans ASME. 64 (1942) 193–200.

[64] A. Chauhan, S.G. Kandlikar, High Heat Flux Dissipation Using Symmetric Dual-Taper Manifold in Pool Boiling, in: ICNMM2019, ASME 2019 17th International Conference on Nanochannels, Microchannels, and Minichannels, 2019. https://doi.org/10.1115/ICNMM2019-4292.

[65] A. Chauhan, S.G. Kandlikar, Transforming pool boiling into self-sustained flow boiling through bubble squeezing mechanism in tapered microgaps, Appl. Phys. Lett. 116 (2020) 081601. https://doi.org/10.1063/1.5141357.

[66] T.S. Emery, S.G. Kandlikar, Pool boiling with four non-ozone depleting refrigerants and comparison with previously established correlations, Exp. Therm. Fluid Sci. 85 (2017) 132–139. https://doi.org/10.1016/j.expthermflusci.2017.02.027.

[67] A. Chauhan, S.G. Kandlikar, Effect of Liquid Volume on Thermosiphon Loop Performance Using Open Microchannels Manifold for CPU Cooling in Data Center, in: ASME 2017 15th Int. Conf. Nanochannels Microchannels Minichannels, ASME, Cambridge, Massachusetts, USA, 2017: p. V001T05A002. https://doi.org/10.1115/ICNMM2017-5529.

[68] S.R. Thangavelu, A. Myat, A. Khambadkone, Energy optimization methodology of multi-chiller plant in commercial buildings, Energy. 123 (2017) 64–76. https://doi.org/10.1016/j.energy.2017.01.116.

[69] M. Matkovic, A. Cavallini, D. Del Col, L. Rossetto, Experimental study on condensation heat transfer inside a single circular minichannel, Int. J. Heat Mass Transf. 52 (2009) 2311–2323. https://doi.org/10.1016/j.ijheatmasstransfer.2008.11.013.

[70] S.G. Kandlikar, Nucleation characteristics and stability considerations during flow boiling in microchannels, Exp. Therm. Fluid Sci. 30 (2006) 441–447. https://doi.org/10.1016/j.expthermflusci.2005.10.001.

[71] A. Kalani, S.G. Kandlikar, Flow patterns and heat transfer mechanisms during flow boiling over open microchannels in tapered manifold (OMM), Int. J. Heat Mass Transf. 89 (2015) 494–504. https://doi.org/10.1016/j.ijheatmasstransfer.2015.05.070.

[72] B.B. Mikic, W.M. Rohsenow, P. Griffith, On bubble growth rates, Int. J. Heat Mass Transf. 13 (1970) 657–666. https://doi.org/10.1016/0017-9310(70)90040-2.

[73] S.G. Kandlikar, A Theoretical Model to Predict Pool Boiling CHF Incorporating Effects of Contact Angle and Orientation, J. Heat Transf. 123 (2001) 1071–1079. https://doi.org/10.1115/1.1409265.

[74] A. Mukherjee, S.G. Kandlikar, Numerical simulation of growth of a vapor bubble during flow boiling of water in a microchannel, Microfluid. Nanofluidics. 1 (2005) 137–145. https://doi.org/10.1007/s10404-004-0021-8.

Appendix

Air, and Water Based Coolers

Air based cooler: The air-based cooler used in this study is a 296 g, 2.4 W SilenX EFZ-80HA2 CPU cooler. The actual images of this air cooler is shown in Fig. 72. The cooler is placed in direct contact with the CPU's heat spreader, and arctic silver thermal past is used between the air cooler and heat spreader. The cooler has a copper base with dimensions 45 mm × 35.5 mm and a secondary fin array containing 32 fins (4 row x 8 columns) is also attached on the top of copper base. The measurement of each fin are 4.1 mm × 10 mm × 1.5 mm. There are four copper heat pipes attached on the copper base, these heat pipes run through a primary metallic fin array over the base of the cooler. The outside diameter of each pipe is 6mm. These metallic fins are cooled using a 2.4 W fan with a diameter 80mm. The projected area of the metallic fins along the air flow direction is 6.7 mm × 76.7 mm. There are 36 fins arranged linearly, and the thickness of each is 6 mm. The heat from the CPU conducts into the secondary fin array, but most heat is transferred into the heat pipes. The heat from heat pipes is transferred to the primary fin array, which are cooled by forced convection using the fan.

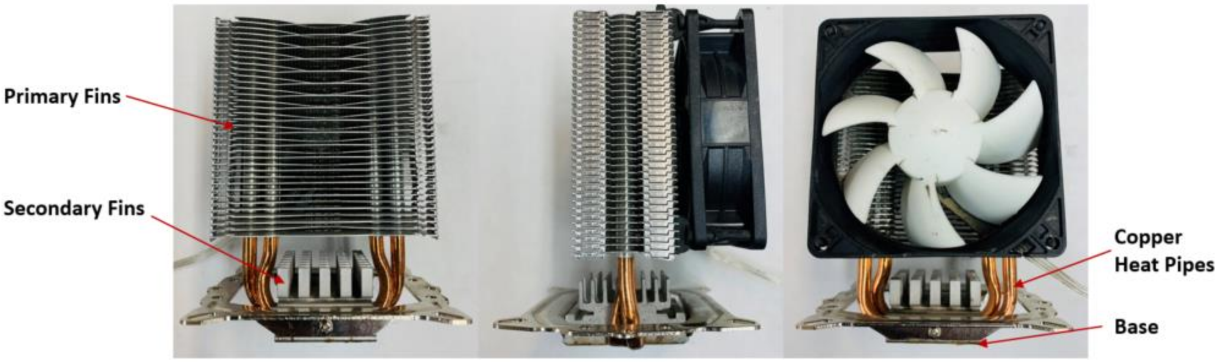

Figure 72: The actual images of air based cooler used in this study.

Water based cooler: The water based cooler used in this study is a 2.5 W Dell Alienware Area 51 W550R PP749 CPU cooler. The two major components in the cooler are the pump, and a fan cooled radiator as shown in Fig. 73. The pump is secured on the CPU with a copper base in direct contact with the CPU's heat spreader. The dimensions of the copper base are 32mm × 34.6mm. The copper base has microchannels on the opposite side which are contained in the pump enclosure. The heat is conducted from the CPU to the microchannels via copper base, and is transferred to the cooling water flowing through the microchannels. The warm water at the outlet of the microchannels is supplied to an external fan cooled radiator. The radiator contains a fin arrangement with projected area of 110mm × 118mm along the air flow direction. The total surface area of the fins is 1478 cm^2. The water flowing through the radiator is cooled using an external fan, and the cold water is supplied back to the microchannels.

Figure 73: The actual images of water-based cooler used in this study.

MATLAB code for calculating net pressure drop in tapered microgap

An example of 20° taper angle with 0.8 mm inlet gap height and HFE7000 as the working fluid is considered here.

```
%Homogeneous flow model and HTC correlation%

%Design parameters%
amm=20; %taper angle in degrees
hmm=0.8; %inlet gap in mm
zmm=4.5; %flow length in mm
wmm=10; %flow width in mm

%Fluid paramters
rhol=1378.55; %Liquid density (HFE7000) at saturation in kg/m^3
rhov=8.49565; %Vapor density (HFE7000) at 1atm in kg/m^3
hfg=142000; %Laten heat of vaporization (HFE7000) in kJ/kg
mewl=0.00037691; %Dynamic viscosity of liquid (HFE7000) in kg/ms
mewv=0.000011277; %Dynamic viscosity of vapor (HFE7000) in kg/ms
vl=(1/rhol); %Specific volume of liquid
vg=(1/rhov); %Specific volume of vapor
kl=0.063293; %Thermal conductivity of liquid

%Operational parameters
q= 20.06; %Experimental heat flux values in W/cm^2, 8 X 1
htcexp= 12.42; %Experimental heat transfer coefficient values in kW/m^2C, 8 X 1

%Calculation begin%
a=amm*pi/180; %taper angle in radians
h=hmm/1000; %inlet gap in m
z=zmm/1000; %flow length in m
w=wmm/1000; %flow width in m
Ain=w*h;
hout=z*tan(a)+h;
Aout=hout*w;
Ac=(Ain+Aout)/2;
dA=Aout-Ain;
Dh1=4*Ain/(2*w+2*h);
Dh2=4*Aout/(2*w+2*hout);
Dh=(Dh1+Dh2)/2;
dPnet=-0.0001;%Error margin
Vdot= 0; %Initial guess value of volume flow rate in ml/min
nloops=1;
while dPnet<0
   Vdot=Vdot+0.1
```

```
Vdot1=(0.0000001/6)*Vdot; %Volume flow rate in m^3/s
mdot=rhol*Vdot1;
G= mdot/((Ain+Aout)/2);
x=(1/hfg)*(q*(z*100)*(w*100)/mdot);%Exit quality
mewtp=1/((x/mewv)+((1-x)/mewl));%two phase dynamic viscosity in kg/ms using McAdams et al. equation
ftp=0.079*((G*Dh/mewtp)^-0.25);%two phase friction factor using Blassius equation
dP1=2*ftp*(G^2)/Dh;
dP2=(vg-vl)*x+vl;
dP3=(G^2)*(vg-vl)*(x/z);
dP=dP1*dP2+dP3;
dPloss=40.5;
dPtotal=dP*z+dPloss;
PR1=(2*(G^2)*vl*dA)/(Ac*z);
PR2=((vg-vl)/vl)*x+1;
PR=PR1*PR2;
PRtotal=PR*z;
dPnet=(PRtotal-dPtotal)/1000 %Net pressure drop in kPa
plot(G,dPnet,"r*");
ylim([-0.05 0.05])
ylabel("Pressure Drop (kPa)")
xlabel("Mass Flux(kg/m^2s)")
pause(0.05)
nloops=nloops+1
end
```

Uncertainty Calculation

The uncertainty analysis similar to that of Emery and Kandlikar [66] was performed for a 95% confidence level for all the recorded data points. The two types of uncertainties considered in this study were, (a) bias error (B_y), and (b) precision error (P_y). The total uncertainty (U_y) can be calculated using Eq. 16 as shown below.

$$\boldsymbol{U_y = \sqrt{B_y^2 + P_y^2}} \qquad (16)$$

The sources of error in the experimental study are thermocouples, thermal conductivity of the copper, and length measurements. The bias error of the thermocouples was determined by calculating the standard deviation of the temperature readings during the calibration process. The calibration process was conducted using a hot cell over a range of known steady state temperature values. The standard deviation value was doubled to obtain the bias error for 95% confidence interval. The precision error of the thermocouples was determined by doubling the standard deviation of the temperature values during the experiments for each steady state condition. The bias uncertainties of the thermal conductivity of copper and length measurements were 9 W/m°C and 10^{-4} m, respectively. The precision or bias errors for the calculated parameters – heat flux, wall superheat, surface temperature, and HTC were calculated using the following general equation.

$$\boldsymbol{U_p = \sqrt{\sum_{i=1}^{n} \left(\frac{\partial p}{\partial \sigma_i} U_{\sigma i}\right)^2}} \qquad (17)$$

Where *p* is any property dependent on independent variable *σ* over *n* samples.

Derivation of Heat Flux Uncertainty

The relation for heat flux, measured from the three heater block thermocouples, is computed from Eqns. (11) and (12) in Chapter 5, and shown below in Eqn. (18)

$$q'' = -k_{Cu}\left(\frac{3T_1 - 4T_2 + T_3}{2\Delta x}\right) \tag{18}$$

The variables in Eq. (18) are substituted into the general equation, as shown earlier in Eq.(17), and the following Eq.(19) is obtained.

$$\frac{U_{q"}}{q"} = \sqrt{\frac{\left(\frac{\partial q"}{\partial k_{Cu}}U_{k_{Cu}}\right)^2 + \left(\frac{\partial q"}{\partial \Delta x}U_{\Delta d}\right)^2 + \left(\frac{\partial q"}{\partial T_1}U_{T_1}\right)^2 + \left(\frac{\partial q"}{\partial T_2}U_{T_2}\right)^2 + \left(\frac{\partial q"}{\partial T_3}U_{T_3}\right)^2}{q"^2}} \tag{19}$$

A new parameter (α) is defined as shown in Eq.(20) for simplifying the next calculation steps.

$$\alpha = 3T_1 - 4T_2 + T_3 \tag{20}$$

The various partial differential expressions in Eq.(19) are calculated using Eq.(18). These calculations are shown below.

$$\frac{\partial q"}{\partial k_{Cu}} = -\frac{\alpha}{2\Delta x} = \frac{q"}{k_{Cu}} \tag{21}$$

$$\frac{\partial q"}{\partial \Delta x} = -k_{Cu}\frac{\alpha}{-2\Delta x^2} = -\frac{q"}{\Delta x} \tag{22}$$

$$\frac{\partial q"}{\partial T_1} = -k_{Cu}\frac{3}{2\Delta x} = \frac{3q"}{\alpha} \tag{23}$$

$$\frac{\partial q"}{\partial T_2} = -k_{Cu}\frac{-4}{2\Delta x} = -\frac{4q"}{\alpha} \tag{24}$$

$$\frac{\partial q"}{\partial T_3} = \frac{-k_{Cu}}{2\Delta x} = \frac{q"}{\alpha} \tag{25}$$

The partial differential terms in Eqns. (21-25) are substituted back into Eq. (19) and following Eq. (26) is obtained.

$$\frac{U_{q''}}{q''} = \sqrt{\frac{\left(\frac{q''}{k_{Cu}} U_{k_{Cu}}\right)^2 + \left(-\frac{q''}{\Delta d} U_{\Delta d}\right)^2 + \left(\frac{3q''}{\alpha} U_{T_1}\right)^2 + \left(-\frac{4q''}{\alpha} U_{T_2}\right)^2 + \left(\frac{q''}{\alpha} U_{T_3}\right)^2}{q''^2}} \quad (26)$$

Eq.(26) is further simplified in two steps to obtain Eq.(28) as shown below. This simplified form is used to calculate uncertainty percentage, and the absolute error values are shown as error bars in the results section.

$$\frac{U_{q''}}{q''} = \sqrt{\frac{\frac{q''^2}{k_{Cu}^2} U_{k_{Cu}}^2 + \frac{q''^2}{\Delta x^2} U_{\Delta x}^2 + \frac{9q''^2}{\alpha^2} U_{T_1}^2 + \frac{16q''^2}{\alpha^2} U_{T_2}^2 + \frac{q''^2}{\alpha^2} U_{T_3}^2}{q''^2}} \quad (27)$$

$$\frac{U_{q''}}{q''} = \sqrt{\frac{{U_{k_{Cu}}}^2}{k_{Cu}^2} + \frac{{U_d}^2}{\Delta d^2} + \frac{9{U_{T_1}}^2}{\alpha^2} + \frac{16{U_{T_2}}^2}{\alpha^2} + \frac{{U_{T_3}}^2}{\alpha^2}} \quad (28)$$

Derivation of Chip Surface Temperature (T_s) Uncertainty

The uncertainty in heat flux is calculated using Eqns. (11) and (13) from Chapter 5 and Eq. (17). Using Eqns. (11) and (13), following Eq. (29) is obtained.

$$T_s = T_4 - \frac{q''}{k_{Cu}} x_1 \quad (29)$$

The variables in Eq.(29) are substituted into the Eq. (17), as shown below in Eq. (30)

$$\frac{U_{T_s}}{T_s} = \sqrt{\frac{\left(\frac{\partial T_s}{\partial T_4} U_{T_4}\right)^2 + \left(\frac{\partial T_s}{\partial q^{"}} U_{q^{"}}\right)^2 + \left(\frac{\partial T_s}{\partial x_1} U_{x_1}\right)^2 + \left(\frac{\partial T_s}{\partial k_{Cu}} U_{k_{Cu}}\right)^2}{T_s^2}} \qquad (30)$$

The partial differential expressions in Eq. (30) are calculated as shown below in Eqns. (31 – 34).

$$\frac{\partial T_s}{\partial T_4} = 1 - 0 = 1 \qquad (31)$$

$$\frac{\partial T_s}{\partial q^{"}} = 0 - 1\left(\frac{x_1}{k_{Cu}}\right) = -\left(\frac{x_1}{k_{Cu}}\right) \qquad (32)$$

$$\frac{\partial T_s}{\partial x_1} = 0 - \frac{q^{"}}{k_{Cu}} = -\frac{q^{"}}{k_{Cu}} \qquad (33)$$

$$\frac{\partial T_s}{\partial k_{Cu}} = 0 + \frac{q^{"} x_1}{k_{Cu}^2} = \frac{q^{"} x_1}{k_{Cu}^2} \qquad (34)$$

The terms in Eqns. (31-34) are substituted in Eq. (30) to obtain the following Eq. (35).

$$\frac{U_{T_s}}{T_s} = \sqrt{\frac{\left(U_{T_4}\right)^2 + \left(-\left(\frac{x_1}{k_{Cu}}\right) U_{q^{"}}\right)^2 + \left(-\frac{q^{"}}{k_{Cu}} U_{x_1}\right)^2 + \left(\frac{q^{"} x_1}{k_{Cu}^2} U_{k_{Cu}}\right)^2}{T_s^2}} \qquad (35)$$

The Eq. (35) is simplified by opening the parentheses in the numerator and following Eq. (36) is obtained, which is further simplified as shown in Eq. (37).

$$\frac{U_{T_s}}{T_s} = \sqrt{\frac{U_{T_4}^2 + \frac{x_1^2}{k_{Cu}^2} U_{q^{"}}^2 + \frac{q^{"2}}{k_{Cu}^2} U_{x_1}^2 + \frac{q^{"2} x_1^2}{k_{Cu}^4} U_{k_{Cu}}^2}{T_s^2}} \qquad (36)$$

$$\frac{U_{T_s}}{T_s} = \sqrt{\frac{U_{T_4}^2}{T_s^2} + \frac{U_{q''}^2 x_1^2}{k_{Cu}^2 T_s^2} + \frac{U_{x_1}^2 q''^2}{k_{Cu}^2 T_s^2} + \frac{U_{k_{Cu}}^2 q''^2 x_1^2}{k_{Cu}^4 T_s^2}} \tag{37}$$

Eq. (37) is used to calculate the percentage uncertainty in the surface temperature. The uncertainty in heat flux which is used in this expression can be obtained from Eq. (28).

Derivation of Heat Transfer Coefficient (HTC) Uncertainty

In this derivation the HTC is shown by the parameter ‘h’ to make the equations simple. Using Eqns. (14 and 15), following Eq.38 is obtained to calculate the HTC (h).

$$h = \frac{q''}{T_s - T_{sat}} \tag{38}$$

The variables in Eq. (38) are substituted in Eq. (17) and following Eq. (39) is obtained.

$$\frac{U_h}{h} = \sqrt{\frac{\left(\frac{\partial h}{\partial q''} U_{q''}\right)^2 + \left(\frac{\partial h}{\partial T_s} U_{T_s}\right)^2 + \left(\frac{\partial h}{\partial T_{sat}} U_{T_{sat}}\right)^2}{h^2}} \tag{39}$$

The partial differential expressions in Eq. (39) are calculated as shown below in Eqns. (40 – 42).

$$\frac{\partial h}{\partial q''} = \frac{1}{T_s - T_{sat}} = \frac{h}{q''} \tag{40}$$

$$\frac{\partial h}{\partial T_s} = -\frac{q''}{(T_s - T_{sat})^2} = -\frac{h}{(T_s - T_{sat})} \tag{41}$$

$$\frac{\partial h}{\partial T_{sat}} = \frac{q''}{(T_s - T_{sat})^2} = \frac{h}{(T_s - T_{sat})} \tag{42}$$

The partial differential terms in Eqns. (40-42) are substituted in Eq. (39) to obtain the following Eq. (43).

$$\frac{U_h}{h} = \sqrt{\frac{\left(\frac{h}{q"}U_{q"}\right)^2 + \left(-\frac{h}{(T_s - T_{sat})}U_{T_s}\right)^2 + \left(\frac{h}{(T_s - T_{sat})}U_{T_{sat}}\right)^2}{h^2}} \tag{43}$$

The Eq. (43) is simplified by opening the parentheses in the numerator and following Eq. (44) is obtained, which is further simplified as shown in Eq. (45).

$$\frac{U_h}{h} = \sqrt{\frac{\frac{h^2 U_{q"}^2}{q"^2} + \frac{h^2 U_{T_s}^2}{(T_s - T_{sat})^2} + \frac{h^2 U_{T_{sat}}^2}{(T_s - T_{sat})^2}}{h^2}} \tag{44}$$

$$\frac{U_h}{h} = \sqrt{\frac{U_{q"}^2}{q"^2} + \frac{U_{T_s}^2}{\Delta T_{sat}^2} + \frac{U_{T_{sat}}^2}{\Delta T_{sat}^2}} \tag{45}$$

Eq. (45) is used to calculate the percentage uncertainty in the HTC. The absolute value of HTC uncertainty is shown as error bars in the experimental results section for various studies as discussed in Chapters 5, 6, and 7.